INVESTIGATIONS OF METAL-SEMICONDUCTOR THIN FILMS AND NANOSTRUCTURES OF LAYERED MATERIALS

A Thesis submitted

in partial fulfillment for the Degree of

Doctor of Philosophy

By

Reshmi S

SC13D011

Department of Physics

INDIAN INSTITUTE OF SPACE SCIENCE AND TECHNOLOGY

THIRUVANANTHAPURAM

MAY 2020

To my beloved Parents, Husband, Sister and Friends…

CERTIFICATE

This is to certify that the thesis entitled **Investigations of metal-semiconductor thin films and nanostructures of layered materials** submitted by **Reshmi S** to the Indian Institute of Space Science and Technology Thiruvananthapuram, in partial fulfilment for the award of the degree of **Doctor of Philosophy** is a *bona fide* record of research work carried out by her under my supervision. The contents of this Thesis, in full or in parts, have not been submitted to any other Institution or University for the award of any degree or diploma.

Dr. Kuntala Bhattacharjee
Supervisor
Associate Professor
Department of Physics

Counter signature of the HOD with seal

डॉ. उमेश आर. कढणे/Dr. Umesh R. Kadhane
सह आचार्य एवं अध्यक्ष/Associate Professor & Head
भौतिकी विभाग/Department of Physics
भारतीय अंतरिक्ष विज्ञान एवं प्रौद्योगिकी संस्थान
Indian Institute of Space Science and Technology
अंतरिक्ष विभाग, भारत सरकार
Department of Space, Government of India
तिरुवनंतपुरम/Thiruvananthapuram-695 547

Thiruvananthapuram
May 2020

DECLARATION

I declare that this thesis entitled **Investigations of metal–semiconductor thin films and nanostructures of layered materials** submitted in partial fulfilment of the degree of **Doctor of Philosophy** is a record of original work carried out by me under the supervision of Dr. Kuntala Bhattacharjee, and has not formed the basis for the award of any other degree or diploma, in this or any other Institution or University. In keeping with the ethical practice of reporting scientific information, due acknowledgments have been made wherever the finding of others have been cited.

Reshmi S

SC13D011

Thiruvananthapuram

May 2020

ACKNOWLEDGEMENTS

The completion of Ph.D thesis would not have been possible without my close association with many people. It is a great opportunity to extend my sincere gratitude to all those people, who made this Ph.D. thesis possible and contributed in different ways.

First and foremost, I would like to extend my sincere and deepest gratitude to my supervisor Dr. Kuntala Bhattacharjee, Associate Professor, Department of Physics, IIST for her excellent guidance, constant encouragement and for giving me complete freedom to grow as a researcher. The extensive discussions during my work, understanding attitude, and personal attention provided the good and smooth basis for my research work. I am thankful for her devoted contribution in reviewing my progress, writing, making corrections to improve and finalize the research papers as well as the thesis. I am highly grateful to her for helping me develop the attitude of independent thinking and build the confidence to pursue independent research.

I gratefully acknowledge Director, Dr. V. K. Dadhwal and former Director, Dr. K.S. Das Gupta, for providing good infrastructure facilities during the tenure of my work. I express my sincere thanks to Dr. Umesh Kadhane, Head of the Department for the academic support. My sincere thanks to former Head of the Department, Dr. S Murugesh, for his continuous support and encouragement. I also gratefully acknowledge the financial assistance from IIST.

I owe my most sincere gratitude to all my doctoral committee members for their critical comments. The suggestions they have given during each evaluation are highly appreciated. I also thank all faculty

members of the Department of Physics for their valuable suggestion which enabled the successful completion of the research work.

I extend my heartfelt thanks to Dr. Sudipta Roy Barman, Scientist-G, UGC-DAE Consortium for Scientific Research, who gave me permission to work in his laboratory for one month and use the facilities available there. Working with his group is a great achievement in my career. I also thank Dr. Abhishek Rai and Dr. Jayita Nayak for giving their valuable suggestions and academic help.

I extend my sincere gratitude to Prof. Saroj Kumar Nayak, Professor, IIT Bhubaneswar to help me work with his group to understand the basics of DFT calculation. A special thanks to Mr. Mihir Ranjan Sahoo for his dedicated academic help.

I am extremely thankful to Dr. Palash Kumar Basu for the collaborative works. I thank him for his fruitful suggestions during my entire work. A special thanks to Ms. Akshaya M V and Ms. Tina C for their whole- hearted help and support.

I extend my sincere thanks to M.Tech student Ms. Janani and project students Gautami Viswan and Sachidanandan.

I would like to give a special thanks to my seniors Dr. Najeeb P K and Dr. Rohith M for their constant encouragement and moral support during my entire Ph.D life. I sincerely admire the contribution of my labmates Mr. Manu Mohan and Ms. Sonia Saini. A special thanks to Manu for helping me whole-heartedly during my thesis correction and submission.

I deeply acknowledge Department of Chemistry-IIST, M G University, Kottayam, and University of Kerala for the characterization studies.

A special mention of thanks to my friends in IIST, Dr. Devi Renuka K, Dr. Meegle S Mathew and Ms. Karthika S. for being my pillar of support during this period. Our friendship will always hold a special place in my heart. Thanks to all my friends who stood by me and encouraged me to reach my goal.

I would like to thank all my teachers who have inspired me throughout these years. A special thanks to all my UG teachers Mr. Remesh Babu, Ms. Geetha, Ms Sarada N S, Dr. K Sabira, Mr. P K Rajashekhar, Dr. Rajan Nambiar, Mr. P A Sivaramakrishnan and late Dr. P.T Thomas for introducing me to world of physics and for always being my mentors.

Words cannot express my love and gratitude towards my family. Thanks to Amma and Acha for being with me, and always supporting my choices. Without their support I wouldn't have succeeded in chasing my dream. I owe them with my life. A special thanks to my sister, who is more like a mother and a friend to me. Thanks for being my constant source of inspiration. I express my deepest gratitude towards Jeeju for his unconditional care and support. Thanks to Kichu and Kunji for being the cute angels in my life.

Thanks to my husband Mr. Rohith Soman for coming into my life and making it so beautiful. His unconditional love and support have always been my strength. Thanks for being my best friend and for supporting my ambitions. I would also thank my mother- in- law, father- in- law for the love and affection they showered on me. Your prayers and support have helped me a lot during my entire Ph.D life.

I would like to thank Malu for being my little sister as well as a good friend. I also extend my sincere gratitude to my other family members for their constant encouragement. Last but not least, I would like to praise the

grace of God whose blessings are marvelous which I am experiencing throughout my life.

(Reshmi S)

ABSTRACT

Semiconductor-metal (MS) heterostructures or heterojunctions are the foundation of modern electronic as well as optoelectronic devices. The most important characteristic when a metal is overgrown on a semiconductor substrate is the formation of the MS junction manifested by the work function difference of the metal and the semiconductor in the form of a potential barrier. This potential barrier is of central importance in determining the performance of various devices. However, engineering the MS contact and to make a sharp MS interface or junction to achieve the required device performance is not an easy job. In most cases, interdiffusion of atoms around the MS junction occurs during the growth process which results in deteriorating device performances. This shortcoming of MS interface can be controlled to some extent by placing an insulating material in between metal and semiconductor electrodes where diffusion and growth kinetics could be taken care of due to the presence of the insulating layer. As a result, metal-insulator-semiconductor (MIS) systems have got a huge attention which could demonstrate better device characteristics depending on the requirements. However, the most used dielectric like SiO_2 on Si substrate has interface states and defects which could be responsible for the diffusion kinetics to take place even on a MIS system. This makes the investigations related to the growth, diffusion kinetics, formation of new interface governed by growth parameters, defects and interstitial processes essential to understand the reliability of the device performance. Thus, a detailed study of growth and interface formation of MIS systems is of great importance.

A strain-induced growth of copper (Cu) and its interaction on a thermally grown, 270 nm thick SiO_2 layer on Si(111) substrates have been investigated. The Cu deposition at 600^0C for 30s followed by post deposition annealing initiates the growth of triangular nanocrystallites on the surface via void filling mechanism even on a 270 nm thick SiO_2 layer. Substrate temperature seems to play a key role in the island formation via diffusion and segregation mostly through void-filling process where 3 fold crystal symmetry of the Cu as well

as of the substrate gets reflected on the morphology of the island growth. Our experimental investigations validate the formation of Cu-oxides, Cu-silicides and an intermediated Cu-O-Si phase in the grown film.

Over the past years, the increased demand for miniaturisation of devices has led to the incorporation of nanostructured materials and two dimensional (2D) layered materials into semiconductor devices. The successful isolation of graphene, a single layer of carbon atoms arranged in a hexagonal motif, from graphite is a breakthrough discovery leading to a different area of research called 2D materials. Transition metal dichalcogenides (TMDs) like MoS_2, WS_2 etc. with a thickness dependent indirect to direct bandgap crossover come under the 2D van der Waals (vdWs) materials which have received enormous attention recently. These materials possess novel electronic, optical, optoelectronic, catalytic properties, many of which could be considered superior to graphene whose technological applications are somewhat limited by its zero band gap nature at the K points.

Nanostructures of TMDs can be easily synthesized and incorporated into semiconductor devices for various applications. We have synthesised MoS_2 nanostructures by a simple liquid phase exfoliation (LPE) of MoS_2 powder in organic solvents followed by microwave treatment (MW) for 10 mins (S1). The probe sonication and the MW treatment play an important role in rolling and curling of the MoS_2 nanosheets to give rise to MoS_2 spheres and rod/tube like-structures with diameter approximately 150–200 nm. The MoS_2 nanorods formed in this fashion are hollow inside with a wall thickness of 15–20 nm and the length of the nanorods is found in the order of several micrometers. The MoS_2 nanostructures, thus, obtained are mainly comprised of 2H semiconducting phase and exhibit good emission.

By simply changing the MW treatment time to 30 mins (S2), we observe that the nanostructures of rods/tubes, spheres and the sheets formed in the sample consists of a mixture of metallic 1T and semiconducting 2H phases with more of 1T than of 2H with a ratio of 70 (1T): 30 (2H). This nanostructured sample S2 also exhibits high emission yield, however, less compared to the 10 min MW

irradiated sample, S1 due to the presence of more metallic 1T phase. The estimated width/diameter of the nanostructures in this case is in the range of 50-150 nm. High resolution transmission electron microscope (HRTEM) investigations performed on S2, clearly demonstrate the formation of sharp coplanar heterojunction of hybridized 1T-2H superlattice phase. This kind of coplanar heterojunctions composed of same layered material with different structural polymorphs have drawn immense interest recently due to low contact resistance and high carrier injection rate owing to low Schottky barrier height. Present research has largely focused on efficient exfoliation of these layered materials and their restacking to achieve better performances. HRTEM investigations reveal evidence of surface ripplocations within the same exfoliated layer of MoS_2. The structural stability of 1T-2H superlattice phase during HRTEM measurements under an electron beam of energy 300 keV is studied. We find that while the nanostructures comprised mainly of 2H semiconducting phase (S1) are very vulnerable towards 200 - 300 keV electron beam, the exfoliated sheets constituted of 1T-2H hybridized phase exhibit no sign of electron beam interaction. This structural stability could be either associated to the change in electronic configuration due to induction of the restacked hybridized phase with 1T- and 2H- regions or to the formation of the surface ripplocations. Surface ripplocations can act as an additional source of scattering centers to the electron beam and also it is possible that a pulse train of propagating ripplocations can sweep out the defects via interaction from specific areas of MoS_2 sheets.

In this thesis, we first study the growth kinetics and interface formation for a conventional MIS system of Cu-SiO_2/Si. Even on a thick SiO_2 dielectric layer of 270 nm, we observe atomic diffusion forming different phases of Cu-oxides, Cu-silicides and an intermediate phase of Cu-O-Si in the sample. Evidence of triangular voids on the surface and the formation of triangular nanocrystallites clearly demonstrate that the formation of islands has taken place via void filling mechanism even on a thick SiO_2 layer. Then we have focussed our studies on to a more recent semiconducting layered material of MoS_2 and tried to develop a simple top-down strategy to exfoliate MoS_2 nanostructures which could have potential technological applications. We have taken a MW assisted easy, fast and

efficient route to induce high concentration of metallic 1T phase in the original 2H matrix of exfoliated MoS_2 layers. This mixed phase demonstrates high structural stability under 200 – 300 keV electron beam and shows a sharp MS junction. This structure could be considered superior to the conventional MS interface due to the lack of lattice mismatch and subsequent reduction of strain in the structure.

TABLE OF CONTENTS

CERTIFICATE v

DECLARATION vii

ACKNOWLEDGEMENTS ix

ABSTRACT xiii

TABLE OF CONTENTS xvii

LIST OF TABLES xxi

LIST OF FIGURES xxiii

ABBREVIATIONS xxv

1. CHAPTER 1: INTRODUCTION 1

2. CHAPTER 2: METAL – INSULATOR-SEMICONDUCTOR (MIS) SYSTEM: Cu-SiO_2/Si

2.1. Introduction 12

2.1.1. General overview: metal-semiconductor (MS) Systems 12

2.1.2. Cu-SiO_2/Si system: Importance and brief Overview 14

2.2. Experimental section 17

2.2.1. Materials 17

2.2.2. Sample preparation 18

2.2.3. Instrumentation 18

2.3. Results and discussions 20

2.4. Conclusion 36

3. CHAPTER 3: SYNTHESIS OF MoS_2 NANOSTRUCTURES AND INTERACTION WITH ELECTRON BEAM: GENERAL OVERVIEW

3.1. Introduction 40

3.2. Structure of TMDs 43

3.3. Electronic band structure 46

3.4. Liquid phase exfoliation 48

3.4.1. Criteria for the selection of solvent 48

3.4.2. Multi solvent system- cosolvency technique 50

3.4.3. Purification of the sample 51

3.5. Liquid phase exfoliation of TMDs 51

3.6. Synthesis of nanostructures of TMDs using LPE 54

3.6.1. Influence of MW heating 56

3.7. Mechanism of electron beam interaction 58

3.7.1. Radiolysis 59

3.7.2. Heating 60

3.7.3. Knock-on 61

3.8. Effects of electron irradiation 61

3.8.1. Atomic defects 62

3.8.2. Structural phase transformations 64

3.8.3. Formation of nanostructures 65

3.9. Conclusion 67

4. CHAPTER 4: CHARACTERIZATION OF MoS_2 NANOSTRUCTURES- MORPHOLOGY, OPTICAL AND VIBRATIONAL PROPERTIES

4.1. Introduction 70

4.2. Experimental section

4.2.1. Materials 72
4.2.2. Sample preparation 72
4.2.3. Instrumentation 73
4.3. Results and discussions 73
4.3.1. Morphology studies 73
4.3.2. Optical characterizations 78
4.3.3. Vibrational characterizations 85
4.4. Conclusion 88

5. CHAPTER 5: STRUCTURAL STABILITY OF MoS_2 NANOSTRUCTURES
5.1. Introduction 92
5.2. 2H to 1T phase transformation in MoS_2: Brief Overview 93
5.3. Stability of 1T- 2H hybrid phase: Energetics 95
5.4. Experimental section 96
5.5. Results and discussions 97
5.6. Conclusion 107

6. CHAPTER 6: CONCLUSIONS AND FUTURE PERSPERCTIVES
6.1. Conclusions 109
6.2. Future perspectives 111

BIBLIOGRAPHY 113

LIST OF PUBLICATIONS 151

CONFERENCES AND SEMINARS 152

LIST OF TABLES

TABLE	TITLE	PAGE NUMBER
2.1	Percentage concentration of various chemical phases present in the sample	28

LIST OF FIGURES

2.1.	Schematic representation of the deposition process	18
2.2.	AFM image of Cu deposited film on SiO_2/Si(111) surface	20
2.3.	SEM micrographs of the nanoislands formed on the SiO_2/ Si(111)surface	22
2.4.	Schematic depecting the growth process of Cu on SiO_2/Si substrate	24
2.5.	High resolution XPS spectra on the grown film	25
2.6.	Raman spectrum acquired from SiO_2/Si before and after Cu deposition	31
2.7.	Schematic representation of the electrical measurements	33
2.8.	Two electrode electrical measurements performed on the grown film	34
3.1.	Schematic depicting the arrangement of atoms in monolayer MoS_2	44
3.2.	Schematic showing the different polymorphic forms of TMDs	45
3.3.	Schematic showing the various types of electron beam interaction with the sample.	59
3.4.	Schematic representation of electron beam heating process	60
3.5.	Schematic representation of knock-on process	61
4.1.	SEM images of MoS_2 dispersion before MW treatment	74
4.2.	SEM investigations on 10 min MW treated sample (S1)	74

4.3.	TEM investigations on 10 min MW treated sample (S1)	75
4.4.	SEM micrographs from the 30 min MW treated MoS_2 sample (S2)	76
4.5.	Schematic of the exfoliation process of bulk MoS_2 and the effect of MW treatment.	77
4.6.	UV–Vis absorption spectrum of MW treated sample (S1)	78
4.7.	The featureless UV-Vis absorption spectrum obtained for S2	81
4.8.	UV-Vis absorption spectrum for non-MW treated sample	82
4.9.	Photoluminescence spectrum obtained for different excitations from the exfoliated sample	83
4.10.	Raman spectrum for bulk MoS_2 powder as well as non MW treated sample	85
4.11.	Raman measurements carried out on exfoliated MW treated samples	87
5.1.	TEM images showing the beam interaction of S1	97
5.2.	TEM images of S2	99
5.3.	TEM images showing the presence of ripples	102
5.4.	Electron diffraction pattern obtained from S2	103

ABBREVIATIONS

AFM	Atomic Force Microscopy
CVD	Chemical Vapor Deposition
EBIF	Electron Beam Induced Fragmentation
EDP	Electron Diffraction Pattern
FWHM	Full Width at Half Maximum
HSP	Hansen Solubility Parameter
HRTEM	High Resolution Transmission Electron Microscope
IC	Integrated Circuit
LPE	Liquid Phase Exfoliation
LP	Lone Pair
MS	Metal- Semiconductor
MIS	Metal- Insulator- Semiconductor
MW	Microwave
NMP	N Methyl Pyrollidine
PL	Photoluminescence
PLD	Pulsed Laser Deposition
RT	Room Temperature
RBS	Rutherford Backscattering
SAED	Selected Area Electron Diffraction
SEM	Scanning Electron Microscopy
STEM	Scanning Transmission Electron Microscopy
TMD	Transition Metal Dichalcogenide
TEM	Transmission Electron Microscopy
UHV	Ultra-High Vacuum
vdWs	Van der Waal's

XPS	X-ray Photoelectron Spectroscopy

CHAPTER 1

INTRODUCTION

This chapter deals with an overall view about the work that has been discussed throughout the thesis. A general discussion about synthesis of nanostructures, importance of nano dimension and the metal-semiconductor (MS) systems in technological applications, and the dominance of 2D materials with superior properties in these fields etc. had been highlighted here.

Demands of miniaturization has called for increasing efforts to synthesize, understand and apply materials with reduced dimensions in nanometer/atomic scale which exhibit enhanced properties than their bulk counterparts. This has resulted in tailoring structures in nano and atomic scales serving enormous demands and challenges related to electronics, optoelectronics, engineering, energy saving, medical and biotechnology. As a result, the field of nanoscience and nanotechnology has become a topic of intense interdisciplinary research across the globe where scientists from different disciplines are working together to meet the challenges imposed by Moore's law. The reduction in the physical size of the materials and the corresponding changes occurring in the properties can mainly be understood as the motion of the charge carriers which is constrained in a particular direction(s) due to reduced size. This constraint in the motion of the charge carriers will give rise to quantum confinement effects giving rise to superior and exotic electrical, electronic, optical, thermal and mechanical properties.

Apprehending the requirements and versatile applications associated with these low dimensional structures, last few decades have experienced an urge to divulge in the hardship and challenges towards practical realization by taking various routes of growth and synthesis. Increasing emphasis on the control of size, shape, structure, morphology, connectivity of molecules, supermolecules, nano-objects and nanostructured materials and devices have made synthesis and assembly at the atomic and nanometer scales which have opened up two main fabrication platforms categorized as `top-down' and `bottom-up' approaches. Microelectronic systems which are typically based on integrated device platforms need each component to be addressed individually where the mode of fabrication becomes really important to address this requirement significantly. In this context, `top-down' fabrication seemed to be the most adequate and efficient to meet with the demands and requirements of the shrinking device technology (Hobbs, Petkov, & Holmes, 2012). However, recent developments and advances related to the 'bottom-up' fabrication have demonstrated

its tremendous credentials where it has been even possible to build single atom structures precisely on a desired substrate showing the ultimate path towards device fabrication with array of atom chips. Routine fabrication of sophisticated low dimensional structures with utmost precision has become feasible by `bottom-up' approach today. Chemical and biological routes of synthesis and assembly guided by "top-down" or "bottom-up" approach proved to be highly efficient to create fully functional nanostructures that are operational at mesoscopic scale. Preparation of complex organic building blocks of polymeric materials, dendrimers etc., preparation of nanocrystals of metals and semiconductors with narrow size distribution utilizing the concept of ligand exchange and surface derivatization, controlled synthesis of nanotubes and rod structures and nanoparticles have been possible which are characterized by topology, morphology, size, bond energy and so on. As a result, depending on the requirements and circumstances it might be highly advantageous to have a synergy between both 'top-down' and 'bottom-up' paradigms (Hobbs et al., 2012) via integrating one of the assembly concepts with the other. This will result in creating new nanometer scale building blocks with unprecedented properties.

Single crystal silicon (Si) has been considered as an integrated component of microelectronics since the initial era, due to its high abundance in earth's crust as well as the stability and high quality of oxide (SiO_2) on Si. Growth of metal on SiO_2/Si systems has received enormous attention from the technological point of views. Formation of metal nanostructures on an insulating layer on a semiconductor substrate of Si and the associated enhanced optical, electronic properties with modified band gap and carrier transport showed the enormous potential this field owns to make it as one of the foremost area of research (Zilberberg & Riedl, 2016), (KO et al., 2016). In the last few decades, main aim of basic and industrial research was to understand the growth of metals on bare or insulated semiconductor surfaces, post-growth surface morphology and the interfaces. Growth of metals on semiconductor surfaces via `bottom-up' approach would vastly be dependent on the combination of materials chosen, surface energies of the materials and the

temperature (Winfried Monch, 1990). Thermal evaporation method is one of the most commonly used techniques to grow metals on semiconductor substrates, where the growth kinetics would strongly rely on the choice of the materials and on the substrate temperature during deposition leading to interesting surface and interface phenomena. While the surface morphology of the metal overgrown Si evolves via shape and orientation controlled growth of nano islands and nanowires governed by the surface energies, interface potential, crystal symmetry of the substrate etc.; formation of the interface, its physical conditions and chemical compositions would mainly depend on temperature dependent diffusion kinetics. As a result, metal-Si systems are not mostly isostructural at the interface. Developments in the `bottom-up' fabrication process has come up with the option of sophisticated growth of epitaxial heterostructure films under ultra high vacuum (UHV) conditions with high crystalline quality and sharp interface, however, vastly limited by isostructural materials with similar/nearly-similar lattice parameters, making the conventional thermal evaporation as still the primary choice. As a result, a vital understanding of the solid phase interaction occurring at the surfaces and interfaces is required in order to obtain an overall view of the reliability and stability of the electronic devices (Grimaldi, Wieluński, Nicolet, & Tu, 1981). The conventional electronic devices, built upon Si, encounters metallic contacts like Copper (Cu), Silver (Ag) etc., out of which Cu-Si interface has garnered top interest due to the low resistivity, low cost and low diffusivity into Si. Diffusion of metals into Si wafers limits the device performance owing to increased leakage current (Istratov, Flink, Hieslmair, Weber, & Heiser, 1998). The studies have also been carried out to understand the diffusivity of metals into Si substrates covered with dielectric oxide layer. Thus, investigations of the surfaces and the interfaces at metal-Si, metal-dielectric-Si boundary is extremely important to improve our fundamental knowledge about growth and diffusion kinetics (Grimaldi et al., 1981), (Yüksel, 2009), (Werner & Güttler, 1991).

The interface between metal-semiconductor (MS) is characterized by the potential barrier between the Fermi level in the metal and the band edge of

semiconductor at that interface (Winfried Monch, 1990). The barrier height is decided mostly by the interface atomic arrangements and atomic (Werner & Güttler, 1991), (Chand & Kumar, 1997), (Cetin & Ayyildiz, 2005), (Tung, 1992) diffusion. This potential barrier is of central importance in determining the performance of semiconductor devices. When metals are grown on semiconducting surfaces, diffusion of metal into the semiconductor lattice occurs (McBrayer, 1986). This intermixing process has been studied extensively since 1960's. With the miniaturisation of semiconductor devices, the knowledge and control of such interface interactions has become more important than ever. In most of the cases, the oxide layer found on semiconductors act as a diffusion barrier thereby controlling the intermixing of metal and semiconductor. However, the shrinking size and formation technique often makes it difficult to have complete control on the diffusion process.

Owing to high demand in miniaturisation of devices, it became difficult to improve the performance of the Si based devices with shrinking size. Thus, new materials and device structures to relax the physical limitation in device scaling are now required. With the discovery of graphene (Geim & Novoselov, 2007), the study of two dimensional materials became a hot topic among materials science community. However, graphene owing to its semi-metallic behaviour, has limiting use in device applications. Transition metal dichalcogenides (TMDs) help in overcoming the intrinsic shortcoming of graphene which show tunable bandgap depending on their thickness. . TMDs like MoS_2, WS_2 etc. with an intrinsic bandgap mostly in the visible and near-infrared limit possess novel electronic (Das, Chen, Penumatcha, & Appenzeller, 2013), optical (Scheuschner et al., 2014), optoelectronic (Mueller & Malic, 2018) and catalytic properties (A. K. Singh et al., 2018). Reduced dimensionality also paves way for the demonstration of unique properties. The van der Waal's (vdWs) attraction present between the layers makes the exfoliation of these materials into mono/few layers, an easy job (A. K. Singh et al., 2018). An interesting property regarding these materials also, lies in their ability to exist as

structural polytypes (Manzeli, Ovchinnikov, Pasquier, Yazyev, & Kis, n.d.), mainly metallic 1T and semiconducting 2H phases which differ in their electrical properties.

MoS_2, because of its high mobility, has been incorporated in various electronic devices (Rai et al., 2018). A single layer of MoS_2 consists of 6.7Å thick slab of S-Mo-S sandwich with a direct bandgap of ~1.9 eV in monolayer and indirect bandgap of ~1.2 eV in bulk form (Kan et al., 2014). Electron mobilities in monolayer MoS_2, as predicted from theoretical calculations ranges from 130 - 480 cm^2/Vs. (Rai et al., 2018), (X. Li et al., 2013), (Jin, Li, Mullen, & Kim, 2014). Moreover, high saturation velocities of both electrons and holes (3.4 - 4.8 × 10^6 and 3.8 × 10^6 cm/s respectively) also makes them an ideal candidate for semiconductor device applications (Jin et al., 2014). Thus MoS_2 could be a promising candidate to successfully outperform (Kappera et al., 2014), (Radisavljevic, Radenovic, Brivio, Giacometti, & Kis, 2011) the conventional 3D semiconductor devices, with seemingly less channel length (< 5nm) (H. Liu, Neal, & Ye, 2012) with their huge carrier mobility values even in sub nm thickness.

In addition to the nanosheets, various nanostructures of MoS_2 can also be incorporated into device structures (Dominko et al., 2002), (Acerce, Voiry, & Chhowalla, 2015). The synthesis of nanostructures is usually associated with tedious chemical reactions (Vattikuti, Byon, Reddy, Shim, & Venkatesh, 2015), (G. Liu et al., 2016a). There exist various techniques to exfoliate or synthesize thin 2D sheets of layered materials. Out of these methods, solution based exfoliation has been demonstrated to be versatile route to the bulk production of 2D sheets and could be a viable method for implementation of these materials into technological front (Dodoo-Arhin et al., 2016). Implementation of heterostructures in low dimensional structures like quantum dots, nanowires, nanosheets etc. is a vital step towards their integration into nanoscale devices. The lattice mismatch between the metal and MoS_2 also plays a significant role in altering the Schottky barrier height and thereby the electrical properties of these nanostructures (Ci et al., 2010). However, one of the most important technological aspects of working on

TMDs like MoS_2 is its polymorphism. It is indeed possible to form a coexisting electrically dissimilar polymorphs (1T and 2H) that are lattice matched such that they form chemically homogeneous atomic and electronic structures (Eda, Fujita, et al., 2012), (Z. Lin et al., 2016). Theoretical calculations carried by Gao *et al.*. in 2015 concluded that the interface effects can be restricted to a region of 1 nm and the material shows pure semiconducting/metallic behaviour toward the central region of 2H /1T domains in MoS_2. The electronic devices built with the 1T phase as electrode on the 2H semiconducting phases provide supreme performance because of the absence of lattice mismatch, which otherwise is a problem in the case of conventional MS structures. Such a homo junction consisting of different phases of the same material with least or no lattice mismatch can considerably increase the carrier mobility and subsequently improved device performance when in comparison with the conventional metal electrodes (Kappera et al., 2014).

The work carried out in this thesis lies within the broad interest of metal-semiconductor systems. First, we try to develop our understanding on a conventional metal-dielectric-semiconductor system of Cu-SiO_2/Si. We focussed our studies related to growth and interface formation when Cu was deposited on a relatively thick dielectric (270 nm) of SiO_2 on Si(111) substrate at an elevated temperature. Though metal growth on semiconductor surfaces had been studied extensively before, however, a proper understanding of growth of Cu and its diffusion processes on a thicker dielectric layer on a Si substrate was missing. Our investigations reveal that even on a 270 nm thick dielectric of SiO_2, Cu grows via void filling mechanism following the substrate crystal symmetry with clear evidence of formation of triangular voids and growth of triangular nanocrystals. X-ray photoelectron spectroscopy (XPS) measurements carried out on the post-grown samples reveal the chemical and elemental compositions of the film and the interface which is mainly composed of Cu-O-Si intermediate phase along with the evidence of formation of Cu-oxides and Cu-silicides. We try to develop an understanding of the preliminary electrical behaviour of the grown film by performing investigations using a two probe

measurement system, which reveal that the film is not metallic in nature. Then, we shift our focus from Cu-SiO_2/Si system to the most recently happening material, MoS_2 which belongs to the class of layered TMDs, driven by the fact that this material shows room temperature (RT) polymorphisms of metallic, 1T and semiconducting, 2H phases. By taking a trivial route of liquid phase exfoliation (LPE) followed by microwave (MW) treatment, we successfully synthesize nanostructures of rods, tubes, spheres and sheets of MoS_2 with a narrow size distribution where the width/diameter of the MoS_2 rods, tubes and spheres lies in the range of 50-200 nm depending on MW irradiation time. We also show that the MW treatment introduces 1T phase in the original 2H matrix of MoS_2 and thus, it is possible to make nanostructures with semiconducting, or semiconducting-metallic mixed phase by tuning the MW irradiation time. These nanostructures exhibit pronounced emission and reveal atomically sharp metal-semiconductor 1T-2H heterojunction. The formation of metallic 1T within the 2H phase of MoS_2 is driven by time dependent MW irradiation. For a 10 min MW treated sample, we find that the nanostructures are mostly composed of semiconducting 2H MoS_2, whereas, for 30 min MW irradiation, the sample is dominated by metallic 1T phase. This hybridized superstructures of 1T-2H MoS_2 show tremendous structural stability towards electron beam of energy 300 keV.

The structure of this thesis is as follows. Chapter 2 describes the general formation of conventional MS junction with an insight of the interface phenomena occurring while a metal is deposited on a semiconducting material followed by a general overview on Cu-SiO_2/Si system. Then we provide details about our experimental work involving the growth of Cu onto SiO_2/Si surface. Chapter 3 deals with the general introduction to 2D vdWs materials - structural polytypes and the band structure followed by an overview of LPE technique and the influence of MW in the formation of nanostructures of TMDs. These vdW 2D materials, being highly influenced by atmospheric radiations, are prone to structural transformations. Such transformations which generally occur during the experimental procedures and

characterisations usually under electron beam will also be discussed briefly. Our experimental investigations related to the morphology, optical and vibrational properties of the MW assisted LPE synthesized nanostructures of MoS_2 will be addressed in Chapter 4. Our observations related to the structural phase change from 2H to 1T, induced by the influence of MW and the associated structural stability of the as synthesised hybrid superlattice phase of 1T-2H MoS_2 will be discussed in chapter 5. This will be followed a chapter dedicated to the conclusions and future outlooks.

CHAPTER 2

METAL-INSULATOR-SEMICONDUCTOR (MIS) SYSTEM: Cu-SiO_2/Si

This chapter deals with a general overview of the conventional metal-semiconductor junction followed by our results and discussions related to Cu-SiO_2/Si system.

2.1. Introduction

2.1.1. General Overview: Metal-Semiconductor (MS) systems

Study of metal semiconductor interactions and formation of interface has received huge attention owing to its application in electronics and semiconductor industry (Schlesinger, 1990), (S. Li et al., 2010), (Park, Han, Kang, Shin, & Park, 2014). The classical picture of metal- semiconductor (MS) interface depicts an abruptly ending junction between a metal and a semiconductor. According to this scenario, the electronic properties of the interface depends only on the bulk properties of the two materials. However, experimental evidences show the formation of regions with different chemical bonding and/or interface diffusion occurring at the clean MS junction. Microscopically, these phenomena results in the rearrangement of atomic charges at the interfaces. The rectifying behavior of the MS junctions were observed in the early 1870's, however, without any proper explanation till 1938 when Schottky explained this observation to be arising due to the depletion of mobile carriers on the semiconductor side of the junction. Such space charge depleted layers in the junction are known as Schottky barriers. The electrical transport properties of the junction thus, depends on the barrier height which is obtained as the energy difference between Fermi level of the metal and valance band top (conduction band minimum) for p type (n type) semiconductors. Depending on the the Fermi level mismatch owing to the work function difference between the two materials, there can be two main possibilities to define the interface region as Schottky contact and Ohmic contact for an ideal MS interface. However, deposition of metal atoms on the semiconductor substrate surface is assisted by numerous surface and interface processes starting from growth of nanocrystallites to interface reaction and inter diffusion of atoms (Vermaak, Snyman, & Auret, 1977), (W. Monch, 1990). These processes at the interface are mainly driven by substrate temperature, bond breaking and structural defects on the substrate surface which can give rise to stable or meta stable new compounds at the interface. Various possibilities for the diffusion

mechanism at the interface can be categorized as lateral diffusion of atoms on the surface, diffusion of surface atoms into the substrate and diffusion of substrate atoms into the surface component. The movement of atoms in a crystal lattice is defined by diffusivity or diffusion coefficient, D. This is usually initiated by a thermally activated jump of atoms overcoming the potential barrier. In this case, the diffusion coefficient can be expressed as an Arrhenius relation,

$$D = D_0 e^{-Q/kT}$$

Where, Q is the activation energy. D_0 and Q are the parameters determined by the diffusion mechanism of the particular atom or defect.

Diffusion process is hugely influenced by the electronic configuration of the diffusing atom, its size, temperature, formations of chemical bonds and interaction with the defect structures. The kinetics of a new compound formation are driven by the involved atom species, related mass transport, interface reaction steps and reaction rates entailing the motion of atoms across or through the MS interface. In case of Si substrate, the native defect density is usually low which cannot support properly the high diffusion observed by Au, Ag, Al etc.. As a result, it had been proposed that the diffusion is mainly dominated by an interstitial diffusion mechanism [56], [59], [60] with an activation energy of around 0.5-1.0 eV. Even for the Si substrate with thin layer of SiO_2 have shown diffusion of metal atoms when deposited at an elevated temperature.

Interaction processes on the surfaces and interfaces also manifest the formation of various nanostructures depending on surface free energy, crystal symmetry, lattice parameter, temperature, deposition rate, diffusivity, substrate defects and so on. Diffusion of metals through the oxide layer on the Si surface which comes under general purview of an Metal- Insulator- Semiconductor (MIS) system, is found to be facilitated by the presence of preexisting defects in the oxide layer. Even high quality thermally grown oxide on the Si surfaces can have holes/voids. These voids can reduce the actual path to be travelled by the diffused metal atoms through

the oxide and thus reach the interface faster. The formation of voids is further enhanced by stress in the oxide layer due to the deposited film. The growth of islands in the film which usually follow the substrate crystal symmetry can directly be aided through these voids (H Dallaporta, M Liehr, 1990).

Lattice mismatch involved during the growth of metals on semiconducting substrates introduces strain in the grown overlayer. The mechanism of relaxation from the strained state involves formation of various dislocations, growth of islands, shape transformations of the nanostructures to optimize the strain and energy of the system. It has been observed that for the growth of Au on Si(111) substrate a perfect symmetry is maintained by the grown islands below a critical size, beyond which, it gets elongated and forms the best suitable shape in order to minimize the strain in the system (Sekar et al., 1995).

2.1.2. Cu-SiO_2/Si system: importance and brief overview

Copper (Cu) with its low cost, low electrical resistivity (~1.7 μΩ-cm) and higher melting point (1357.6 K) showed tremendous potential for applications in the electronic devices as Schottky junctions, metal gates and local interconnects (S. Li et al., 2010). Cu is having a lower resistivity and a lower diffusivity compared to aluminium. As a result, significant research interest is seen in the areas of growth of Cu thin films, and improvement of the film quality via tailoring deposition techniques. However, even with a lower diffusivity, Cu interacts with Si or SiO_2/Si substrate which is considered to be a limiting factor to maintain the device performances mainly due to the problem of leakage current. Many studies are being carried out in order to understand the interaction and diffusion of Cu in SiO_2/Si matrix (Noelia Benito & Flores, 2017), (Bo, Yan-hui, Gong-Ping, & Xi-Meng, 2010) and even on a native oxide layer (J. Zhang, Liu, & Fan, 2013), (Savchenkov, Shukrinov, Mutombo, Slezák, & Cháb, 2002), (J.R. Shi , S.P. Lau, Z. Sun, X. Shi,

B.K. Tay, 2001), (Benouattas & Mosser, 2000), (Benouattas, Mosser, & Bouabellou, 2006). However, work related to growth of Cu on a relatively thick dielectric of SiO_2 on Si substrate is not yet reported.

Effect of annealing on Cu-Si system had been studied by different groups (Benouattas & Mosser, 2000), (Sekar, Satyam, Kuri, Mahapatra, & Dev, 1993), (Ektessabi, 1993), (Dolbak, Zhachuk, & Olshanetsky, 2003). Thin films deposited at room temperature (RT) by the ``bottom-up'' approach of thermal evaporation usually do not show good chemical bond with the substrate due to lower kinetic energy of the incoming atoms and non-uniformity in sticking coefficient (J. B. Zhou & Gustafsson, 1997). Substrate heating and post-deposition annealing are important processes in order to achieve high-quality films from the vapor deposition technique, which mostly leads to the formation of silicides and oxides in the Cu-SiO_2/Si system. The coefficient of Cu segregation in to Si(111) surface is highest for a temperature range of 500-650^{0}C (Dolbak et al., 2003). However, this was reported for clean Si(111) surfaces without any oxide layer. Annealing at high temperature will lead to the coalescence of copper and to the formation of isolated crystallites (Zhou Zhang et al., 2008) which are mostly reported to be comprised of copper silicide for native oxide of 2-4 nm or for bare Si substrates. As a result, these nanostructures usually follow the crystal symmetry of the substrate surface.

Diffusion and interaction of Cu in the SiO_2/Si system will mainly result in the formation of Cu silicides and Cu oxides depending on growth parameters and thickness of the SiO_2 layer. By performing Rutherford backscattering (RBS) experiments on Cu/Si system, Sekar *et al.*.had shown that for Si(111) surfaces with a native oxide layer, the onset temperature of inter diffusion of Cu is in the range of 500-700 ^{o}C (Sekar et al., 1993). Cu silicides can form at a relatively lower temperature than other metal silicides (Aboelfotoh, Krusinelbaum, & Aboelfotoh, 1991). There are three stable Cu-Si alloys which exist at RT and are metallic, out of them Cu_3Si is the most stable (S. Li et al., 2010). Cu silicides have got significant

applications as a catalyst for hydrogenation, chlorosilanes formation and gas etching of silicon. Strong resistance to oxidation is displayed by these metal silicides compared to their metal counterparts which makes them highly applicable as electronic interconnects. Owing to its high charging and optimized cycling properties, the metallic Cu_3Si poses itself as a suitable candidate as an anode in a Lithium-ion battery (In-Chul Kim, Dongjin Byun, Sangwha Lee, 2006). On the other hand, two main variants of Cu oxides which are usually formed due to reaction with oxygen from the SiO_2 interface are Cu_2O and CuO. Both these two oxides are p-type semiconductors. Cu oxide thin films have received enormous attention in the last decades where it has been shown that Cu_2O is a good candidate for applications in the area of spintronics (Pearton, Heo, Ivill, Norton, & Steiner, 2004), catalysis (Ramírez-Ortiz et al., 2001), and solar cells (K. Han & Tao, 2009), (Fernando & Wetthasinghe, 2000), whereas CuO is an attractive system related to photo thermal and photoconductive applications (Koffyberg & Benko, 1982).

Our main aim to carry out this work was to understand the growth and interaction of Cu on a thick SiO_2 barrier on Si substrate. Previous reports related to growth of Cu were mainly focused to study elemental compositions and chemical nature (Noelia Benito & Flores, 2017), (Bo et al., 2010), (Wright & Mooradian, 1967), (Morales, Barranco, Caballero, Holgado, & Gonza, 2002), (Sarkar et al., 1998), electron and electrical transport properties (Wright & Mooradian, 1967), (Aboelfotoh et al., 1991), (Yuan et al., 2013) when Cu was mainly grown on native oxide layer or on bare Si substrate (S. Li et al., 2010), (Zhou Zhang et al., 2008). Growth of metal films on passivated Si (Sekar et al., 1993), (A. Roy, Sundaravel, Batabyal, & Dev, 2012), (Sundaravel, Das, Ghose, Sekar, & Dev, 1999), (Sundaravel, Das, Ghose, Rout, & Dev, 1999), (Sundaravel, Sekar, et al., 1999), (Sekar et al., 1995), (Sumitomo, Kobayashi, Shoji, Oura, & Katayama, 1991), (Nishiyama et al., 1996) had also been investigated earlier. Zhang et.al (Zhou Zhang et al., 2008) reported shape- and orientation- controlled growth of nanotriangles, nanosquares and nanowires of Cu_3Si on Si(111), Si(100) and Si(110) surfaces respectively with a

native SiO_2 layer of 2-4 nm thickness through Au nanoparticle assisted vapor transport method and reviewed the dependence of substrate crystal symmetry on the growth morphology of Cu_3Si. However, as our limited search goes, growth of Cu and its interaction on a relatively thick dielectric of SiO_2 on Si substrate has not yet been explored which is important to understand the role of Cu as a candidate material for any device application.

In this work, the strain-induced growth of copper (Cu) and its interaction on a thermally grown, 270 nm thick SiO_2 layer on Si(111) substrates have been investigated. Surface morphology of the Cu deposited (at 600^{o}C) annealed film, its chemical compositions and preliminary electrical characteristics are studied by atomic force microscopy (AFM), scanning electron microscopy (SEM), X-ray photoelectron spectroscopy (XPS), Raman spectroscopy and by two probe transport measurement system. We observe growth of triangular voids and nanocrystallites on the surface via void filling mechanism even on a 270 nm thick SiO_2 layer. XPS investigations reveal formation of a Cu-O-Si (> 41 %) mixed intermediate phase in the film along with Cu oxides and Cu silicides. Two probe electrical measurements performed on the grown film from RT to 200^{o}C reveal that the film is not metallic and display room temperature resistance of the film which is of the order of 1500 - 2000 Ω. This is attributed to the collective behavior of different phases coexisting in the film with a significant amount consisting of Cu-O-Si intermediate phase.

2.2. Experimental Section

2.2.1. Materials

Si(111) substrates with a SiO_2 layer of 270 nm thickness were purchased from Testbourne Ltd, UK.

2.2.2. Sample preparation

SiO_2/Si(111) wafers were first cleaned in organic solvents before loading into the deposition chamber. In the thermal deposition chamber, the substrate temperature was set at 600^0C and was maintained at that temperature by a temperature controller for 60 minutes prior to deposition to ensure uniform temperature attainability of the substrate surface. The temperature of the substrate heater was measured by a thermocouple and the set temperature of 600^0C of the substrate heater was maintained within an accuracy of $\pm 10^0$C. Copper was deposited from a thermal evaporator for 30 seconds at a rate of 2 Å/s on SiO_2/Si(111) surface which was kept at 600^0C. The pressure inside the chamber during deposition was 5.7×10^{-6}mbar. After deposition, the substrate heater was maintained at the same temperature and the samples were annealed for 60 minutes. Post-deposition annealing was followed by normal cooling down to RT before taking the samples out from the deposition chamber.

2.2.3. Instrumentation

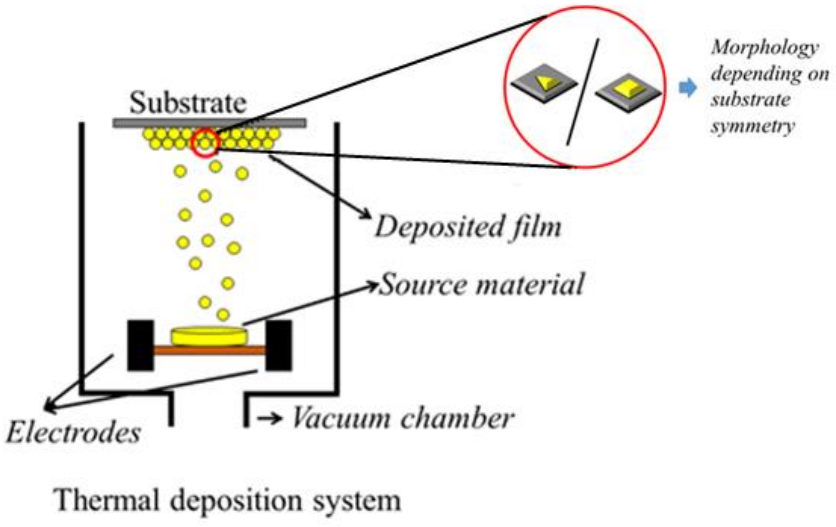

Figure 2.1;Schematic representation of the deposition process

The turbo molecular pump based thermal evaporation set up was procured from H. Fillunger and Co. Pvt. Ltd. Pune, India. The surface morphology of the samples was investigated using atomic force microscopy (AFM) [Agilent: 5500 AFM/SPM N9410S and Nanosurf: NaioAFM] and scanning electron microscopy (SEM) (Carl Zeiss EVO 18 Secondary Electron Microscope). Data acquired by AFM were investigated and analyzed using WSxM[34] software package and SEM images were analyzed using ImageJ. The elemental composition and chemical stoichiometry of the samples were studied by X-ray photoelectron spectroscopy (XPS). All XPS spectra were acquired at room temperature using an Omicron Multiprobe system and monochromatic Al–Kα ($h\nu$ = 1486.7 eV) x-ray radiation source (Anupam Roy et al., 2013). The background pressure during measurements was kept below 3×10-10 mbar. The chemical composition of the grown film was quantified using the Casa XPS software. Raman spectroscopy measurements have been carried out in a Renishaw inVia Raman Microscope using a laser excitation of 532 nm. The electrical characterizations have been carried out using a two-probe probe station connected to a power supply procured from Agilent Technologies (B2912A precision source/measure unit.

2.3. Results and Discussions

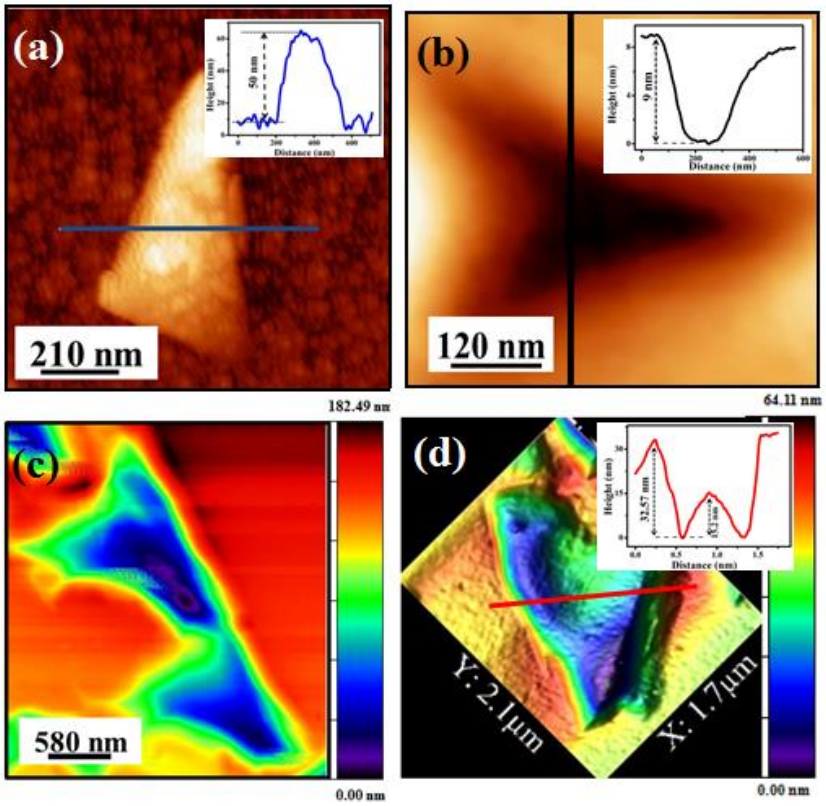

Figure.2.2.(a) AFM image of Cu deposited film on SiO_2/Si(111) surface. Formation of triangular island is clearly seen. A line profile taken across the island is shown as an inset in (a), (b) formation of empty triangular voids in the sample. Line profile taken across the void is shown as an inset. (c) and (d) show array of triangular voids and presence of partially filled void respectively. Corresponding z-scale of the images is shown in the right side.

Figure.2.2 shows AFM investigations of the surface morphology of Cu deposited films on SiO_2/Si(111) substrate. It can be seen that Cu grows as triangular islands [Figure.2.2(a)] with side lengths in the range of 300-500 nm. The height profile [inset: Figure.2.2(a)] taken along the line marked in the image shows the height of the island around 50 ± 10 nm. According to Zhang *et al.*., growth of Cu at 600^0C may not be single crystal (Zhou Zhang et al., 2008). This is apparent in the AFM image shown in Figure.2.2(a) where the surface seems to be uneven or rough

signaling mostly a polycrystalline nature of the film [24]. Detail investigations on the sample further reveal formation of triangular voids [Figure.2.2(b-d)] on the surface with varying dimensions. Smaller triangular voids [Figure.2.2(b)] have side lengths of the order of 100 nm, whereas, for larger triangular voids [Figure. 2.2(b, c)], it is of the order of 1.0-2.0 micrometer. Depth of the triangular voids varies from few (~10) nm for smaller ones to 100-200 nm for larger ones as revealed by AFM micrographs [Figure.2.2(b-d)]. Evidence of empty [Figure.2.2(b)] and partially filled triangular voids [Figure.2.2(c, d)] are also clearly seen in the AFM measurements. The line profiles taken across the voids [inset: Figure.2.2(b) and (d)] additionally corroborate the fact that the voids are either empty or partially filled. Occurrence of empty or partially filled voids is an indication of rapid growth of voids in the system. Such growth of triangular voids following the substrate crystal symmetry and growth of Cu on a relatively thicker SiO_2/Si is not yet reported according to our knowledge.

Formation of voids and the growth of Cu silicides through void filling mechanism were explored by Shauzhou Li and his coworkers (S. Li et al., 2010). They reported the growth of voids originating from the defect sites that are already present at the thermally grown SiO_2 on Si surfaces. A small amount of deposited Cu on SiO_2 at high temperature can form Cu_3Si which acts as a catalytic element and enhances the decomposition of SiO_2 in to SiO at the SiO_2/Si interface (Si + $SiO_2 \rightarrow$SiO (g)) (S. Li et al., 2010), (Cros, Aboelfotoh, & Tu, 1990), (H Dallaporta, M Liehr, 1990). This further promotes the formation of voids at the interface (S. Li et al., 2010). Initially the voids formed can have different shapes which may eventually grow to the morphology that is matching with the substrate symmetry (S. Li et al., 2010). The void structures play an important role in Cu-Si intermixing and can act as a template for the growth of islands (S. Li et al., 2010). Annealing at 450^0C can initiate the intermixing of Cu and Si and can facilitate the formation of the silicide nanocrystallites following the substrate symmetry (M. Seibt, M. Griess, A.A. Istratov, H. Hedemann, A. Sattler, 1998) through void filling mechanism in the presence of a native oxide barrier of 4 nm (Bo et al., 2010).

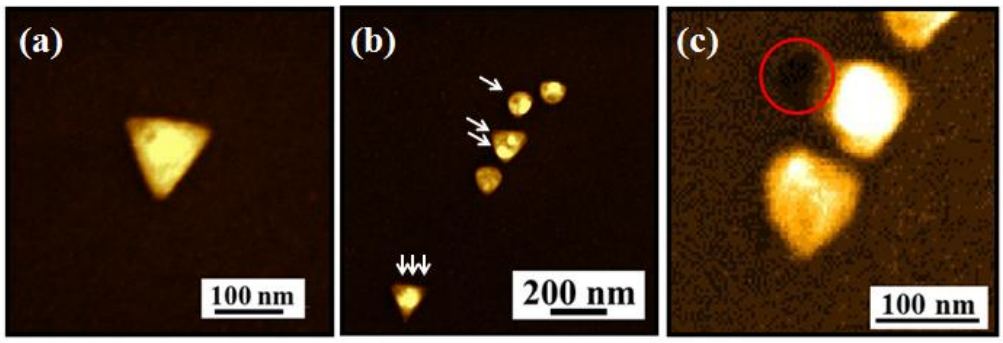

Figure.2.3. SEM micrographs of the nanoislands formed on the SiO_2/ Si(111)surface, (a) an individual triangular island and (b) array of spherical, partially formed triangular and fully formed triangular (denoted by single, double and triple arrows respectively) islands on Si substrate, (c) evidence of a half filled void is shown (marked inside red circle).

SEM investigations performed on the grown sample further validate the triangular morphology of the nanoislands [Figure.2.3(a), (b)] and the formation of half-filled voids [Figure.2.3(c), marked with circle] on the sample surface. The lateral dimension of the triangular islands in the SEM images is around 150 nm. We also see direct evidence of spherical (marked with single arrow), partially formed triangular (marked with double arrow) and fully formed triangular (marked with triple arrow) islands on the surface as shown in Figure.2.3(a, b). On an oxidized surface, because of its much lower surface free energy, growth of nearly spherical islands is expected (Anupam Roy, Bhattacharjee, Ghatak, & Dev, 2012). The spherical or nearly spherical islands [Figure.2.3 (b, c)] observed in the SEM micrographs are indeed smaller in dimension with diameter less than 100 nm compared to the triangular islands with side lengths around 150 nm or above [Figure.2.3(b, c)]. A smaller dimension of the spherical islands compared to the triangular ones and signature of partially grown triangular islands in the SEM images [Figure.2.3(b, c)] are direct manifestation of the evolution of islands from spherical to triangular shape and/or its preference to adapt shape following three-fold symmetries of the substrate and the

nanocrystals. Evidence of half-filled void seen in AFM [Figure.2.3(c,d)] and SEM investigations [Figure.2.3(c), marked with circle] is a clear demonstration of faster rate of growth of the voids than that of the nanocrystallites which is happening from void filling mechanism (S. Li et al., 2010).

From the AFM and SEM micrographs, we calculate the density of formation of triangular voids on the surface which is roughly in the range of 1-3 voids/100 μm^2. This number density includes formation of both smaller and bigger voids. We find that these voids are mostly either empty or partially filled [Figure.2.2(b, c, d)] and as a result formation of triangular nano crystallites on the surface is more than one order of magnitude less compared to the number density of the voids. The nano crystallites are mostly sparsely distributed on the surface as can be seen from the AFM and SEM micrographs [Figure.2.2 and Figure.2.3]. At the initial stage of growth, Cu-Si precipitates at the voids giving rise to small spherical islands due to a comparatively less surface energy of SiO_2 than Si which eventually grows as triangular nanocrystallites following the 3 fold crystal symmetry of the Cu as well as of the substrate to minimize the system energy through shape transformations (S. Li et al., 2010). However, the formation of voids, diffusion of Cu and the evolution of nanocrystallites will all be limited by the amount of Cu deposition, growth rate and annealing temperature, duration of annealing and thickness of the SiO_2 layer. In our case, even on a thicker oxide layer of 270 nm, we observe formation of triangular voids following substrate crystal symmetry and growth of triangular nanocrystallites through void filling mechanism which provide crucial insight related to fundamental studies on growth, a hitherto unreported observation for material growth on a substantially thicker dielectric. A schematic of the growth process is shown in the Figure.2.4.

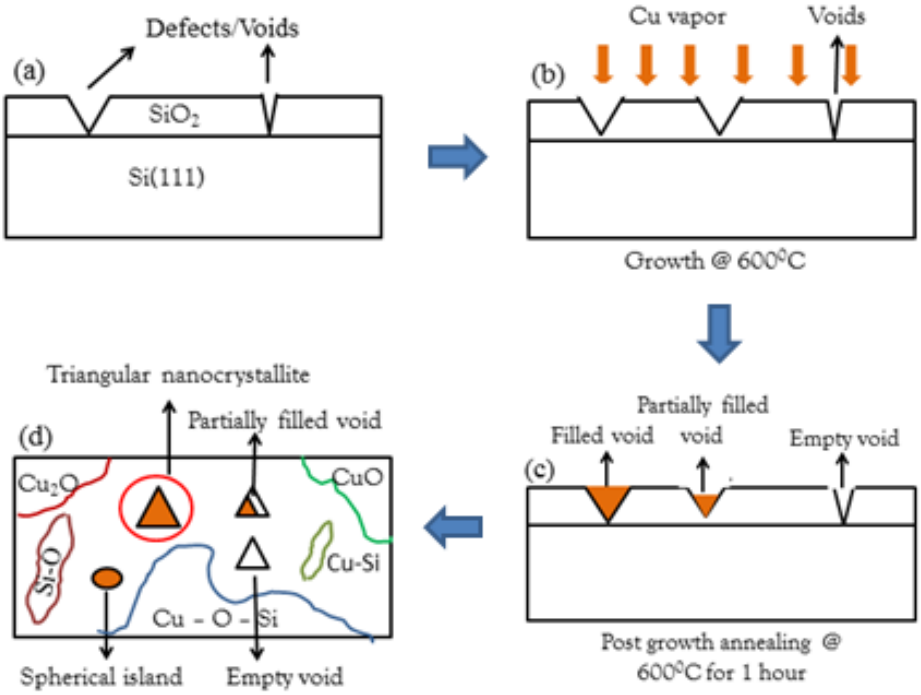

Figure.2.4. Schematic depicting the growth process of Cu on SiO_2/Si substrate. (a),(b), (c) Side-view of the growth process and (d) top-view

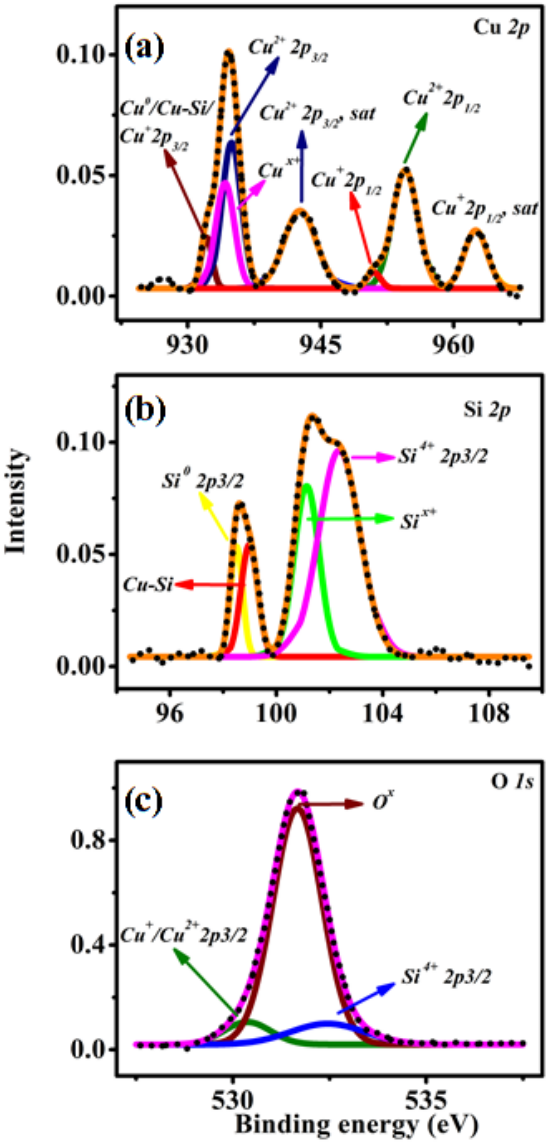

Figure.2.5. High resolution XPS spectra on the grown film. (a) Cu *2p*, (b) Si *2p* and (c) O *1s* core level peaks are shown.

XPS studies were carried out to further examine the elemental composition of the sample. Figure.2.5. shows XPS measurements carried out on the grown film. High resolution Cu *2p* [Figure.2.5.(a)], Si *2p* [Figure.2.5.(b)] and O*1s* [Figure.2.5.(c)] peaks, respectively from the XPS studies reveal various chemical compositions of the elements on the surface. Six different compositions are identified from the fit to Cu *2p* peak. The peak at 932.13 eV in Figure.2.5.(a), could be assigned to either metallic

Cu in the film or formation of Cu-silicide or Cu_2O in the sample (Sarkar et al., 1998), (Cros et al., 1990), (Chen et al., 2015). The position of Cu $2p_{3/2}$ peak in pure metallic Cu, in the silicide phase and in Cu_2O are reported to be very close to each other (Sarkar et al., 1998) ,(Cros et al., 1990) and as a result, it is usually difficult to resolve the signature of these states separately in the XPS spectrum. The peak centered at 934.2 eV, we assign to the formation of an additional mixed state of Cu-O-Si. The high intense peak centering at 934.95 eV in the spectrum may correspond to Cu^{2+} in octahedral coordination (Noelia Benito & Flores, 2017), (Kester et al., 1996). The peaks at binding energies of 934.95 eV and 942.67 eV we associate with Cu $2p_{3/2}$ in CuO and its satellite peak respectively (Noelia Benito & Flores, 2017), (Chen et al., 2015). The bands at the binding energies of 950.97 eV and 954.52 eV might be associated with Cu $2p_{1/2}$ from Cu_2O and CuO respectively (Chen et al., 2015). The last peak observed at 962.49 eV in the Cu *2p* spectrum is ascribed as Cu $2p_{1/2}$ satellite peak in Cu^{+} state (Chen et al., 2015), (Arellano et al., 2015), (Yongfan Wang et al., 2015). All the peak features corresponding to Cu *2p* band in Figure.2.5.(a) are relatively broad with FWHM falling in the range of 2.4 - 4.8 eV which also corroborate the formation of different Cu-oxide and Cu-silicide phases in the sample (Sarkar et al., 1998).

The XPS spectrum from Si *2p* band and the fitted curves are shown in Figure.2.5.(b). In the fitted spectra, the peak at 98.49 eV is assigned to Si $2p_{3/2}$ (E.'Sobol & Bomben, 1992), whereas, the peak at 99 eV, we associate to the formation of silicide phase in the sample (Sarkar et al., 1998), (Cros et al., 1990). The peak centered at 101.14 eV is attributed to Si^{x+} state, the presence of which might be due to formation of new additional state of Cu-O-Si after deposition of Cu (Noelia Benito & Flores, 2017). The peak at 102.36 eV corresponds to Si^{4+} state in the SiO_2 layer (Noelia Benito & Flores, 2017). A 1.8 eV of FWHM of this peak could be associated with Cu/SiO_2 interface formation (Noelia Benito & Flores, 2017). Binding energy of Si *2p* band in SiO_2 matrix can vary by 1.5 eV depending on the coordination number, oxidation states and chemical compositions during interface

formation (Noelia Benito & Flores, 2017). Therefore, the 102.36 eV peak feature, signature of the Si *2p* peak in the SiO_2 layer, could be associated with the modification of the chemical environment and subsequent formation of the interface after Cu deposition (Noelia Benito & Flores, 2017).

High resolution O *1s* peak and corresponding fitting of the data are shown in Figure.2.5.(c). Results obtained from the fit to O *1s* peak further substantiate the results obtained from Cu *2p* [Figure.2.5.(a)] and Si *2p* [Figure.2.5.(b)] high resolution XPS spectra. In the fitted data, the 1^{st} peak position centered at 530.37 eV is due to the formation of Cu_2O and CuO (Noelia Benito & Flores, 2017), (Zuo, Li, Han, & Huang, 2014) in the film. The peak centered at 531.67 eV represents an O^x state which could be due to the formation of a new mixed oxide state related to Cu-O-Si in the sample (Noelia Benito & Flores, 2017), (N. Benito & Palacio, 2014). The peak at 532.45 is coming from O in SiO_2 matrix (Noelia Benito & Flores, 2017), (N. Benito & Palacio, 2014) which is also observed as 102.4 eV peak in the Si *2p* spectrum as Si^{4+} state.

High resolution Cu *2p*, Si *2p* and O *1s* spectra and subsequent fittings help to develop our understanding about various chemical and structural phases formed due to deposition of Cu on SiO_2/Si(111) at 600^oC followed by a post growth annealing of the sample for 1 hour at the same temperature. The peaks at 932.13 eV in the Cu *2p* and at 99 eV in the Si *2p* spectra respectively indicate the formation of copper silicide (Geaney et al., 2012) in the sample. Formations of Cu^+ and Cu^{2+} oxide states are obvious from the peaks centering at 934.95 eV, 942.67 eV, 950.97 eV, 954.52 eV and at 962.49 eV in the Cu *2p* [Figure.2.5.(a)] and the peak at 530.37 eV in the O *1s* spectra. Interestingly, we see the emergence of a mixed Cu-O-Si phase which is apparent from the peaks centering at 934.2 eV in the Cu *2p*, 101.14 eV in the Si *2p* and at 531.67 eV in the O *1s* spectra. The results are consistent and could be validated by considering mainly three simultaneous interface processes: firstly, mixing of Cu and O to form the oxides; secondly, formation of the Cu-O-Si mixed phase and

thirdly, mixing of Cu and silicon to form the Cu-silicide phase. A qualitative estimation of the concentration of each phase, calculated from the area under the fitted curves in Figure.2.5., is shown in Table.2.1. As we can see, concentration of the mixed additional phase is the highest with more than 41%, in the film followed by Cu oxide which is around 29%.

Composition	Cu oxide ($CuO+Cu_2O$)	Cu-O-Si	Si-O	Cu-Si	Si
Concentration (%)	28.93	41.65	20.97	3.92	4.33

Table.2.1: Percentage concentration of various chemical phases present in the sample

When metallic copper is evaporated onto SiO_2/Si(111) at an elevated temperature and subsequently annealed, copper diffuses into the substrate. However, the diffusion and intermixing of Cu and Si are limited by the presence of SiO_2 layer and the temperature (Sekar et al., 1993). In our case, we have a 270 nm thick oxide over Si(111) as the substrate. The diffusivity of copper in intrinsic silicon is reported to be almost two orders of magnitude greater than that in SiO_2 (Istratov et al., 1998), (McBrayer, 1986). Thus, the SiO_2 layer acts as a barrier for Cu diffusion, promoting the oxidation of Cu over the formation of Cu silicide. The two main reasons for interface mixing of Cu and Si are solid state chemical reaction at the interface at an elevated temperature and the increase in diffusivity of Cu atoms in the Si matrix compared to the SiO_2 layer. The diffusivity of Cu in intrinsic Si is reported to be $(3.03 \pm 0.3) \times 10^{-4}\, e^{(-0.18 \pm 0.01)eV/k_B T}\ cm^{-2}/s$ and in SiO_2 it is $7.6 \times 10^{-6}\, e^{-1.82eV/k_B T}\ cm^{-2}/s$ (S. Li et al., 2010). However, diffusion of copper into silicon increases by an order of magnitude as the temperature is raised from RT to above 120°C (Ektessabi, 1993). When Cu atoms diffuse through the SiO_2 layer, it can combine with oxygen to form oxides during the process. The kinetics of oxidation depends on various factors like temperature, annealing time, *etc*. Even at a temperature as low as ~150^0C Cu is

reported to form oxides with Cu atoms in +1 oxidation state (Valladares et al., 2012). In general, we can get a mixed oxide phase with Cu in +1 and in +2 oxidation states at a temperature around 600^0C and a pure CuO (Cu in +2 state) at around 1000^0C (Valladares et al., 2012). Therefore, we expect the formation of Cu oxides in both +1 and +2 oxidation states. Our XPS results shown in Figure.2.5. indeed corroborate the fact that we have mixed oxide phases containing Cu_2O and CuO in the film. The higher concentration of Cu oxides compared to silicides might be due to a thicker SiO_2 layer interacting with Cu vapors to form oxides and the mixed chemical state involving Cu-O-Si bonds, thus limiting the interaction of Cu and Si. Benito *et al.*. (Noelia Benito & Flores, 2017) have studied the formation of Cu oxide states, mixed chemical states (Cu-O-Si) and silicide phases for varying Cu/Si ratio. According to their results the mixed chemical state of Cu-O-Si is formed for the lowest Cu/Si ratio with highest concentration. In our case, only around 60Å of Cu was deposited and as a result, it is quite likely that we get to see a substantial portion of the film (~41%) containing an intermediate mixed chemical state in the XPS data. It was proposed that the oxygen from SiO_2 substrate first reacts with Cu and forms a thin layer of Cu oxides and Cu-O-Si phase. In the Cu-SiO_2/Si interface, Cu^{x+} in Cu $2p_{3/2}$ is formed at a binding energy higher than that of Cu^+; O^{x+} is formed in O *1s* in between the binding energies of Cu_2O and SiO_2 and Si^{x+} in Si *2p* is formed at a binding energy below SiO_2, giving rise to an intermediate state of Cu-O-Si with a binding energy higher than that of Cu-O bonds and lower than that of Si-O bonds (Noelia Benito & Flores, 2017). Migration of Si atoms towards the surface is also an important phenomenon to form this intermediate state (Noelia Benito & Flores, 2017), (N. Benito & Palacio, 2014).

Growth of Cu silicide in the Cu-SiO_2/Si system is mainly governed by the thickness of the SiO_2 barrier and the temperature which would decide about the diffusion of Cu into Si to form Cu silicide. Voids present on the surface also play an important role to accelerate the formation of the silicide phase. The enthalpy of mixing of Cu and Si is almost the same at RT because of the similarity in their crystal

structure. Thus, the intermixing is not energetically favorable in such conditions (Shin et al., 2005). Cu-rich silicides (Cu_4Si, Cu_3Si) can be formed by the reaction between Cu layers and Si substrates covered by a thin silicon oxide layer of 2-4 nm during heat treatment in the temperature range of 600–750^{0}C (Benouattas & Mosser, 2000). The enthalpy of formation of the most stable Cu silicide (Cu_3Si) has been calculated to be -24.4 kJ/mol (Shin et al., 2005) at RT. The catalytic action of Cu silicide further helps in breaking Si-Si and Si-O bonds (which would otherwise occur at high temperature) which enhance the formation of new voids and facilitates more silicide formation. The extra silicide will then generate new defects at the SiO_2/Si interface promoting growth of more islands (M. Seibt, M. Griess, A.A. Istratov, H. Hedemann, A. Sattler, 1998). Our XPS data [Figure.2.5.] reveals a small concentration of the Cu silicide phase in the sample. This can be associated with the amount of deposited Cu (60Å) and the thickness (270 nm) of the SiO_2 barrier which are the critical parameters not only to determine the concentration of Cu silicide phase, but also the concentration of Cu oxide and the formation of the mixed intermediate phase. For a native SiO_2 layer of thickness 2-4 nm, the products would mostly comprise of silicide at an annealing temperature of 600^{o}C (S. Li et al., 2010).

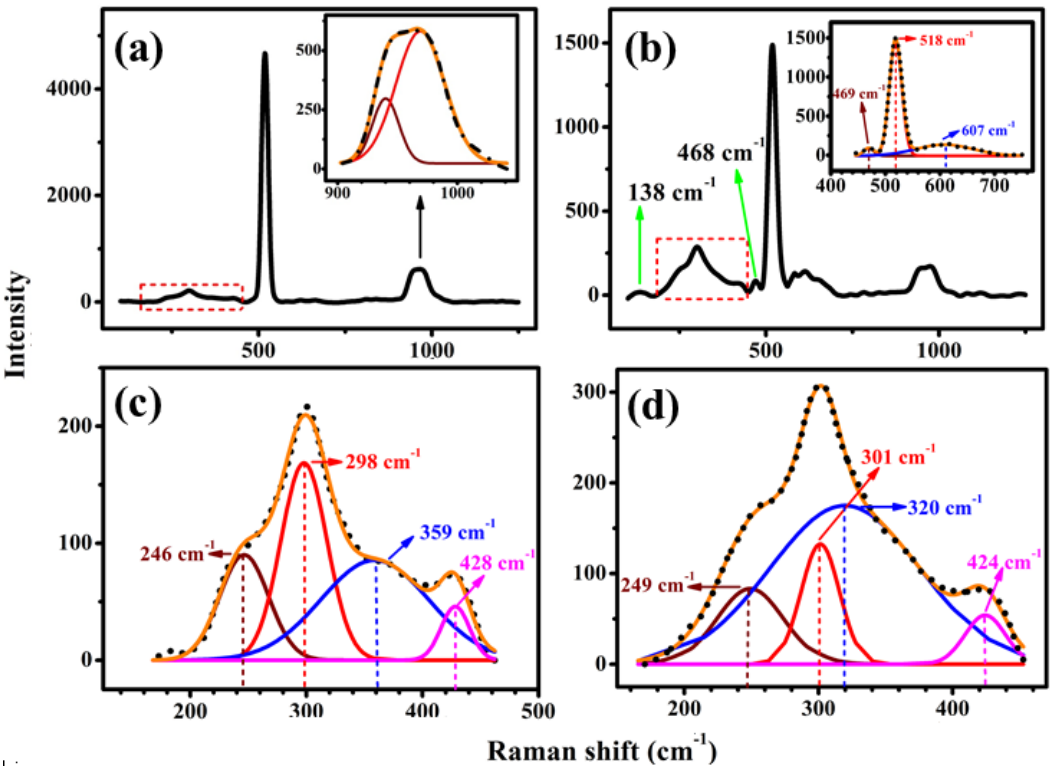

Figure.2.6. (a) and (b) show the Raman spectrum acquired from SiO_2/Si before and after Cu deposition respectively. Inset of (a) is the fitted data corresponding to 900 - 1000 cm^{-1} onset as marked by the arrow in the image. Inset of (b) is the fitted data corresponding to the onsets at 468 cm^{-1}, 518 cm^{-1} and the broad hump like feature adjacent to 518 cm^{-1} peak. (c) and (d) are the fitted Raman shifts marked by red rectangular boxes in (a) and (b).

Raman spectroscopy studies performed are shown in Figure.2.6. Figure.2.6(a) exhibits the Raman transitions from the SiO_2/Si substrate. The most intense Raman shift observed at 518 cm^{-1} is attributed to main one-phonon peak of Si (Kunimitsu Uchinokura, 1972), whereas, the relatively less intense broad band with a doublet feature observed between 900 to 1000 cm^{-1} with peak positions at 940 and 969 cm^{-1} is associated to two phonon overtone related to the optical branch of Si (Kunimitsu Uchinokura, 1972). We could resolve all the fine structures related to Si in between 200 to 450 cm^{-1} (Wright & Mooradian, 1967), (Kunimitsu Uchinokura, 1972), (Cowley, 1965), (Dolling & Cowley, 1966) by performing multi Gaussian peak fit to the experimental data [inset: Figure.2.6(a)]. These peak features observed at 246, 298, 359, 428 cm^{-1} associated with Rayleigh

tail correspond to optical phonon (Wright & Mooradian, 1967), (Kunimitsu Uchinokura, 1972), (Cowley, 1965),(Dolling & Cowley, 1966). Raman shifts observed in the Cu deposited film [Figure.2.6(b)] are somewhat displaced compared to the observed peaks on bare SiO_2/Si substrate along with signature of new peaks/onsets in the spectrum. Cu with FCC crystal structure does not have any Raman active modes. We observe peak features from the grown film [Figure.2.6(b)] at wave numbers 138, 249, 301, 320, 424, 468, 518, 627, 943 and 980 cm^{-1} which could be associated with various vibrational modes ascribed to the film and the substrate. The convoluted peak features in the Cu deposited film in the range of 200 to 450 cm^{-1} were de-convoluted in a similar fitting process considering Gaussian peaks discussed above. Features related to Cu oxidation are supposed to appear within ~630 cm^{-1}. Formation of Cu_2O in the system is validated by the presence of an onset at 138 cm^{-1} (Sarma et al., 2018). Raman shifts related to CuO should be seen at 297 and 626 cm^{-1} (Sarma et al., 2018), whereas, formation of CuO and Cu_2O mixed phase is reported to exhibit a broad feature peaking at 630 cm^{-1} (Sarma et al., 2018). From our fitted data [Figure.2.6(b):inset], we observe onset at 301 and a broad feature at 607 cm^{-1} which are shifted compared to the peak positions mentioned above for the CuO and the CuO and Cu_2O mixed phase. We associate these two features primarily with the formation of CuO and the Cu-oxide mixed phase respectively (Sarma et al., 2018). Since, the broad onset seen at 607 cm^{-1} in our case is shifted by quite a large amount of 23 cm^{-1} compared to the reported value of 630 cm^{-1} (Sarma et al., 2018), we also do not ignore the possibility of associating this feature with the formation of the Cu-O-Si intermediate phase. Peak feature observed at 469 cm^{-1} could be assigned to the emergence of Cu-silicide phase in the grown film (Z. Zheng et al., 2018). Fitted data in the range of 200 to 450 cm^{-1} for both the substrate and the film exhibit 4 peaks related to Si acceptors/donors electronic Raman transitions (Wright & Mooradian, 1967) among which the 428 cm^{-1} peak from the substrate could also be due to symmetrical Si–O–Si stretching modes principally involving motion of the oxygen atom for the SiO_2/Si substrate (Thermadam et al., 2010). We see shift in peak positions associated with change in intensity in the Raman transitions [Figure.2.6(c) and (d)] of the fitted spectrum

[200-450 cm^{-1}] for the grown film compared to the substrate which could as well be attributed to the formation of Cu-O-Si intermediate phase in the sample. From the Raman studies discussed here, evidence of formation of Cu-oxides and Cu-silicide is clearly established, however, it is difficult to comment certainly on the Raman active signatures of the Cu-O-Si phase as there is hardly any theoretical or experimental studies available so far related to this. However, we put these results here with a strong belief that they would provide important insight toward future investigations to develop proper understanding of the Raman transitions of the intermediate Cu-O-Si phase.

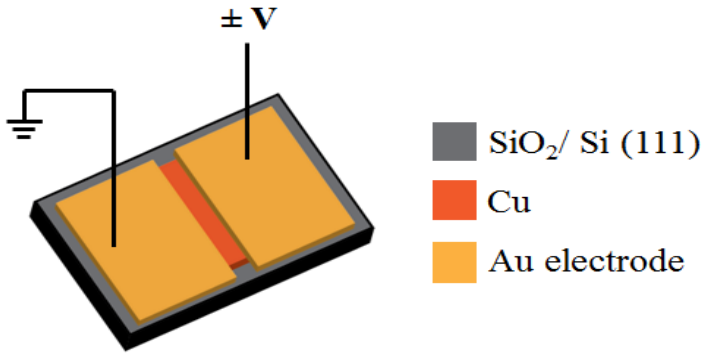

Figure.2.7. Schematic representation of the electrical measurements. The thickness of the Au electrode is ~140 nm.

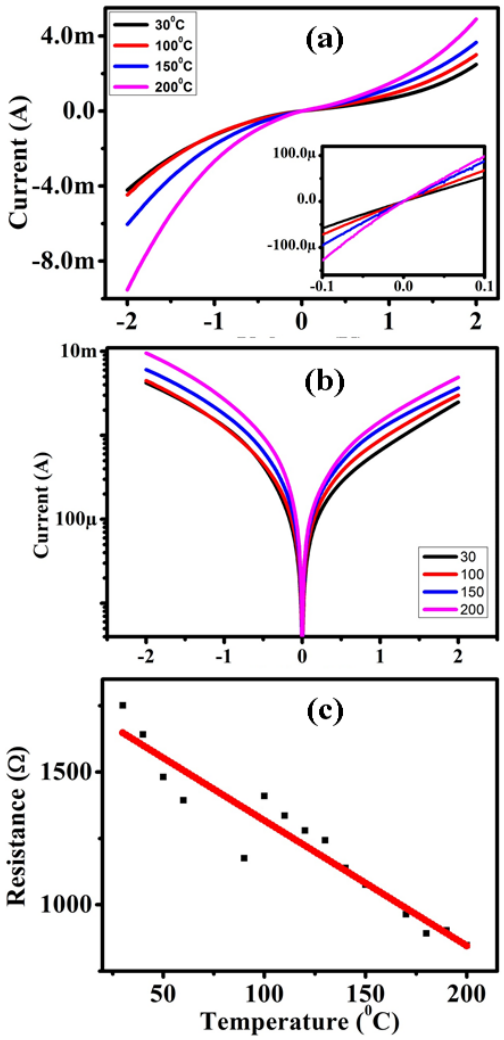

Figure.2.8. Two electrode electrical measurements performed on the grown film. (a) I-V characteristics of the sample for a temperature range of 30-200 ^{o}C. Ohmic nature of the sample around 0V is zoomed and is given as inset in (a). (b) Log I vs. V data exhibit a slightly more reverse current than forward. (c) Temperature dependent resistance of the film which shows a semiconducting like nature.

We have carried out preliminary electrical conductivity measurements of our sample to probe in general the electrical nature of the grown film using a two probe transport measurement set-up. A schematic of the electrical characterization setup is shown in Figure.2.7 and the experimental results are shown in Figure.2.8. 140 nm thick gold electrodes were deposited on the sample using thermal evaporation and the current-voltage (I-V) spectra were acquired between the two

electrodes separated by 1 mm channel, starting from RT up to an elevated temperature of 200^0C. Figure.2.8(a) shows such a set of I-V spectra acquired in the voltage range of -2 to +2 V. The I-V characteristics exhibit a non-linearity, presumably arising from the Schottky barrier between the Cu species and the Au contacts, as can be seen in Figure.2.8(a). The Ohmic nature of the contacts around zero bias is shown in the inset of Figure.2.8(a). The slope of the I-V curves increases with increase in temperature exhibiting highest slope at 200^0C indicating the lowest resistivity of the sample at this temperature. Sample resistances are calculated for different temperatures from the corresponding I-V spectra which show a linear trend with a negative slope in the resistance vs. temperature plot shown in Figure.2.8(c) indicating a semiconducting like behavior with more reverse current than forward [Figure.2.8(b)].

The additional phase of Cu-O-Si and the Cu oxide (Cu_2O + CuO) constitute together a substantial amount (more than 70%) of the film whereas the silicide phase is present in a small amount. Experiments performed based on electrical current measurements on metal silicides exhibit either metallic or semiconducting behavior (S. Li et al., 2010), (F. Zhou et al., 2007), (Mattheiss, 1991). Cu silicides usually come under metallic silicides (S. Li et al., 2010). Cu oxides (both in +1 and +2 states), on the other hand, are *p*-type semiconductors with an energy band gap of 2.1 eV for Cu_2O and 1.21-1.51 eV for CuO (Valladares et al., 2012). However, a very little is known so far about the electrical characteristics of the Cu-O-Si phase. The RT resistivity of CuO is in the range of 0.01-1 Ω-cm, Cu_2O is in the range of 10^{3-8} Ω-cm and Cu_3Si is 55-60 μΩ-cm, whereas intrinsic Si has a resistivity of $3.2x10^5$ Ω-cm. The RT resistivity in our case is in the range 0.105 Ω-cm which is close to the resistivity of the CuO. The electrical measurements performed on our sample would mostly be a cumulative effect, albeit, would be dominated by the characteristics of the main phases formed. There will be various possibilities about the distribution/arrangement of the domains related to Cu-oxides, Cu-O-Si and Cu-silicide phases in the film which is impossible to comment. The domains of Cu-O-Si as well as Cu-oxides, main phases formed in the film, could be either connected

to each other or sparsely distributed and depending on that the electrical nature of the film would vary. The nano crystallites formed here are anyway sparsely distributed and mostly cannot participate in forming the electrical path. We attribute these preliminary studies of I-V characteristics and the associated temperature dependent electrical resistivity of the grown film to the collective behavior of the sample. All Cu oxides are semiconducting. Cu-O-Si mixed phase has unknown electrical properties. We found that the film contains mostly the mixed phase. Hence, in principle the electrical properties should be dominated by the mixed phase. Since we do not observe metallic behavior in the electrical characterizations, this signifies that the mixed Cu-O-Si phase is mostly not metallic. This also indicates about the amount of Cu-silicides in the film which is less and mostly scattered throughout, thus, could not provide any metallic path. From all these, we elucidate that the grown film does not exhibit any metallic nature which is governed mostly by the Cu-O-Si intermediate and Cu-oxide phases in the sample.

2.4. Conclusion

Growth and interaction of Cu at 600^{o}C on a 270 nm thick SiO_2 layer on Si(111) substrate have been investigated. We find growth of triangular voids on the surface following substrate crystal symmetry. Upon deposition, Cu grows as triangular islands *via* void filling mechanism through diffusion and segregation where 3 fold crystal symmetry of the Cu as well as of the substrate gets reflected on the morphology of the island growth. Along with Cu oxides and Cu silicides, we report the formation of an intermediate Cu-O-Si phase in the grown film. XPS data reveal that this new intermediate Cu-O-Si phase dominates the composition (as high as ~ 41%). XPS data also reveal a small percentage of silicide phase in the film. Formation of all these phases could be associated with the annealing temperature, thickness of the SiO_2 barrier, amount of deposited Cu, diffusion of Cu in the SiO_2/Si system and migration of Si towards the surface. Preliminary electrical characterizations performed on the film show an overall behavior of the film which is not metallic. This also indicates that mostly the intermediate mixed

Cu-O-Si phase which constitutes a substantial amount of the sample might not also be metallic.

CHAPTER 3

SYNTHESIS OF MoS_2 NANOSTRUCTURES AND INTERACTION WITH ELECTRON BEAM: A GENERAL OVERVIEW

This chapter deals with the review on the exfoliation techniques used for isolating the layers of 2D materials, especially, MoS_2. We have done a brief literature survey on the liquid phase exfoliation of 2D layered materials, the main criteria involved in the selection of solvent etc.. Synthesis of nanostructures of MoS_2 using top down approach, influence of MW energy in the formation of the nanostructures, interaction of electron beam with 2D materials and the associated structural phase transformations are the main topics which will be discussed briefly.

3.1. Introduction

The necessity to integrate miniaturized device structures with better performance in the integrated circuits (IC) has always made researchers to look for new materials with exotic properties. The scientific community was hugely overwhelmed by the isolation of graphene from graphite and investigations of the electronic and electrical properties of graphene carried out by Novoselov and Geim (Geim & Novoselov, 2007). These led them to the prestigious Nobel award and instigated curiosity among researchers for 2D layered materials and their properties. Graphene - an sp^2 hybridized carbon allotrope in the form of 2D sheet with hexagonal arrangement of atoms exhibits extraordinary electronic, electrical, mechanical properties which are drastically different than its bulk counterpart graphite. However, technological applications of graphene which is somewhat limited by its semi metallic zero band gap nature for electronic device implementations like switching etc., has led to a completely new field of research called 2D materials. Recent trend in materials research is to find new layered materials with sustainable superior qualities where, by controlling the layer thickness, one could tailor their properties according to the will. In this regard, TMDs have received enormous attention recently.

Research interests on bulk TMDs like MoS_2 dates back several decades due to its striking mechanical properties caused by the vdWs interaction present between the layers. The structure of MoS_2, was determined back in 1923 (Dickinson & Pauling, 1923). Bulk MoS_2 was mainly used as a dry lubricant, although it also had 'electronic' applications, e.g. as an anode in lithium-ion batteries (Stephenson, Li, Olsen, & Mitlin, 2014). The observation of a direct band gap in monolayer MoS_2 (Mak, Lee, Hone, Shan, & Heinz, 2010) and the associated high yield in emission triggered a huge research interest to look for other semiconducting TMDs with direct band gap which can be exfoliated easily. Depending on the structural arrangements and stackings, presently there exists a variety of layered materials starting from semiconducting TMDs of MoS_2, WS_2 to insulating hBN. Broad range of diversified properties exhibited by this material

class is mainly because of the existence of the out-of-plane *d* orbitals which are not bonded and the degree to which they are filled (Kolobov & Tominaga, 2016).

The main strategies for the production of atomic thin 2D TMDs and their nanostructures include both bottom up and top down methods. Bottom up techniques produce defect free high quality TMD layers. Hence, these are widely used in nanoelectronics and nanodevices. As the name suggests, bottom up methods involve synthesizing large area uniform layers starting it from the smallest components of atoms or molecules (Ciesielski & Samorì, 2014). Single-layer TMDs via bottom up strategy can be formed by chemical vapor deposition (CVD) (Y. H. Lee et al., 2012), (X. Wang, Feng, Wu, & Jiao, 2013), thermal evaporation (Balendhran et al., 2012), (Y. C. Lin et al., 2012), pulsed laser deposition (PLD) (Zabinski, Donley, Prasad, & McDevitt, 1994) or other ultra high vacuum (UHV) approaches (Kibsgaard et al., 2006), (Lauritsen et al., 2007) out of which, CVD is the most widely utilized to produce high-quality single-layer TMDs. Even though large area uniform layer synthesis is possible by bottom up methods, the tedious task of precise growth and transferring them onto desired substrate for industrial applications is often difficult.

Top down strategy relies on techniques such as mechanical cleavage (Mak et al., 2010), (Splendiani et al., 2010b) liquid-phase exfoliation by sonication in appropriate liquids (J. N. Coleman et al., 2011), (K.-G. Zhou, Mao, Wang, Peng, & Zhang, 2011) intercalation of TMDs by ionic species followed by liquid exfoliation (Eda et al., 2011), (J. Zheng et al., 2014) electrochemical ion-intercalation and exfoliation (Yichao Wang et al., 2013), (Zeng et al., 2011), ball milling (Kouroupis-Agalou et al., 2014) and laser thinning technique etc. (Castellanos-Gomez et al., 2012). The top down “scotch tape” or mechanical exfoliation method is very useful to peel off high quality single-layer sheets from the bulk crystal as mentioned before, however, limited by lower yield and size uniformity (Q. H. Wang, Kalantar-Zadeh, Kis, Coleman, & Strano, 2012). Compared to the mechanical cleavage, liquid based techniques usually do not require extreme synthesis conditions, and allows the production of nanosheets

with high yield. The separation of layers is aided by direct sonication in an appropriate solvent to obtain mono/few layers. This method is dominant over the mechanical exfoliation owing to its scalability and versatility, moreover, with the possibility of exfoliation in easily available common solvents. Mass production of exfoliated 2D TMD layers can also be achieved by electrochemical ion-intercalation and exfoliation in which, the electronic structure of TMDs can be electrochemically tuned by the diffusion of intercalated ions (Li^+, Na^+, K^+) by means of a discharge process (Yichao Wang et al., 2013), (Zeng et al., 2012). Nevertheless, the control of ion intercalation, amount of ions inserted and also, the structural deformation induced in the TMD sheets poses a serious issue in this technique.

The materials, thus, synthesized are comprised of nanostructures and 2D sheets which require in-depth investigations from structural aspects to understand various intrinsic properties related to electronic, electrical, optical and mechanical exhibited by these low dimensional structures owing to their crystallinity, size, shape and morphology. For the precise investigations related to structural arrangement requires instrumental techniques providing atomically resolved pictures with single atom precision. Electron microscopy techniques employed for this purpose involves scanning the material surface with an electron beam. Usually, even at low voltages, these electron beams can induce structural damages in 2D materials. State of the art, transmission electron microscope (TEM), usually uses electron beam of energy ranging from as low as 20 keV to as high as 300 keV. To perform high resolution TEM (HRTEM) measurements for capturing images at the atomic level, one requires an electron beam of energy of around 200 - 300 keV. Such high energy beam can cause irreversible damage in the crystalline structure of the 2D sheets. Hence, it is highly essential to look for thin 2D sheets which can withstand such high beam energies and remain structurally stable.

This chapter is organized as follows, the first section discusses briefly the structural polytypes of TMDs and the band structure. This will be followed by a

introduction to the TMDs synthesis procedure with special focus on the physics behind the LPE process. Since, in this thesis we have taken a simple facile route of LPE to achieve MoS_2 nanostructures and 2D sheets, our main discussion will focus on various processes related to the synthesis of 2D materials and low dimensional structures by LPE. In the third section, the recent development of LPE of 2D materials especially TMDs, in general will be reviewed. In the fourth section, we will discuss mainly about the synthesis of nanostructures of TMDs using LPE, followed by a discussion of the synthesis method which we have taken for our work. The fifth section in this chapter will discuss about the fundamental mechanisms underlying the interaction of electron beam with materials and also the structural changes which the beam can impart onto layered 2D materials.

3.2. Structure of TMDs:

TMDs can be generally represented with the formula MX_2, where M represents the transition metal atom and X represents the chalcogen atoms. These atoms are stacked one upon the other in the form X-M-X and one such stack corresponds to a monolayer of TMDs. These monolayers stacked vertically can realize the bulk TMDs. The intralayer bonding (ie, bonding between X and M within a layer) is covalent whereas interlayer (between two monolayers) is the weak vdWs force. This weak interlayer bonding enables the easy separation of layers into mono/few layer regime.

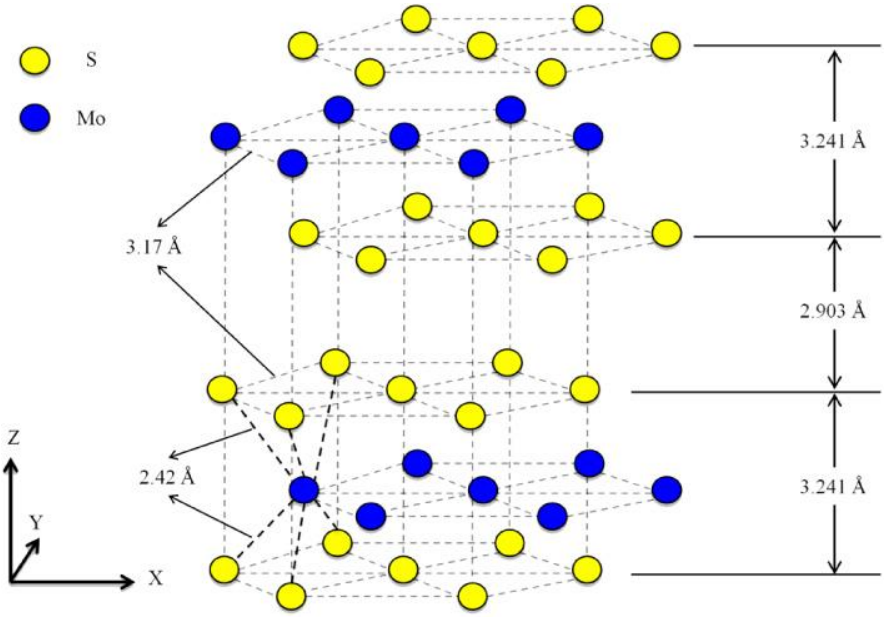

Figure. 3.1. Schematic depicting the arrangement of atoms in monolayer MoS_2. (Taken with permission from (Stewart & Spearot, 2013)

A typical monolayer of a TMD material is shown in the Figure.3.1. Each layer consists of hexagonally arranged metal atoms which are sandwiched in between two layers of chalcogen atoms arranged in honeycomb fashion. So individually if considered, each atomic plane has a hexagonal symmetry. The thickness of each such stack comes around 6-7 Å which constitutes a monolayer of TMDs.

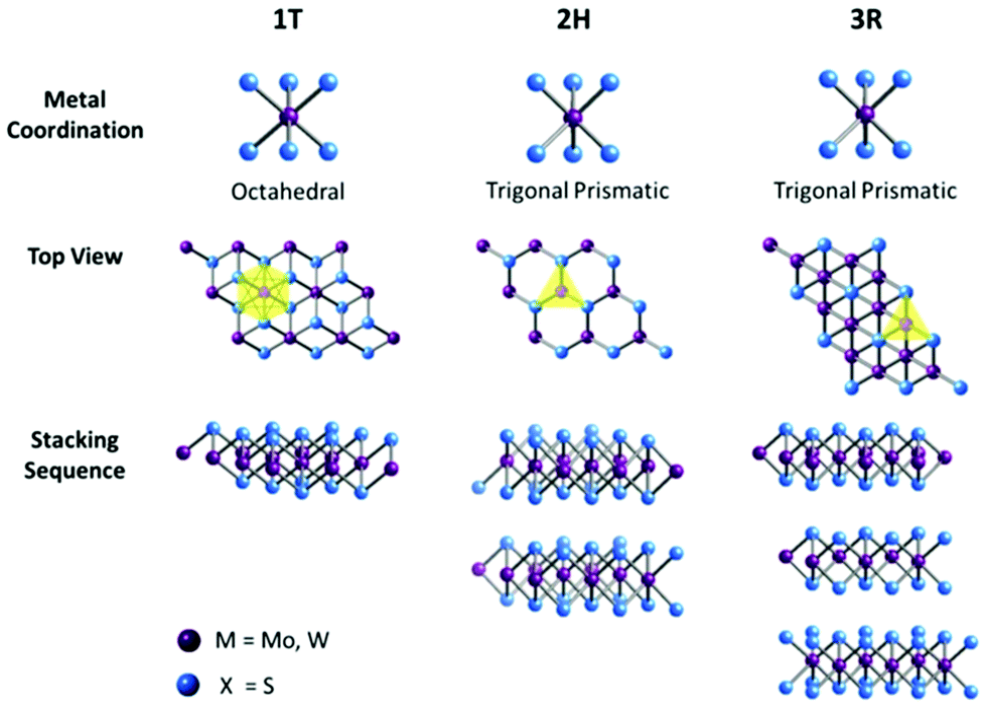

Figure.3.2. Schematic showing the different polymorphic forms of TMDs. The metal atom coordination as well as the sequence of stacking of monolayers is depicted (Taken with permission from (Toh, Sofer, Luxa, Sedmidubský, & Pumera, 2017).

As discussed earlier, the TMD monolayer can exist in either trigonal prismatic or octahedral symmetry (Figure.3.2.). Based on this, bulk TMDs can usually exist in three polymorphic structures, 1T, 2H and 3R where the number indicates number of layers in bulk unit cell and letter indicate the crystal symmetry (T- trigonal, H- Hexagonal, R- Rhombohedral). The unit cell is defined by 3 parameters namely ‘c’ which lies perpendicular to the layer, and the ‘a’ and ‘b’ axes which lies along the minimum chalcogen- chalcogen distance. The trigonal prismatic configuration has a D3h symmetry.

The 2H bulk polytype can assume two forms have different stacking symmetries. In $2H_a$ (AbA/CbC) stacking, transition metal atoms in one layer are located on top of transition metal atoms of the neighbouring layer. This polytype is reported to occur in $NbSe_2$, NbS_2,TaS_2, and $TaSe_2$ crystals. The $2H_c$ polymorph is characterised by the CaC/AcA stacking, i.e. any transition metal atom is located on top of two chalcogenides atoms of the subsequent layer. This polytype occurs

in MoS_2,WS_2, $MoSe_2$, and WSe_2 crystals. Both the polytypes belong to non symmorphic hexagonal space group $P6_3/mmc$ (Wilson & Yoffe, 1969).

The 1T polytype is constructed by piling up single layers, with one transition metal atom (or chalcogen atom) located on top of another transition metal atom (or chalcogen atom), in an octahedral coordination. In bulk, stacking of 1T phase follows D^3_{3d} symmorphic space group with unit cell comprising of 3 atoms. In 2H phase, the symmetry in few layer structures depends on the number of layers (even or odd) whereas, in 1T phase, since the layers are all identical, the symmetry operations do not change with layer thickness (Kolobov & Tominaga, 2016).

The 3R phase is usually formed under special conditions like extremely high pressure and high temperatures (Towle, Oberbeck, Brown, & Stajdohar, 1966). Hence, naturally occurring TMDs usually exist in 2H phase only. Synthetic MoS_2 usually contains 3R phases. In both 2H and 3R phase the metal atoms exist in trigonal prismatic coordination.

3.3. Electronic band structure

The bonding in TMDs is slightly different from the conventional covalent bonding. The bonding occurs between the empty orbital of metal and lone pair (LP) of chalcogen atoms. Metal atom provides 4 electrons to fill the bonding states and the metal atom and chalcogen atom thus acquires a charge of +4 and -2 respectively (Chhowalla et al., 2013). The chalcogen atoms are generally sp^3 hybridized with the LP electrons pointing outward the plane of atoms. These LP electrons of the chalcogen atoms terminate the TMD surface thereby making the surface very stable. The nine metal orbitals and six chalcogen orbitals combine to form six bonding and six antibonding orbitals. The material's properties are governed by the population of electrons in the non bonding level and lower anti bonding levels. The coordination number of metal atoms is determined by the size of the metal atom, the number of *d* electrons etc. Although coordination numbers

from 2-9 are known, the metal atoms within the triple atomic layer of TMD monolayer are six-fold coordinated and can exist in trigonal prismatic or octahedral symmetry. In the prismatic arrangement, chalcogen atoms of different planes are stacked one on top of the other whereas in the octahedral arrangement it is distorted. The preferred symmetry depends mostly on the *d* electron count of the transition metal and also to the size of the atom upto an extent.

As a result, the electronic structure of TMDs largely depends on the d electron count and coordination geometry. For both 2H and 1T phases, the non bonding d- bands of TMDs lie between the bonding (sigma) and antibonding (sigma*) bands. For octahedral coordination, two degenerate orbitals, consisting of d_{x^2} and $d_{x^2-y^2}$ orbitals and t_{2g} consisting of d_{xy}, d_{yz}, d_{xz} orbitals, are formed. In the trigonal prismatic arrangement on the other hand, the orbitals split into 3 groups, a1, e and e` consisting of d_{z^2}, $d_{x^2-y^2} + d_{xy}$ and $d_{xy} + d_{xz}$ respectively.

The electronic properties arise from the mode in which these orbitals are filled. For partially filled highest orbital, the material behaves as a metal, whereas, for fully filled orbitals, semiconducting behaviour is observed. In the presence of chalcogen atoms, the d bands broaden with an associated decrease in band gap. However, the properties of the material is affected mainly by the transition metals and the influence of chalcogen atoms is almost negligible.

The weak interlayer vdWs attraction facilitates the easy exfoliation of TMDs into individual layers. A unique characteristic of TMDs is their thickness dependent electronic properties. This behaviour came into limelight after the investigation on luminescence property of MoS_2 with layer thickness was reported by Mak *et al.* (Mak et al., 2010) and Splendiani *et al.*, in 2010 (Splendiani et al., 2010a). The origin of such a behaviour stems from the band structure cross over. As the thickness gets reduced from bulk to monolayer, the band gap changes from indirect to direct causing the origin of unique properties in TMDs.

3.4. Liquid Phase exfoliation via sonication

LPE of layered materials usually involves three steps: (i) dispersion of bulk material in a suitable liquid, (ii) exfoliation via sonification, and (iii) purification/separation of isolated few/mono layered sheets from the dispersion. One of the widely used method for exfoliation is ultrasonication, where, the cavitation and shear forces produced due to the propagation of ultrasonic waves aids to the separation of layers. These as produced sheets need to be stabilized by minimising the interfacial tensions, which hugely depends on the choice of liquid medium chosen for the exfoliation. Choice of poor liquid medium leads to the restacking of the exfoliated layers with increase in time.

During ultrasonication of materials, acoustic cavitation is demonstrated which has simultaneous effects on the related sonochemical events. According to these phenomena, the sonication process has been divided in different steps: i) generation of nuclei on cavitation bubbles; ii) bubble growth due to gas diffusion; iii) damage of bulk materials due to intense shock-waves or high-speed jets; iv) formation of high-velocity interparticle collisions and; v) increase of surface area of solid materials because of their fragmentation (Suslick, 1995), (H. Xu, Zeiger, & Suslick, 2013). Thus, several parameters need to be considered for an effective and scalable sonication process including sonication time and cavitation intensity. We briefly discuss below few of these parameters which are responsible towards providing scalable nanostructures especially related to our synthesis process.

3.4.1. Criteria for the selection of solvent

For the case of 2D layered materials, the core mechanism of the LPE process is based on solution thermodynamics. Assuming that dispersions can be considered as solutions, the free energy of mixing (ΔG_{mix}) is given by

$$\Delta G_{mix} = \Delta H_{mix} - T\Delta S_{mix}$$

where, ΔH_{mix} is the enthalpy of mixing and ΔS_{mix} is the entropy of mixing (Bernal & Milano, 2014). The mixing is favourable for a negative ΔG_{mix} which can be ascertained by a large value of ΔS_{mix}. For larger area nanosheets, which are normally produced by LPE, ΔS_{mix} is considerably small. Hence, minimising ΔH_{mix} is the only viable option in order to obtain a stable dispersion (J. N. Coleman et al., 2011), (Jonathan N. Coleman, 2009), (Cunningham et al., 2012).

A thermodynamic modelling approach was employed by Bergin *et al.*. (Bergin et al., 2008) to investigate the exfoliation process of carbon nanotubes in solvents. Later, the same approach was adapted by Cunningham (Cunningham et al., 2012) and his coworkers as an extension towards vdWs interaction under solvent conditions and expressed the enthalpy of mixing per unit volume of mixture as;

$$\frac{\Delta H_{mix}}{V} = \frac{2}{T_{NS}} \left(\sqrt{\gamma_{NS}} - \sqrt{\gamma_{sol}}\right)^2 \Phi$$

where V is the volume of the mixture, T_{NS} is the nanosheet thickness, γ_{NS} and γ_{sol} are the surface energies of nanosheet and solvent respectively, Φ is the dispersed nanosheet volume fraction. From the above expression, it is quite evident that the ideal dispersion condition is when surface energy values of nanosheet and solvent are close.

It has been established that for successful LPE of layered materials require solvents with surface tension in the range of 40 - 50 mJm^{-2} (J. N. Coleman et al., 2011). Unfortunately, these solvents present different inconveniences such as toxicity and high cost. Besides, future processing of the dispersions is a tricky issue owing to their high boiling point, challenge for characterization and future processing of the dispersions.

Although the surface energy of some solvents matches those required to form a stable dispersion, the concentration of dispersed nanosheets is quite low which demands the incorporation of surface tension as a crucial solubility

parameter (Cunningham et al., 2012). Hansen solubility parameters (HSP) takes care of all these factors and aids to an accurate prediction of molecular affinities, solubility and its related phenomena (Jonathan N. Coleman, 2009). Here, each molecule is assigned with the parameters arising from the following forces; (i) dispersion forces (δ_D), (ii) dipole forces (δ_P), and (iii) hydrogen bonding (δ_H). The basic notion of HSP concludes that if the solubility parameters of both solute and solvent does not vary too much and lies in the same range, they will have high affinity and will dissolve. Taking each of these parameters as coordinate, a material's solubility can be characterised as the distance between its location to the point representing the solvent. This relation can be described as,

$$R= \sqrt{4(\delta_{D,sol} - \delta_{D,NS})^2 + (\delta_{P,sol} - \delta_{P,NS})^2 + (\delta_{H,sol} - \delta_{H,NS})^2}$$

R is the interaction radius $\delta_{D,sol}, \delta_{P,sol}, \delta_{H,sol}$ and $\delta_{D,NS}$, $\delta_{P,NS}, \delta_{H,NS}$ are the dispersion, polar and H bonding for solvent and nanosheets respectively. The smaller the interaction radius, the greater would be the solubility.

In case of a multi component system, HSP parameters can be obtained as follows.

$$\delta_{blend} = \sum \varphi_{compn} \delta_{compn}$$

Where $\varphi_{compn} and \delta_{compn}$ are the volume fraction and the intrinsic HSP parameters of the particular solvent in the combination.

3.4.2 Multi solvent system- Cosolvency technique

As mentioned in previous section, the normally used solvent for LPE pose a drawback owing to their high boiling point. Due to this issue, solvents like water, low boiling point solvents like acetone, chloroform etc. can be used as an alternative. But with these solvents, 2D materials do not generally bond much to form a stable dispersion. This led to the investigation on mixed solvent systems for successful exfoliation of layered materials.

The cosolvency system were initially utilized for a system of cellulose nitrate where it has been observed that a pair of non- solvents could effectively act as a good solvent for polymer dispersion when mixed in a specific ratio (K.-G. Zhou et al., 2011). A classic example of the cosolvency phenomenon is observed for thermoplastic polymer dispersions formed in a mixture of carbon tetrachloride and an alcohol [34]. Such a study can be extended towards 2D layered materials exfoliation due to the weak vdWs interaction between the layers. The first reported study was by Zhou *et al.*. for the efficient exfoliation of transition metal dichalchogenide (TMD's) in an appropriate solvent mixture of ethanol and water based on HSP parameters [42]. Later on, numerous studies have been carried out on cosolvent systems, which will be discussed in the following sections.

3.4.3 Purification of the sample

After the sonication process, most of the material present in the dispersion would be having varying thickness and sizes. These can be separated by various approaches based on differential centrifugation processes (May, Khan, Hughes, & Coleman, 2012), (O'Neill, Khan, & Coleman, 2012). For graphene dispersions, Coleman and his coworkers have suggested a successive centrifugation, separations and redispersion process for isolation of sheets with varying sizes. It has been observed that the higher the centrifugation rate, the smaller will be the flake size (O'Neill et al., 2012), (Backes et al., 2014). Also, the separation by centrifugation mostly depends on the concentration of material in the dispersion as well.

3.5. Liquid phase exfoliation of TMDs

Layered TMD materials have received tremendous attention recently owing to their structural polymorphs, electrical and electronic properties. The composition and arrangement of atoms in mono layers as well as the dimensionality govern the potential applications of these 2D materials (Mak et al., 2010), (Lv et al., 2015). Exfoliated TMDs are chemically reactive and hold

inimitable electronic, electrochemical and optoelectronic properties (Eda et al., 2011), (Q. H. Wang et al., 2012), (Two-dimensional et al., 2014) as a result of their high surface area and quantum confinement effects (Lv et al., 2015), (Chhowalla et al., 2013), (M. Xu, Liang, Shi, & Chen, 2013) which are not spotted in their bulk counterparts. However, these properties of exfoliated layers have a strong correspondence with the layer thickness i.e. number of mono layers in the stack.

LPE is considered as an easy and scalable technique to obtain mono/few layer(s) TMD in an extensive list of solvents. Various TMDs like MoS_2, WS_2, $MoSe_2$ etc. has been exfoliated in a number of solvents with varying surface tensions by Coleman and his group (J. N. Coleman et al., 2011). They concluded by rigorous optical absorption spectroscopy studies that the amount of material in the dispersions increases with the reduced mismatch in surface tensions of solvent and bulk material. Later on, investigations were carried out to understand the dispersion of 2D material in terms of the solubility parameters (Cunningham et al., 2012).

Coleman *et al.* extended the work by using N methyl pyrollidine (NMP) to form MoS_2 dispersions and provided a method for separation of fractions of dispersions w.r.t. to their sizes by modifying the initial concentration and also centrifugation time. Acetonitrile being a polar solvent dissolves a wide range of ionic and non-polar compounds. It physisorbs on to MoS_2 surface thereby weakening the vdWl's forces facilitating easy exfoliation (Pachauri, Kern, & Balasubramanian, 2013).

Water offers the advantage as a solvent in terms of its cheap availability and non toxic nature, However, similar to other 2D materials, exfoliation of TMDs in water is quite difficult, and requires a stabilizer or surfactant for successful exfoliation. Backes *et al.*, (Backes et al., 2014) used sodium cholate as surfactant, similar to the investigations carried out by Smith and group (Smith et al., 2011), but additionally used centrifugation based methods to isolate the dispersion fraction w.r.t. their lateral sizes. When non– ionic surfactants were utilized, more concentration of mono/few layers were obtained for MoS_2 and WS_2

(Guardia et al., 2014). Even though based on solubility parameters, pure water based exfoliation is reported to produce unstable dispersions, Forsberg (Forsberg et al., 2016) has reported in 2016, a formation of stable MoS_2 dispersion in pure water without any additives. They have observed a stable dispersion even after a time period of 4 months (Forsberg et al., 2016). However, a temperature controlled stable dispersion of 2D materials like graphene, h-BN, MoS_2, WS_2 and $MoSe_2$ in pure water was reported earlier by Kim and his coworkers in 2015(Kim et al., 2015). In general, it has been observed that high temperatures favour both exfoliation and dispersion stability. Recently in 2018, a similar investigation was carried out to understand the mechanism of dispersion of MoS_2 in water by Ma (H. Ma, Shen, & Ben, 2018) and his group and upon rigorous investigations, concluded that the dispersion stability increases with increasing centrifugation time thereby producing flakes with small lateral sizes.

More than 60 solvents were tested as solvents for the exfoliation of 2D materials including graphene. However, from all these reported solvents, NMP still stands out as the best solvents for the 2D materials when sonication without any added stabilizer is the synthesis method. The possible cons that can be highlighted for this solvent is the high boiling point and the hygroscopic nature whereby, it absorbs moisture and thus can cause the destabilization of the dispersion. Low boiling point solvents suffer from the issue of low yield which makes them practically of limited use in the technological applications. In this scenario, the mixed solvent could be considered as a strategy to enhance the exfoliation efficiency.

The mixed solvent or co solvent approach was discussed by Zhou and his co workers (K.-G. Zhou et al., 2011) using volatile solvents with assuring advantages in terms of cost, toxic level, and solvent removal after the synthesis procedure. A useful method for TMDs that cannot be exfoliated in common solvents was reported by May *et al.* (May et al., 2012) who suggested dissolved polymers for this purpose. It can also facilitate the formation of polymer nanocomposites. In the similar fashion, the cosolvency technique was used for exfoliating TMDs by Udayabagya Halim and coworkers with water alcohol

combination (Halim et al., 2013). It was observed that the exfoliation rate increased up to a particular solvent ratio and after that, the rate reduced (Halim et al., 2013).

It has been observed that addition of iso propyl alcohol (IPA) or t- butyl alcohol can significantly enhance the dispersion capability of water for the case of graphene and MoS_2. For the exfoliation of WSe_2 in water various alcohol cosolvents were examined and alcohol–water mixing rate was optimized to be 30%, 60% and 70% for IPA, methanol and ethanol respectively (K.-G. Zhou et al., 2011). An increase in exfoliation rate was observed for both graphene and MoS_2 by an addition of hydrazine (N_2H_4) compared to those in the reference organic or surfactant water solvents (G. Liu et al., 2016b).

It is reported that solvents like water, alcohol NMP etc., can readily form radicals during the ultrasonication process. For example, in the case of water, hydroxyl radicals can be formed which can interact with the basal plane readily form covalent bonds with sp^2 carbon atoms, resulting in the transformation of that carbon to sp^3 hybridized carbon, with a slight out-of-plane puckering of that carbon atom. N-Methylpyrrolidone radicals have been studied as components in the exfoliation of MoS_2. NMP in an aerobic environment can act as oxidizing agent proposing an oxidation of graphene in the presence of free radicals from the singlet oxygen. On functionalization with hydroxyl groups h-BN is reported to become water soluble. The lower concentration of different 2D material sheets in various solvents might be justified by the possible addition of solvent radical to the basal planes and subsequently acting as a nucleation site for other solvent molecules. The dimension of such surface modifications are very small and becomes indistinguishable from the sheets stacking.

3.6. Synthesis of nanostructures of TMDs using LPE

MoS_2 nanomaterials with varying dimensions and preparation of MoS_2 nanorods have been reported earlier using hydrothermal methods (Ye Tian, He, & Zhu, 2004), chemical vapor deposition (CVD) (S. Han et al., 2015), two step electrochemical method (Gao & Zhang, 2014), (Nagaraju, Tharamani,

Chandrappa, & Livage, 2007), (Santillo, Deorsola, Bensaid, Russo, & Fino, 2012), (Wei et al., 2008), (Wiesel et al., 2009), (Pua, Chia, Zakari, & Liew, 2010), the sonication method (X. Zheng, Zhu, Yan, Bai, & Xie, 2004) and so on. Though, many different methods have been developed to synthesize MoS_2 nanorods, manipulating the morphology and the size of MoS_2 nanorods is still a challenge. Zheng *et al.* reported the synthesis of MoS_2 rods from microparticles using ultrasound cracking process (X. Zheng et al., 2004). Remskar (Remskar, Skraba, Cléton, Sanjinés, & Lévy, 1996) and his coworkers reported the first evidence of hollow crystalline MoS_2 micro tubes with several mm in length, several micrometers in diameter and less than 0.1 µm wall thickness. They have also reported the self-assembly of sub nanometer diameter single wall MoS_2 using catalyzed transport method with C_{60} as the growth promoter (Remskar et al., 2001). Formation of hollow MoS_2 tubules of uniform size and shape through a template were reported by Zelenski *et al.* (Zelenski & Dorhout, 1998) which were ~30 µm in length and 50 nm in diameter with a wall thickness of approximately 10 nm (Zelenski & Dorhout, 1998). Dorhout and his co-workers (Zelenski & Dorhout, 1998) reported the synthesis of MoS_2 fibers and tubules within the pores of porous aluminium oxide template by controlling the deposition of aluminium thiomolybdate precursor. MoS_2 nanorods were also successfully synthesized by redox reaction in aqueous media by Yumei Tian and his group in 2005 (Yumei Tian et al., 2005). All these methods involve tedious procedures and complex reactions which take place in a special environment. Recently, Han *et al.* (S. Han et al., 2015) have studied the evolution of the morphology of CVD grown MoS_2 nanorods with different growth conditions.

Nanostructures of 2D materials can be synthesized with the aid of high intensity ultrasound waves. The application of ultrasonic waves, in addition to the exfoliation of 2D materials, can curl and roll the sheets to produce desired nanostructure which makes then highly useful in material synthesis. For example, nanostructured MoS_2, was synthesized by the sonication of $Mo(CO)_6$ with elemental sulphur in 1,2,3,5-tetramethyl benzene under Argon atmosphere (Dhas & Suslick, 2005). This synthesis process changed the morphology to a spherical one, with average diameter 15 nm. It has also been observed that the

nanostructure thus prepared, displayed more defects and edges, making them an ideal candidate for catalysis related applications (H. Xu et al., 2013). Hollow MoS_2 nanoparticles has also been reported by the sacrificial etching of silica component which acts as a template for their growth (H. Xu et al., 2013). It has been studied that, ultrasonic irradiation of $Mo(CO)_6$, sulphur and silica nanoparticles in isodurene under Ar forms MoS_2-coated silica nanoparticles, subsequent replacement of Ar with air and removal of sulphur from the system yields MoO_3-coated silica nanoparticles. Etching of the silica component by HF leaves hollow MoS_2 or MoO_3. These hollow MoS2 nanoparticles showed better catalytic properties due to the obvious increase in surface area and edges. However, an easy and scalable procedure is required for the synthesis of MoS_2 rod/tube like-structures.

3.6.1 Influence of MW Heating

In contrast to the conventional heating methods, MW heating is advantageous in reducing the reaction time, increasing selectivity, yield etc. (Nüchter, Ondruschka, Bonrath, & Gum, 2004). Thus, MW aided heating has opened numerous applications in the completion of fast chemical reactions and rapid material synthesis (Komarneni, Roy, & Li, 1992) in very short duration, leading to a reduction in cost as well as energy saving. MW assisted approach has played an important role as a thermal tool to synthesize and to functionalize different classes of nanostructures of carbon, oxides, sulfides and hybrid materials by providing a fast route and a uniform distribution of energy which can be selectively administer towards the sample (Bregadiolli, Fernandes, & De Oliveira Graeff, 2017), (Kumar, Singh, Vaz, & Moshkalev, 2015), (Kumar, Singh, Singh, Savu, & Moshkalev, 2016), (Kumar, Singh, Savu, et al., 2016), (Vivas-Castro et al., 2011). MW aided synthesis of carbon nanostructures (Ikeda, Kamo, & Danno, 1995) and vertically aligned carbon nanotubes (Kharissova, 2004) have demonstrated the advantages of using MWs over the conventional heating mechanisms. A controlled exposure of MW irradiation can be very effective starting from exfoliating graphite to create bending or curling in the powdered samples.

Dipolar polarization and ionic conduction are the two main mechanisms involved in MW heating process. (Gabriel, Gabriel, Grant, Halstead, & Michael P Mingos, 1998), (Y.-J. Zhu & Chen, 2014). It can in general heat any material containing mobile charges such as polar molecules or conducting ions in the solvent or in a solid. The polar molecules try to orient in the rapidly changing alternating electric field of MWs, thereby increasing the heating effect by rotation, friction and collision of molecules. The conducting ions on the other hand will move through the solution depending on the orientation of the electric field, thereby causing local heating effect due to collision and friction (Y.-J. Zhu & Chen, 2014), (Collins, 2010). Many of the powdered samples like graphite, MoS_2 etc. efficiently absorb the MW radiation which then gets converted in to heat through energy dissipation via dielectic loss and conductive loss mechanisms through the coupling of the electric field corresponding to the radiation with the local electric dipoles associated with various structural defects, edge states, dangling bonds, impurities and others.

The properties of the solvents significantly affect the formation of inorganic nanostructures under MW heating treatment. Owing to the difference in solvent polarities, dielectric nature etc., different solvents interact differently with the MW. Hence, a suitable mixture of solvents with a proper volume ratio, can enhance the nanostructure formation with varying sizes and morphologies (Y.-J. Zhu & Chen, 2014), (Dallinger & Kappe, 2007). Alcohols are good solvents for MW heating, and their abilities to absorb microwaves are generally better than that of water. Alcohol and water are highly miscible and bond among themselves via hydrogen bonds. Hence, the mixed solvents of water and alcohols will certainly enhance the abilities to absorb microwaves as compared to that in the case of using water as the only solvent.

In our synthesis strategy, we have employed the cosolvancy technique of LPE using water and IPA mixture, followed by a MW heating treatment. Our results demonstrate that this facile synthesis process is a good route to produce MoS_2 nanostructures of rods, tubes, spheres and 2D sheets. The nanorods, nanotubes, nano spheres, thus, synthesized show narrow size distribution with

width/diameter in the range of 50-200 nm depending on the MW exposure time and exhibit high emission yield. By tuning the MW irradiation time, we show that metallic 1T phase can be induced in the original 2H matrix of MoS_2. The nanostructures produced after a MW irradiation of 10 min are mostly constituted of 2H phase, whereas, the synthesized MoS_2 sheets after 30 min MW exposure reveal a 1T-2H superlattice phase with a ratio of 1T to 2H concentrations as 70:30. This hybridized superlattice phase exhibits a very good structural stability upon exposure to high energy electron beam of 300 keV. In the next sections of this chapter we will discuss about the influence of electron beam on the 2D sheets and their interaction processes. The details of experimental parameters and conditions related to our synthesis process will be discussed in the following chapters.

3.7. Mechanism of electron beam interaction

In this section and sub sections we will in general discuss about the effect of electron beam on the layered materials like graphene, MoS_2 etc.. Our investigations reveal that while MoS_2 nanostructures mostly comprised of 2H phase are structurally vulnerable towards electron beams, however, the nanostructures of 1T-2H hybridized superlattice phase with a concentration of more 1T than 2H demonstrates good structural stability against high energy electron beam of 300 keV. As a result, it is essential to understand the electron beam related interactions on the 2D materials and the associated structural damage or stability of these thin and small structures.

Layered materials in their 2D forms in general undergo electron beam damage while characterizations using scanning electron microscope (SEM) and transmission electron microscope (TEM). These techniques, in addition to giving vital information about the material structure, imparts a temporary or permanent damage to the surface and in the bulk of the sample. The incoming electron beam can cause either elastic or inelastic collision within the sample, causing damage to the system. The elastic interaction is primary due to the deflection of incoming

electron beam due to the Coulomb field of the atomic nucleus, whereas, inelastic scattering occurs due to the Coulomb interaction between the incoming electron beam and the atomic electrons in the sample. A generalized schematic of the type of electron beam damages that can occur in a specimen is shown in Figure.3.3.

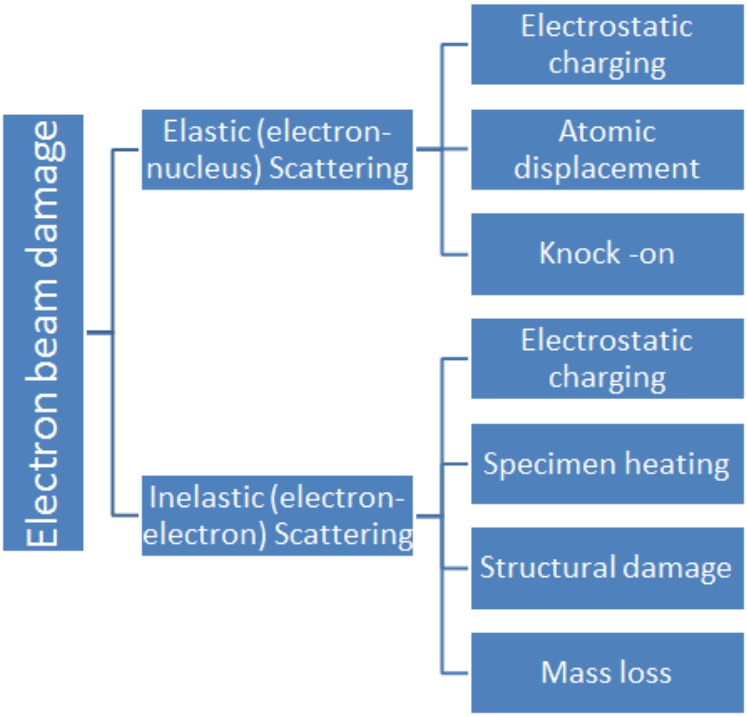

Figure.3.3. Schematic showing the various types of electron beam interaction with the sample.

The scattering events (both elastic and inelastic) lead to structural damage via displacement, sputtering, heating, charging, radiolysis, and radiation-induced contaminations. The structural damage in 2D materials via electron bombardment is commonly induced by three mechanisms: radiolysis, heating and knock on (Egerton, McLeod, Wang, & Malac, 2010), (Meyer et al., 2012). In the following subsections we will briefly discuss about these three main processes responsible for the structural damage of 2D materials by electron beam.

3.7.1.Radiolysis:

Radiolysis entails the electron beam damage via inelastic scattering mechanism. It is mainly the damage happening by the external radiation due to the

ionization of the edge atoms (Zan et al., 2013). Radiolysis involves bond breakage and is a crucial factor in insulators and some semiconductors. In the case of insulators, charging via electron bombardment is also a possible scenario, whereby, localized charges are formed on the surface which leads to electrostatic repulsion (Egerton, 2013).

3.7.2. Heating:

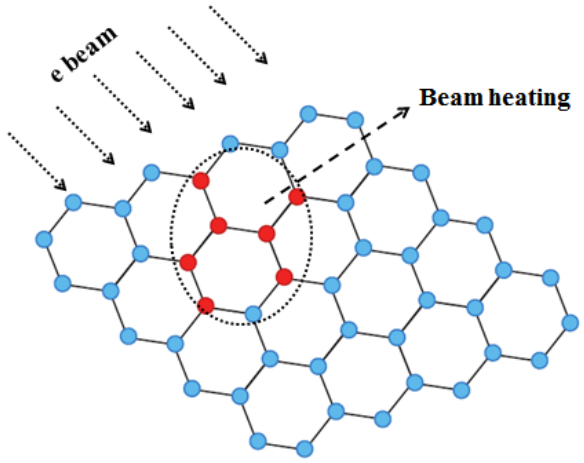

Figure.3.4. Schematic representation of electron beam heating process

The inelastic scattering involves, the direct collision between incoming electrons from the beam and the atomic electrons. A reasonable amount of energy is transferred during this process. This energy causes the heating up of the specimen, aiding to a local rise in temperature [Figure.3.4.]. The heat deposited in the sample directly depends on the electron beam current as well as on the energy transfer during each collision. Under any given condition, the rise in temperature has been observed to be independent of the thickness of the sample. (Egerton, Li, & Malac, 2004). Heating of samples can thus be a major issue in TEM measurements involving high beam current, which can even lead to the melting of thin samples. This issue becomes much grave for organic/polymer samples with lower thermal conductivity.

3.7.3. Knock-on

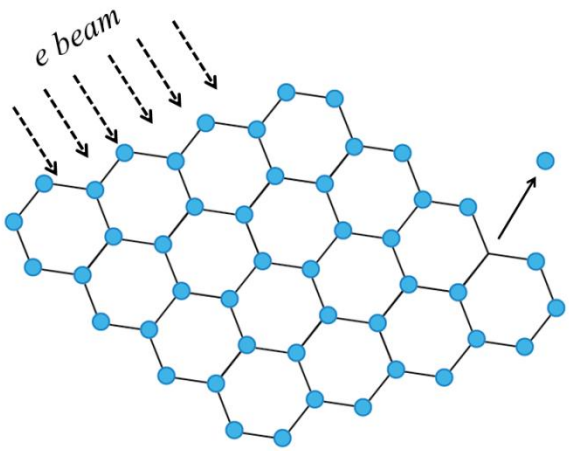

Figure 3.5. Schematic representation of knock-on process

The knock on mechanism becomes prevalent when the electron beam carries an energy sufficiently larger than the threshold value required to sputter away the atoms (Egerton, 2013). This method involves the bond breakage and thereby freeing an atom from the surface of the material. If a high elastic angle scattering occurs on a surface atom, a lower amount of energy would suffice to displace the atom. These atoms will be free to leave the sample surface, hence the term knock-on/sputtering[Figure.3.5]. The sputtering threshold is found to increase with increasing atomic number (Z) of the solid elements. Thus, low and medium Z atoms are more prone to the sputtering due to electron bombardment. The process of knock on is also directly influenced by the beam current.

3.8. Effects of electron irradiation

In 2D materials, the electron beam exposure can cause damage to the surface or edges where, the knock on threshold is minimum [109 review]. Even for a very low voltage, the energy transferred by the electron beam can be sufficient enough to generate structural deformations and atomic defects. The effects of electron beam interactions with the 2D materials are vivid in the form of

creating defects, structural transformation, nanostructures formation and so on. In the following subsections, we will discuss these effects of electron beam interactions in general with 2D materials.

3.8.1. Atomic defects:

In accordance with the laws of thermodynamics, 2D materials are always accompanied with intrinsic point defects (Banhart, Kotakoski, & Krasheninnikov, n.d.). Atomically resolved images using electron microscopy techniques aid to the identification of various point defects such as Stone Wales defect, single atom vacancy, di atom vacancy, etc. (Hashimoto, Suenaga, Gloter, Urita, & Iijima, 2004), (Meyer et al., 2008), (Suenaga et al., 2007), (Algara-Siller, Kurasch, Sedighi, Lehtinen, & Kaiser, 2013). However, the experimental tools themselves can be the cause of formation of these atomic defects. Under TEM investigations, graphene shows the formation of stable defects of varying sizes (Hashimoto et al., 2004), (Robertson & Warner, 2013), (Skowron, Lebedeva, Popov, & Bichoutskaia, 2015) which may relax to form stable structures (Hashimoto et al., 2004), (Skowron et al., 2015), (Warner et al., 2009). This property has been demonstrated in patterning the sheets of graphene and constructing nanoribbons out of it (Robertson & Warner, 2013), (Chuvilin, Meyer, Algara-Siller, & Kaiser, 2009). It is also reported that the electron interaction causes n doping in graphene, thereby decreasing electron conductivity in response to the formation of defects and damages (Feng et al., 2018).

In the case of MoS_2, 6 types of point defects have been identified which play a major role in tuning the properties of the material depending on the type of defects as well as their concentrations in the sample. Theoretical investigations using density functional theory (DFT) points out that the formation energy of point defects in monolayer MoS_2 depends highly on the chemical potential of sulphur (S). The lowest formation energy is reported for single S vacancy. Synthesis techniques play an important role in the formation of defect sites in the material where the growth environment can significantly influence the type of

point defect formed. This can be further enhanced and controlled by electron beam irradiation in order to modify the material property as required. Managing the formation and distribution of such defects using an electron beam with atomic precision can even cause a structural modification in MoS_2.

The electron beam irradiation of MoS_2 predominantly creates S vacancies due to its lower formation energy as has been verified by early experiments (Hansen et al., 2011), (Z. Liu et al., 2011). The displacement energy threshold of S atoms in MoS_2 is approximately 6.5 eV (H. P. Komsa et al., 2012), (X. Liu, Xu, Wu, Zhang, Yu, Qiu, Hong, & Jin, 2013). This value corresponds to the maximum knock on energy that can be provided by 80 keV electron beam (Zan, Bangert, Ramasse, & Novoselov, 2011). Thus, the optimum electron beam energy below which the MoS_2 sample is stable is found to be 80 keV and is experimentally verified by Garcia and his group in 2015 (A.Garcia, A M Raya, M M Mariscal,R Esparza, M.Herrera, S I Molina, G Scavello, P L Galindo, 2014). For a lower beam energy, say 60 keV, approximately 4.3 eV can be transferred to S atoms in which case, ionization mechanism is predominant (Krivanek et al., 2010), (W. Zhou, Zou, Najmaei, Liu, Shi, Kong, Lou, et al., 2013). However, no beam induced displacements are anticipated in this case.

Under continuous electron beam irradiation, these single atom vacancies can migrate and agglomerate to form various kind of defects (Sun, Banhart, & Warner, 2015) of different morphologies depending on the chemical compositions of the 2D sheets. These defects and distortions happening in the 2D crystals would govern in altering the material properties drastically e.g. inducing superconductivity charge density waves, magnetism etc. (W. Zhou, Zou, Najmaei, Liu, Shi, Kong, Lou, et al., 2013), (J. Lin, Pantelides, & Zhou, 2015), (Zhuhua Zhang, Zou, Crespi, & Yakobson, 2013), (Lehtinen et al., 2015). Thus, electron beam induced defect formation and controlling defect morphologies could provide new possibility to modify the functionalities of 2D materials.

3.8.2. Structural phase transformations:

It has been demonstrated that even structural phase transitions of 2D materials can be accomplished via controlled e-beam irradiation (X. Zhao et al., 2017). In graphene, a complete amorphisation is reported owing to exposure to a highly energetic electron beam (Kotakoski, Krasheninnikov, Kaiser, & Meyer, 2011). Electron beam induced change in structural polymorphic arrangement has been observed in MoS_2. Since, TMDs in general exists in semiconducting 2H and metallic 1T phases, interchange between these phases could be very important in realizing low resistance contacts for devices. In situ scanning transmission electron microscope (STEM) studies performed on single layer MoS_2 at high temperature showed that 2H and 1T polymorphs of MoS_2 can easily be converted from one to the other by a transversal displacement of one of the S planes via intralayer atomic plane gliding (Y.-C. Lin, Dumcenco, Huang, & Suenaga, 2014). 1T phase can also be intentionally introduced in the 2H matrix which is controllable in size by using a high dose ($0.7 - 1.8 \times 10^7$ e nm^{-2}) of incident electron beam during heating the single layer MoS_2 upto 400°C – 700°C in high vacuum (Y.-C. Lin et al., 2014). Thus, the phase transformation in exfoliated layers are not generally complete, but rather, forms hybridized layers with fractions of both 2H and 1T phase (Bertolazzi, Jacopo, & Andras, 2011).

The phase transition of 2H to 1T MoS_2 has been studied extensively both theoretically (Y. C. Liu, Wang, Xia, & Zhang, 2017), (Raffone, Ataca, Grossman, & Cicero, 2016), (Kumara & Ahluwalia, 2012), (Kan et al., 2014), (W. Zhao & Ding, 2017) and experimentally (Y.-C. Lin et al., 2014), (Eda, Fujita, et al., 2012), (Chou et al., 2015), (Guo et al., 2015). In addition to 1T metallic phase, a distorted 1T phase is also displayed by TMDs, which consists of zig-zag arrangements of metal atoms. Electron beam can alter the structure of these distorted phases of TMDs. In the case of MoS_2, it has been observed that the charge build up in TEM measurements causes to weaken the metal-chalcogen bond thereby reorienting the zig-zag metal atom bonds.

3.8.3. Formation of nanostructures:

Electron beam from STEM/TEM can be used to modify the material structure at the region of irradiation in a controlled fashion. A focussed sub-angstrom beam can interact with the targeted atoms thereby producing nanostructures with atomic accuracy. A large number of materials are viable to electron beam induced alteration into nanostructures with varying dimensionality. Zero dimensional nanoparticles, 1D nanowires/nanotubes etc. with well-defined morphology can be engineered with the aid of electron beam irradiation. The final morphology of the nanostructures mainly depend on the specimen properties and electron beam operation parameters like beam energy, acceleration, voltage, beam current etc. In rare cases, even interesting nanostructures with fractal geometries like nano-dendrites could be formed depending on the beam and material nature. Metastable structures can also be formed using focussed electron beam with definite energy, which in usual cases are unrealizable using conventional routes of synthesis.

The two main methods of formation of nanoparticles include electron beam induced fragmentation (EBIF) of the specimen and the localized beam induced nucleation/precipitation of crystalline nanoparticles within the 2D film. Beam induced heating and charging effects occur during EBIF process whereas on the other hand, nucleation/precipitation process are mostly non-thermal in nature as per previous reports (Pyrz, Park, Vogt, & Buttrey, 2007), (Caldwell et al., 2010). Charging effects can also contribute substantially in the fragmentation process (Gonzalez-Martinez et al., 2016).

Many materials on the other hand are susceptible to electron beam induced formation of crystalline domains which later evolve into nanoparticles. In most of the case, the specimen will be mostly amorphous, polymers or even layered materials. The nanoparticle formation involves two steps, chemical decomposition of the material followed by the atomic rearrangement in the chemically altered domain. The rearrangement involves atomic displacements facilitated by knock –

on mechanism or even charging effects (Gonzalez-Martinez et al., 2016), (Du, Takeguchi, Tanaka, & Furuya, 2003).

Linear atomic chains of the form M-X has also been observed experimentally in tri-atom monolayer of TMDs under high energy electron beam (X. Liu, Xu, Wu, Zhang, Yu, Qiu, Hong, Jin, et al., 2013), (J. Lin, Zhang, Zhou, & Pantelides, 2016). In MoS_2 several reports suggests the formation of metallic linear chains when investigated under TEM (J. Lin et al., 2014). These isolated MoS_2 metallic nanowires embedded in 2D semiconducting monolayer were also synthesized using STEM mode with accurate precision (J. Lin et al., 2016), (J. Lin et al., 2014). This atomic precision enables the formation of complex atomic chain metal-semiconductor junctions in 2D monolayers. The metallic nature of such linear atomic chains formed by e beam irradiation, suggests its candidature as metallic interconnects in 2D devices.

We demonstrate that by considering a MW assisted easy facile route of LPE, we are able to synthesize mixed MoS_2 nanostructures of sheets, spheres and rods/tubes and by changing simply the MW irradiation time keeping all other parameters same in the synthesis process, we can induce 1T phase in the original 2H matrix of MoS_2. We show that a 10 min MW treated sample exhibits mostly a 2H phase, whereas, a 30 min MW irradiated sample reveal a more of 1T phase than that of 2H. Our high resolution transmission electron microscopy (HRTEM) investigations show formation of coplanar 1T-2H hybridized superlattice phase comprised of around 70% of 1T and 30% of 2H. This hybridized superlattice phase manifests high structural stability towards electron beam of energy 200–300 keV. In the following chapters we will discuss the synthesis process of MoS_2 nanostructures, tuning of the structural phases which can correspondingly change the structural stability of these nanostructures.

3.9. Conclusion

In this chapter, we have briefly reviewed the liquid phase exfoliation technique utilized for the separation of few layer of TMDs from their bulk counterpart. Various factors affecting the stability of TMD dispersion formed in different solvents have been discussed. Few reported studies of exfoliation of TMDs in using solution based LPE are analysed and the benefits of cosolvent systems have been examined by literature survey. The method of nanostructure synthesis of MoS_2 by solution based techniques and the role of MWs in aiding the nanostructure formation have also been addressed. Then we have discussed about various methods by which an electron beam can interact with the 2D materials and the structural vulnerability of the 2D materials especially the 2D TMDs towards electron beam. This is followed by the various processes related to structural phase transitions in TMDs mainly 2H to 1T and the related structural stability towards electron beam which follows for 2D TMDs. All the literature surveys and the discussions put in this chapter are important to have an insight and understanding into the work on MoS_2 by providing a general layout carried out in this thesis.

CHAPTER 4

CHARACTERIZATION OF MoS_2 NANOSTRUCTURES- MORPHOLOGY, OPTICAL AND VIBRATIONAL PROPERTIES

This chapter deals with the synthesis of MoS_2 nanostructures using liquid phase exfoliation technique. We have proposed a simple method to synthesize MoS_2 nanostructures of spheres and rods/tubes by a simple modification of the traditional LPE where MW treatment (MW) at 175 °C for 10 min was used after the synthesis. The same MW assisted strategy is utilized to induce 1T domains in the original 2H lattice of MoS_2 by a small variation in the MW irradiation time. Exfoliated and MW treated MoS_2 nanosheets has been characterised using Scanning Electron Microscope (SEM), and the coexistence of 1T and 2H phases has been confirmed by optical characterization and Raman spectroscopy.

4.1. Introduction

Novel properties often emerge as the dimensionalities of materials are reduced. Extensive theoretical calculations and experiments performed on the nanotubes of carbon or TMDs reveal stability, mechanical property, exciting optical, electrical and electronic properties of these 3D cylindrical structures (Ghorbani-Asl et al., 2013), (Kuc, Zibouche, & Heine, 2011), (Kuemmeth, Ilani, Ralph, & McEuen, 2008), (T. Li & Galli, 2007), (Chico, Jaskólski, López-Sancho, & Muñoz, 2005), (W. Li, Zhang, Guo, & Zhang, 2014). To date, substantial efforts have been made to prepare MoS_2 nano/micromaterials with various morphologies such as inorganic fullerene-like structures and nanotubes (Tenne, Margulis, Genut, & Hodes, 1992), (Margulis, Salitra, Tenne, & Talianker, 1993), nanorods (Albiter, Huirache-Acuña, Paraguay-Delgado, Rico, & Alonso-Nuñez, 2006), nanowires and nanoribbons (Q. Li et al., 2005), amorphous nanospheres (Yumei Tian et al., 2006), nanoflowers (Fang, Bando, Gautam, Ye, & Golberg, 2008), nanoboxes (Bastide, Duphil, Borra, & Lévy-Clément, 2006) and hierarchical hollow cubic cages (Ye, Wu, Guo, & Xie, 2006). However, tailoring these nanomaterials to the desired morphology is a hard task. The ability to modify the morphology, size etc. is an important goal to achieve.

MoS_2 nanomaterials with varying dimensions and preparation of MoS_2 nanorods have been reported earlier using hydrothermal methods (Ye Tian et al., 2004), chemical vapor deposition (CVD) (S. Han et al., 2015), two step electrochemical method (Gao & Zhang, 2014), (Nagaraju et al., 2007), (Santillo et al., 2012), (Wei et al., 2008), (Wiesel et al., 2009), (Pua et al., 2010), the sonication method [46] and so on. Though, many different methods have been developed to synthesize MoS_2 nanorods, manipulating the morphology and the size of MoS_2 nanorods is still a challenge. MoS_2 nanorods were also successfully synthesized by redox reaction in aqueous media by Yumei Tian and his group in 2005 (Yumei Tian et al., 2005). All these methods involve tedious procedures and complex reactions which take place in a special environment. However, an easy and scalable procedure is required for the synthesis of MoS_2 rod/tube like-

structures. Out of the various methods for exfoliating 2D materials, LPE is the simplest. However, the solvents used are usually highly toxic and have a high boiling point which makes it difficult to remove. Later on, the cosolvency (K.-G. Zhou et al., 2011) method using water and alcohol was used for exfoliating TMDs by Udayabagya Halim and coworkers with water alcohol combination (Halim et al., 2013). It was observed that the exfoliation rate increased up to a particular solvent ratio and after that, the rate reduced. Here we apply this experimental method along with MW treatment to synthesize MoS_2 nanostructures, especially the rod/tube like-structures of MoS_2. MW assisted approach has played an important role as a thermal tool to synthesize and to functionalize different classes of nanostructures of carbon, oxides, sulfides and hybrid materials by providing a fast route and a uniform distribution of energy which can be selectively administered towards the sample (Bregadiolli et al., 2017), (Kumar et al., 2015), (Kumar, Singh, Singh, et al., 2016), (Kumar, Singh, Savu, et al., 2016), (Vivas-Castro et al., 2011). A controlled exposure of MW irradiation can be very effective starting from exfoliating graphite to create bending or curling in the powdered samples. Many of the powdered samples like graphite, MoS_2 etc. efficiently absorb the MW radiation which then gets converted in to heat through energy dissipation via dielectic loss and conductive loss mechanisms through the coupling of the electric field corresponding to the radiation with the local electric dipoles associated with various structural defects, edge states, dangling bonds, impurities and others.

In this work, we present an easy, facile and fast route to produce MoS_2 nanostructures by utilizing low cost easily available solvents without involving any rigorous or hazardous chemical reactions followed by MW irradiation at 175°C. The temperature of 175°C was chosen, taking into account a maximum yield of nanotubes as reported by Tian (Ye Tian et al., 2004) and his coworkers. LPE (Jawaid et al., 2016) is a simple, scalable technique, which can be controlled and calibrated easily to achieve desired nanostructures of MoS_2 and other 2D materials due to their potential applications in different field (Quinn, Ho, & Notley, 2013), (Winchester et al., 2014). To understand the effect of MW

irradiation, we considered of making samples, with 10 min (S1) and 30 min (S2) MW exposure respectively. Our investigations reveal that a MW irradiation time of 10 min mostly retains the 2H phase of MoS_2 (Z. Lin et al., 2016), whereas, a 30 min MW exposure induces 1T phase in the original 2H MoS_2 and makes 1T-2H hybridized superlattice with more of 1T than 2H (Reshmi, Akshaya, Satpati, Basu, & Bhattacharjee, 2018a). We attribute this structural transformation from 2H to 1T to the MW exposure where MW energy played a significant role in altering the crystal structure in the exfoliated sample.

4.2. Experimental Section

4.2.1. Materials

The initial precursor MoS_2 powder (<2 μm; 99% purity, 2H) was obtained from Sigma Aldrich and was used without further processing or purification.

4.2.2. Sample preparation

A mixture of 2 propanol and distilled water were used as a solvent combination for the exfoliation process of MoS_2 powder. The solvent ratio was optimized by repeated trials. In this method, we used distilled water to 2 propanol ratio 2:3 with an initial concentration of MoS_2 1 mg ml^{-1}. MoS_2 dispersion was made by ultra sonication for 60 min with consequent centrifugation at 7500 rpm for 10 min to separate bigger particles. The supernatant solution was collected and was further stirred at 600 rpm for 30 min followed by MW treatment at 175 °C for 10 min (S1). Another sample (S2) was prepared by slightly changing the synthesis conditions. Keeping all the initial parameters same, the MW treatment time was increased to 30 min.

4.2.3. Instrumentation

The MW irradiation of the exfoliated samples was done in an 'Anton Paar Monowave 300 Monowave EXTRA' microwave oven. The MW power was automatically adjusted according to the set temperature. The maximum power attained to reach a set temperature of 175 °C was 5-8 W. The pressure inside the chamber was 16 bar at 175 °C and remained almost constant for the whole duration of the MW treatment. The exfoliated MW treated sample was then characterised by scanning electron microscope (SEM) (Carl Zeiss EVO 18 Secondary Electron Microscope), transmission electron microscope (TEM) (JEM2100 and FEI-Tecnai S-twin) with an electron beam energy of 200–300 keV, UV–vis absorption (Cary 100 Bio UV–visible spectrophotometer) spectroscopy in the range of 200–800 nm, photoluminescence (PL) (Horiba Scientific Fluoromax 4 Spectrophotometer) spectroscopy in the spectral range of 200-800 nm and Raman (Renishaw inVia Raman microscope) spectroscopy measurements using a laser excitation of 532 nm.

Samples for SEM were prepared on silicon wafer. After the MW treatment, the solution was drop casted on Si substrate and was air dried for several hours (12-14 hours). Similar samples were used for Raman spectroscopy measurements as well. TEM investigations were carried out by dispersing exfoliated MoS_2 on carbon coated Cu microgrids. Optical measurements were taken on samples in solution phase taken in a quartz cuvette.

4.3. Results and Discussions

4.3.1. Morphology studies:

The SEM and TEM studies are carried out to investigate the morphology of the as synthesized samples before and after performing the MW treatment. Figure.4.1. shows, the SEM images of the formation of conglomerated MoS_2 sheets [Figure.4.1.(a)] and rod like-structures [Figure.4.1. (b)] with a non-uniform shape before MW application.

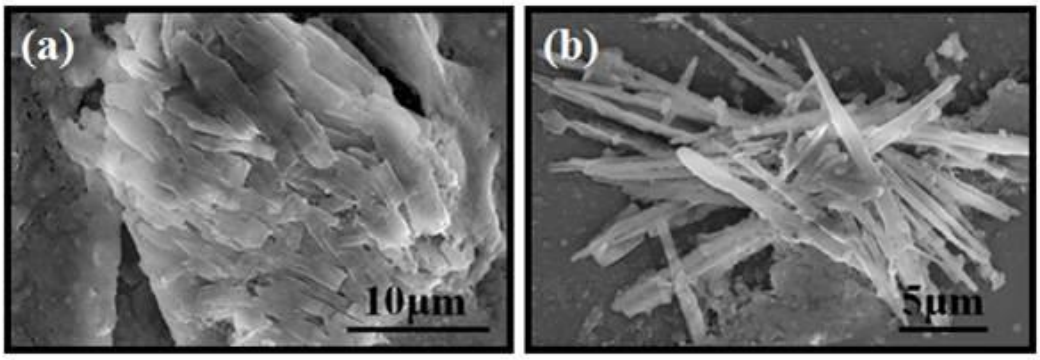

Figure 4.1. SEM images of MoS_2 dispersion before MW treatment; (a) and (b) show the images of conglomerated MoS_2 sheets (a) and rod like-features (b).

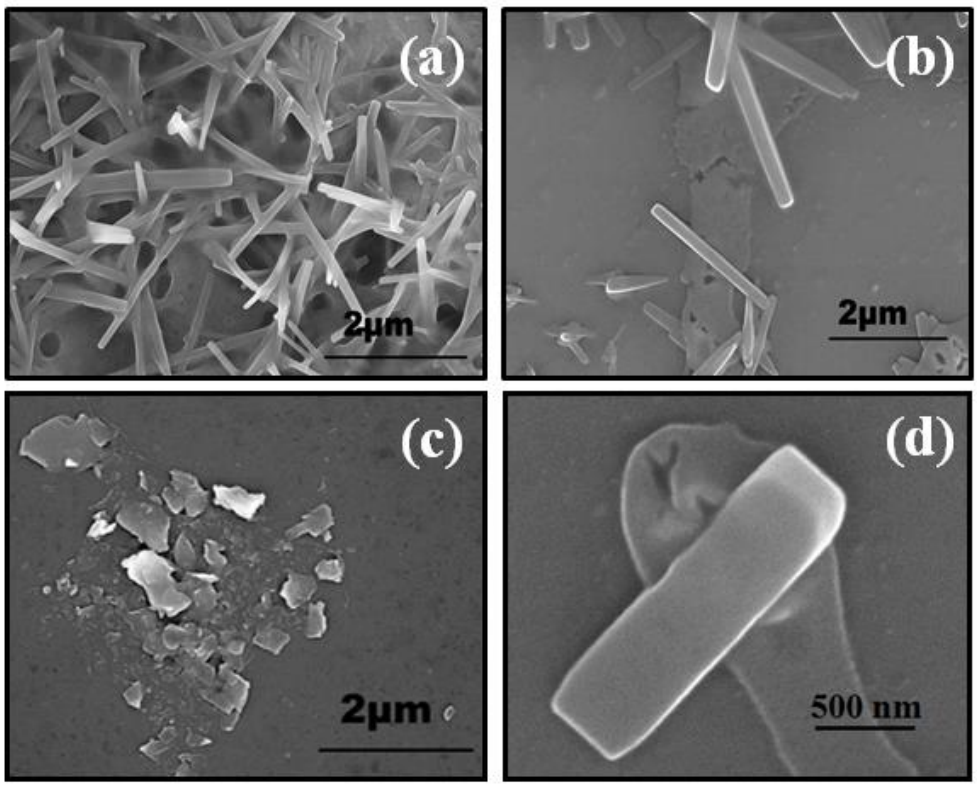

Figure 4.2. SEM investigations on 10 min MW treated sample (S1). Evidence of formation of (a, b) rod like-structures and (c, d) MoS_2 flakes.

Figures.4.2. shows SEM investigations carried out on a drop casted sample S1 which reveals the existence of rod like- structures and MoS_2 flakes in the exfoliated MW treated sample. The rods formed in this way have diameter in the

range of 150–200 nm and length several micrometers as can be seen in Figures 4.2(a) and (b). The flakes are of different size and shape and their dimension varies from few hundred nanometers to few micrometers [Figure.4.2(c) and (d)]. The authors in (Vattikuti et al., 2015) have reported the MoS_2 sphere like-structures with a diameter in the range of 50–100 nm and rod like-windings with a diameter in the range of 20–150 nm and a few tens of micrometers in length with a high degree of size homogeneity (Vattikuti et al., 2015) almost similar to our results. However, these authors have used the co-precipitation method to fabricate the nanoparticles like nanospheres and nanorods.

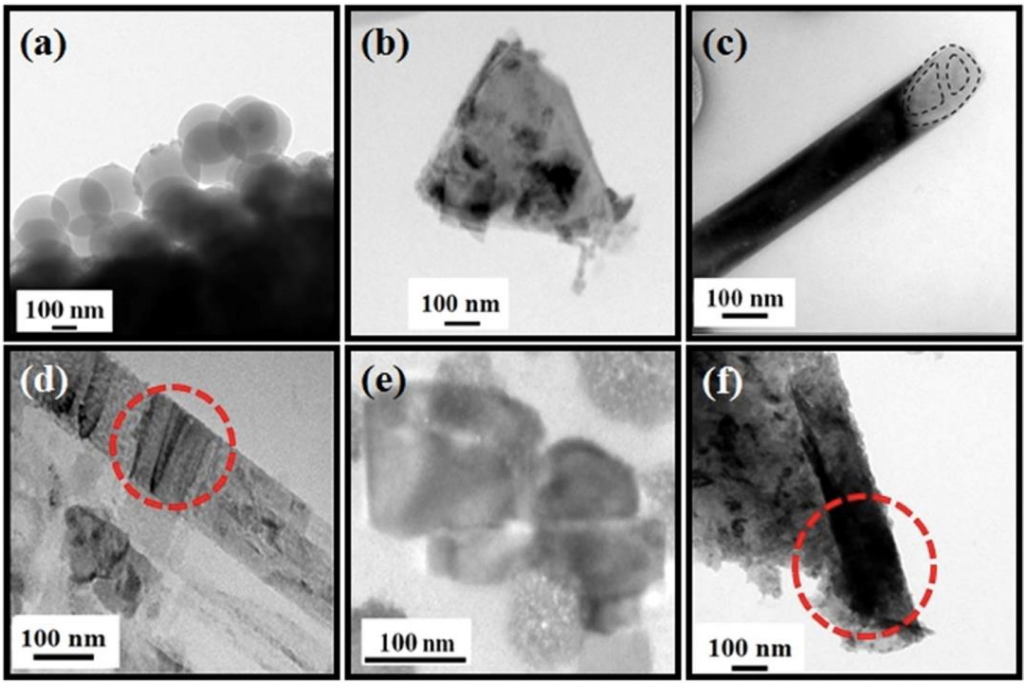

Figure 4.3. (a)–(c) Show the TEM images of spheres, flakes and rod features respectively in the exfoliated sample; (d) and (e) show the belt like-features where the MoS2 sheets curl and form the rod/tube structures; (f) shows the initiation of curling mechanism of a MoS2 sheet/flake. The curled region is marked in red circle.

Figure.4.3. displays the TEM investigations carried out on sample S1. Formation of mixed morphologies of MoS_2 nanostructures is again clearly evident in the TEM micrographs [Figures 4.3((a)–(c))] where spheres, flakes and rods co-exist in the sample. In figure 4.3.(a), MoS_2 spheres of almost uniform size are seen. The diameter of the spheres as well as the rods is estimated to be around

150–200 nm which is similar as was disclosed by SEM investigations (Figure.4.1 (b)). In Figure 4.3.(c), TEM micrograph of a hollow rod/tube structure is shown. The folding of the flake at the rod/tube end is marked with black dotted curves. The wall thickness of the rod/tube like-structure is around 15–20 nm which is determined from the separation between the inner and the outer black dotted lines [Figure.4.3.(c)]. Formation of belt like-structures can also be seen in Figure.4.3. (d) and (e) providing a direct evidence for the rolling and curving mechanism of the MoS_2 sheets to give rise to hollow MoS_2 rod/tube like-structures as was proposed by Vattikutty *et al.* (Vattikuti et al., 2015). The rolling mechanism of flakes is also evident from Figure.4.3.(f) (marked in red circle).

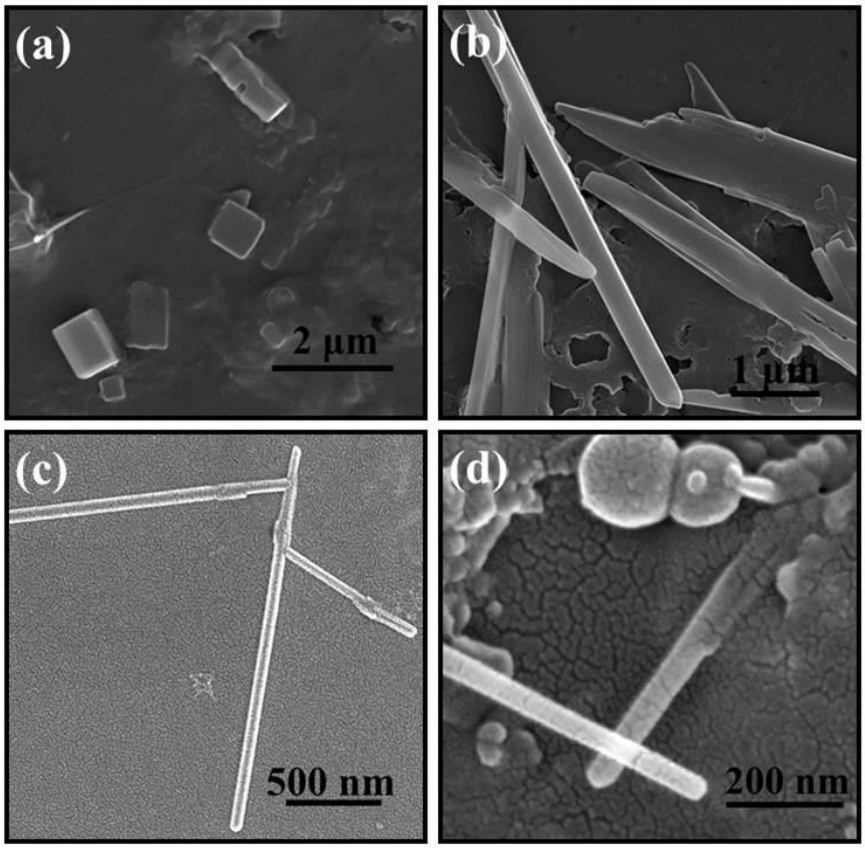

Figure 4.4. SEM micrographs from the 30 min MW treated MoS_2 sample (S2). Presence of (a) flakes, (b) sheets, (c) rod like- structures and (d) rods and spheres in the sample.

Figure 4.4. show the SEM studies carried out on drop casted sample S2. SEM investigations reveal a similar kind of morphology as was displayed by S1. We find the evidence of formation of MoS_2 flakes [Figure 4.4. (a)], sheets [Figure

4.4 (b)], rod like- structures [Figure 4.4 (c)] and rods and spheres [Figure.4.4 (d)] in the sample. The diameter of the rod like- structures and spheres for the sample S2 is in the range of 50-150 nm as revealed by SEM studies. The schematic of the exfoliation process is shown in Figure.4.5. The dangling bonds present at the edges of the MoS_2 flakes may initiate the curving mechanism to start forming the nanorods/nanotubes as suggested by Remskar *et al.* (Remskar et al., 2001). It was also proposed that the spheres elongate or conglomerate to form the rod like-structures (Vattikuti et al., 2015).

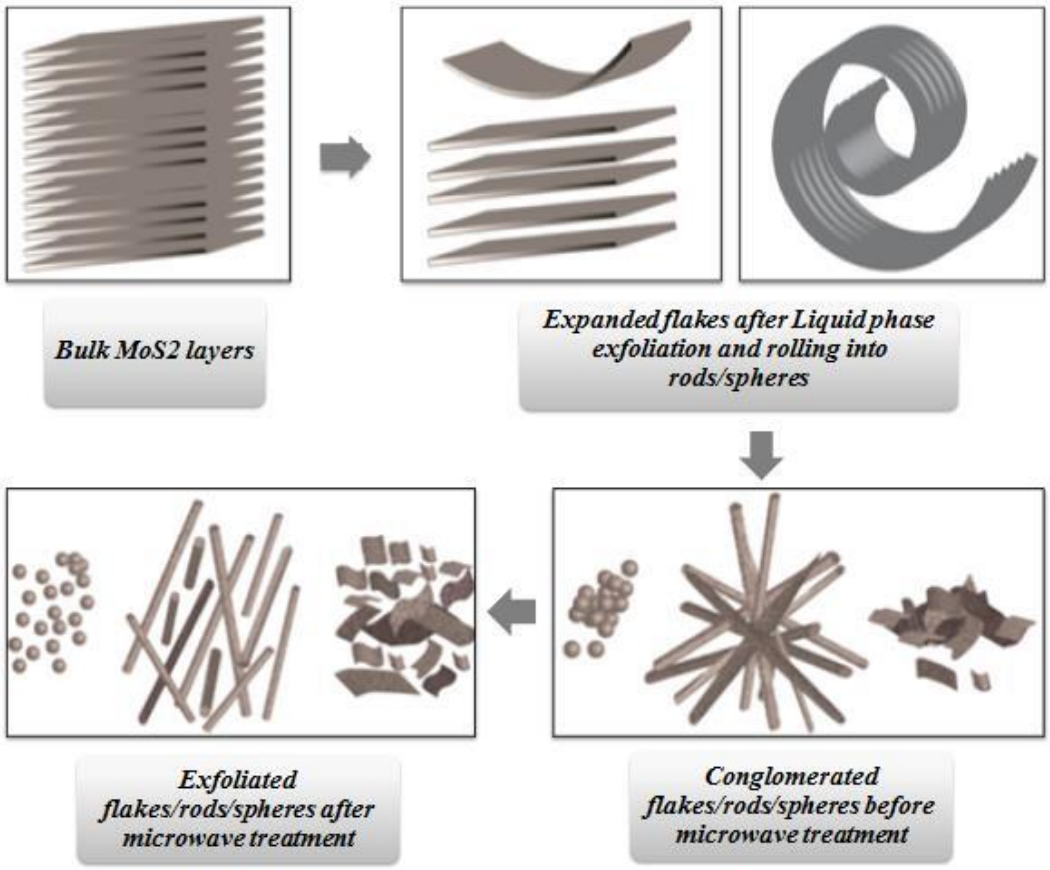

Figure.4.5. A schematic of the exfoliation process of bulk MoS_2 and the effect of MW treatment.

Evidence of amalgamated MoS_2 sheets and rod like structures with nonuniform shapes is a clear indication of the benefit of using MW irradiation in controlling the morphology of the exfoliated nanostructures. SEM and TEM studies carried out on the as synthesized MoS_2 nanostructures before and after

MW application demonstrate that the MW energy was useful in separating the MoS_2 sheets from the bundle and giving uniform shape to the morphology of the nanostructures. We see that after the MW treatment the exfoliated nanostructures exhibit a narrow size distribution with diameter in the range of 150-200 nm (S1) and 50-150 nm (S2) which otherwise seems not to be the case for the non-MW treated sample.

4.3.2. Optical characterizations

The optical properties of exfoliated MoS_2 sheets and nanostructures were investigated using UV–Vis absorption spectroscopy and photoluminescence spectroscopy. The absorption data in the wavelength range of 200–800 nm from the MW treated samples S1, S2 and the initial non – MW sample will be discussed here.

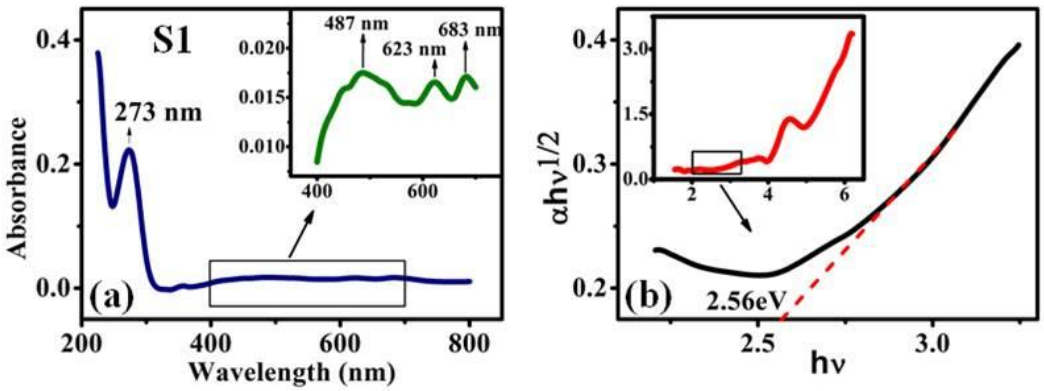

Figure 4.6. (a) UV–Vis absorption spectrum of MW treated sample. A prominent peak at 273 nm is seen in the spectrum which we associate with the high energy excitonic transitions corresponding to the 2H phase of MoS_2. Inset shows the enlarged region from 400–700 nm. Peak features at 487, 623 and 683 nm are shown as inset in (a); these peak features are assigned due to quantum confinement effects and the A, B excitonic transitions respectively; (b) Tauc plot derived from the absorption spectrum which shows a bandgap of 2.56 eV (484.5 nm). Inset shows the tauc plot for the whole range of energies revealing the presence of heterostructures in the exfoliated sample

The absorption spectrum from the exfoliated 10 min MW irradiated MoS_2 sample, S1, exhibit strong absorption in UV and visible region as shown in Figure.4.6. A first glance on the absorption data shows no peak like feature other than a high intense absorption at 273 nm [Figure.4.6.(a)]. However, to look for the characteristic A, B excitonic transitions in MoS_2, the spectral range of the same absorption data was enlarged from 400 to 700 nm where three additional less intense peak features at 487 nm, 623 nm and 683 nm are observed. These peaks are shown as an inset in Figure.4.6(a). In the absorption data, coexistence of mixed morphology of MoS_2 is clearly evident. We attribute the origin of the high intense 273 nm peak to high energy excitonic transitions corresponding to the 2H phase of MoS_2 (Eda, Yamaguchi, et al., 2012) nanosheets and nanostructures in the as-prepared exfoliated sample. Eda *et al.* (Eda, Yamaguchi, et al., 2012) have mentioned the occurrence of a similar peak in the near-UV range (200–300 nm) from colloidal suspension of highly monodisperse monolayer MoS_2 sheets which were prepared from MoS_2 powder through Li intercalation and exfoliation. They have ascribed this peak to high energy excitonic transitions of the 2H phase of MoS_2 (Eda, Yamaguchi, et al., 2012). Other authors (Nguyen, Sohn, Oh, Jang, & Kim, 2016) have reported a high intense absorption peak at 296 nm, the origin of which was associated to quantum confinement effects of MoS_2 nanodots. However, a larger dimension of the spheres and rod/tube structures in our sample with diameter in the range of 150–200 nm seems to be unlikely to show quantum confinement effects corresponding to a huge band gap of ~4.5 eV (273 nm). Radial confinement of electrons in the hollow nanostructures could be a possibility to give rise to quantum confinement effects. The weak peak features appearing at 623 nm and 683 nm in the absorption spectrum is assigned to the characteristic A and B excitonic transitions at the K point of the Brilllouin zone (Vattikuti et al., 2015), (Visic et al., 2011) of MoS_2. Due to spin orbit interaction and interlayer coupling the valance band maxima of MoS_2 spilts in to two (Visic et al., 2011). In the measured spectrum an energy difference of 0.17 eV (60 nm) between the A, B excitonic transitions (figure 4.6(a) inset) is in well agreement with the reported values (Visic et al., 2011), (Frey, Elani, Homyonfer, Feldman, & Tenne, 1998). The peak feature at 487 nm (2.546 eV) in the absorption spectrum

(Figure 4.6.(a) inset) can be assigned to the simultaneous existence of the optical absorption features coming from thinner MoS_2 sheets and the nanostructures (Mukherjee, Maiti, Midya, Das, & Ray, 2015a), (Le, Nguyen, Jang, & Kim, 2014) in the sample. The origin of this peak can be attributed to the quantum confinement effects arising from the mixed morphology of the exfoliated sample (Mukherjee et al., 2015a). Mukherjee *et al.* (Mukherjee et al., 2015a) have observed similar peak features in their chemically exfoliated MoS_2 sample in the range of 459–388 nm (2.7–3.2 eV) where 2D layers and nanocrystals coexisted. They have ascribed this peak feature due to increased optical bandgap of nanostructures w.r.t. their shrinking size. Visic *et al.* (Visic et al., 2011) have reported a similar peak feature around 540 nm (2.3 eV) in the absorption data of MoS_2 nanotubes. They have ascribed this feature which might be due to a direct transition between the states deep in the valence band to the conduction band at the M point of the Brillouin zone (Visic et al., 2011), (Coehoorn et al., 1987). Occurrence of the convoluted C, D excitonic peaks (Eda, Yamaguchi, et al., 2012) is also possible for the 2H phase of MoS_2 in the range of 400–500 nm. We ascribe the peak feature at 487 nm either due to the quantum confinement effects appearing from the heterodimensional morphologies of nanospheres and nanorods present in the as-prepared exfoliated MoS_2 or due to the C, D excitonic transitions responsible for the 2H phase of MoS_2 (Eda, Yamaguchi, et al., 2012). The absorption behaviour in the visible light region of MoS_2 nanospheres and nanorods with diameters almost in the similar range was explicitly shown by Vattikutty *et al.* (Vattikuti et al., 2015). The absorption features of the nanorods and nanospheres in their studies show similar behaviour, however, MoS_2 nanorods exhibit strong absorption than that of the nanosphere-like structures (Vattikuti et al., 2015). As a result, MoS_2 nanorods can have relatively high light-harvesting property due to the presence of more edge sites than in the nanospheres (Vattikuti et al., 2015). From the optical absorption data, we have calculated the optical band gap by using the Tauc equation near the band edge which is: $(\alpha h\nu)^{1/2} = A(h\nu - E_g)$; where α is the absorbance, $h\nu$ is the incident photon energy, A is a constant. The plot of $(\alpha h\nu)^{1/2}$ versus photon energy ($h\nu$) is shown in figure.4.6.(b). The band gap energy E_g is determined from the extrapolation of the linear fit onto the x axis

(Vattikuti et al., 2015), (Bhar, Mukherjee, Maji, Adhikary, & Mondal, 2010), (Diamandescu et al., 2008) and the calculated band gap in our case is determined to be 2.56 eV. This is in good agreement with the absorption peak appearing at 487 nm (2.546 eV) in the absorption spectrum. Several dips in the Tauc plot (inset figure.4.6.(b)) might be due to the presence of mixed morphologies (nanorods, nanospheres and MoS_2 nanosheets of variable dimensions) in the sample (M. Han et al., 2012), (Scafetta, Cordi, Rondinelli, & May, 2014). Emergence of the characteristic peak features in the absorption data corroborates the existence of mainly 2H phase of MoS_2 which comprises the nanosheets and the nanostructures.

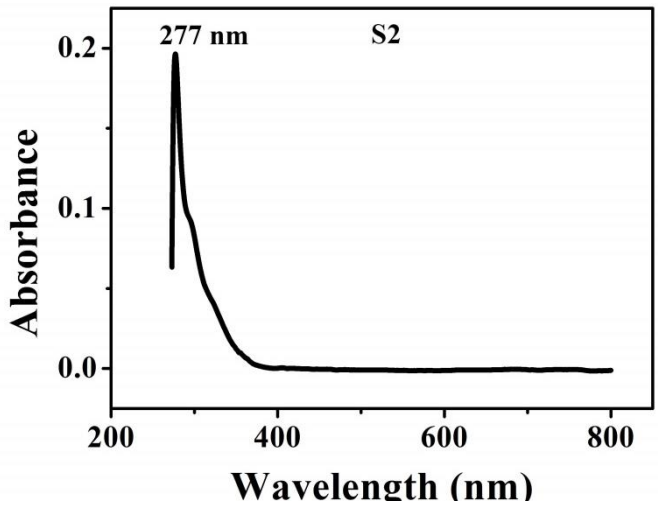

Figure.4.7. The featureless UV-Vis absorption spectrum obtained for S2

Absorption spectrum corresponding to 30 min MW irradiated sample, S2, is shown in Figure.4.7. A distinct difference can be clearly seen when one compares the absorption spectra [Figure.4.6.(a) and Figure.4.7] of the two samples, S1 and S2. We observe an almost featureless absorption from the 30 min MW irradiated sample, S2, for the whole data range except for the occurrence of a peak like-feature around 277 nm. We attribute the origin of the peak feature at 277 nm due to high energy excitonic transitions corresponding to the presence of 2H phase of MoS_2 (Santillo et al., 2012). We do not find any evidence of the other characteristic excitonic (A, B, C, D) transitions coming from the 2H phase in the absorption spectrum acquired from the MW irradiated sample. The appearance of

the peak feature at 277 nm with much low intensity compared to the peak at 265 nm from the non MW treated sample [Figure.4.8 shown below] and that from S1 along with the absence of no other peak feature throughout the absorption spectrum [Figure.4.7] signify a less concentration of 2H phase. Such a featureless absorption has been reported for 1T metallic phase of MoS_2 (Reshmi, Akshaya, Satpati, Basu, & Bhattacharjee, 2018b). The absorption spectroscopy studies carried out on sample S1 and S2 provide an initial insight where MW assisted structural evolution from semiconducting 2H to metallic 1T polymorphism seems to have taken place in the MoS_2 sheets and nanostructures. Sample S1, which is MW treated for 10 min seems to be mostly comprised of 2H semiconducting phase of MoS_2, whereas, the sample S2 appears to be primarily constituted of 1T metallic phase from the UV-Vis absorption spectroscopy spectra.

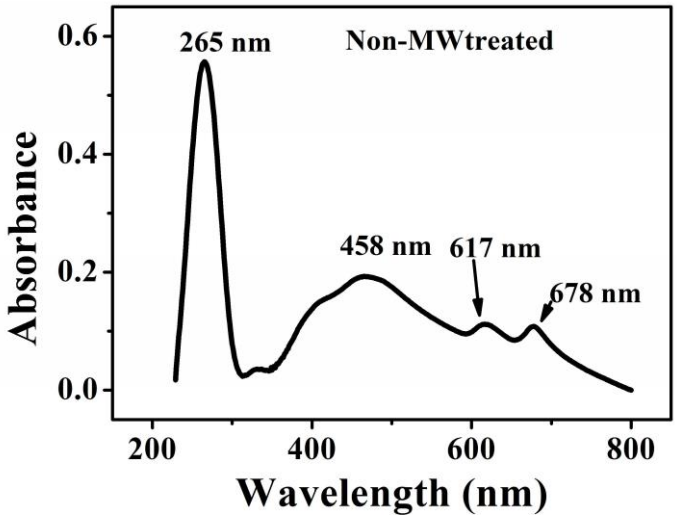

Figure.4.8. UV-Vis absorption spectrum for non-MW treated sample

Absorption from the exfoliated non-MW treated sample is shown in Figure.4.8 as a reference data. The absorption spectrum exhibits prominent peaks at 265, 458, 617 and 678 nm respectively as shown in Figure.4.8 which correspond to nearly virgin 2H phase of MoS_2. These peaks are red shifted in energy compared to the peaks exhibited by the 10 min MW treated sample S1 [Figure.4.6(a)]. A similar trend was observed by Visic *et al.*. (Visic et al., 2011)] in the absorption spectrum from the MoS_2 powder sample compared to the

exfoliated coaxial nanotubes. Frey *et al.* (Frey et al., 1998) have specifically shown that the positions of the characteristic peaks in the absorption data are highly dependent on the number (n) of atomic layers constituting the nanostructures rather than the particle size. For n > 6, a red shift in the exciton energies in the optical properties would show up which is due to the expansion of the c-axis of the MoS_2 layers. They have also shown a blue shift in energies w.r.t. increased annealing time from 3 min to 90 min for MoS_2 and WS_2 synthesized samples. In our case, a similar behaviour for the non-MW treated sample compared to the MW treated ones can be attributed to the facts, which are inherent to the topology of the nanostructures constituted with many shells (Reshmi et al., 2017b) as was explained by Frey *et al.* (Frey et al., 1998).

The direct excitonic transitions and the transitions occurring due to the quantum confinement effects owing to the heterodimensional nanostructures are clearly reflected in the photoluminescence (PL) spectra [Figure 4.9.] from the exfoliated MW treated MoS_2 sample, S1 and S2.

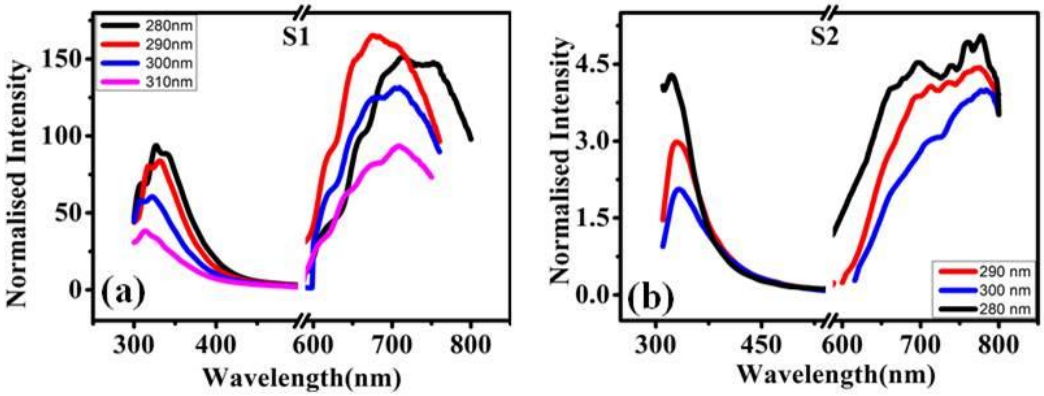

Figure.4.9. Photoluminescence spectrum obtained for different excitations from the exfoliated sample. Various small hump features (indicated by arrows) on the onset of the luminescence peak in the range 300–400 nm are assigned due to the confinement of photons in the hollow nanstructures. The high intense luminescence peak in the range 650–800 nm can be associated with the transitions in the nanostructures and due to the A, B exictons.

Normalized PL spectra of the as-prepared MW irradiated samples, S1 and S2, are shown in Figure.4.9. A clear difference in the intensities is observed in the emission spectra of samples S1 and S2. Both the samples exhibit two prominent emissions in the range of 300–400 nm and 600–800 nm for the excitations starting from 280 nm [Figure.4.9]. However, the emission intensity from S1 is much higher compared to sample S2 which can be clearly seen in the normalized emission spectra in Figure.4.9. This could be associated with the presence of more 2H semiconducting phase in S1 and a more of metallic 1T phase in S2. Presence of more 1T, being a metallic phase will hardly contribute in the luminescence spectrum. However, emission will still occur from the quantum confined nanostructures, defect states present in the sample S2. Our PL data shown here is consistent with the absorption results which also manifest a distinct difference in terms of more 2H phase in 10 min MW assisted sample, S1 and the presence of more 1T phase in the sample S2 which was MW irradiated for 30 min. The initial excitation wavelength of 280 nm is chosen keeping in mind the high intense absorption thresholds at 273 (S1) and 277 (S2) nm respectively. By varying the excitation wavelength from 280 nm to 310 nm for S1 and 300 nm for S2, the emission peaks show a systematic reduction in the intensity and a blue shift in energy [Figure.4.9] with the increase in the excitation wavelength. A comparatively broad set of emission features which are observed in the wavelength range of 600–800 nm with a relatively higher PL quantum yield in contrast to the emissions in the range of 300–400 nm could be associated with the transitions due to the nanostructures (Visic et al., 2011), characteristic excitons (Scheuschner et al., 2014) and the defect states mediated contributions (Tongay et al., 2013). The size distribution of heterodimensional nanostructures will give rise to distribution of energy gaps depending on the particle size which would lead to the broadened emission. Various defect states like single sulphur (S) and double S vacancies which are mainly formed in the sample during the exfoliation process itself can also contribute significantly in the emission spectrum (Saigal & Ghosh, 2016). This broad emission feature is also seen to be excitation dependent [Figure.4.9] with blue shift in energy as the excitation wavelength increases. A higher intensity of the luminescence peak observed for the 290 nm excitation from

sample S1 compared to the 280 nm in the emission range of 600–800 nm [Figure.4.9] might be associated with the fact that the surface states and the quantum dimensions both can contribute in a complicated way to the emission from the excited states of the nanostructures (Nguyen et al., 2016), (S. Zhu et al., 2013). As a result, a discrepancy in the emission intensity w.r.t. the excitation wavelength is a likely phenomenon sometimes. The excitation dependent photoluminescence is an indication of the formation of electron–hole pair at different energies in the heterodimensional MoS_2 nanostructures of the exfoliated samples. Radial confinement of electrons in the hollow nanostructures could also be a certain possibility in our case.

4.3.3. Vibrational Characterization

The vibrational properties of the samples were investigated using Raman spectroscopy measurements. Raman spectra for the bulk as well as for the exfoliated samples with and without MW treatment were recorded using a laser excitation of 532 nm.

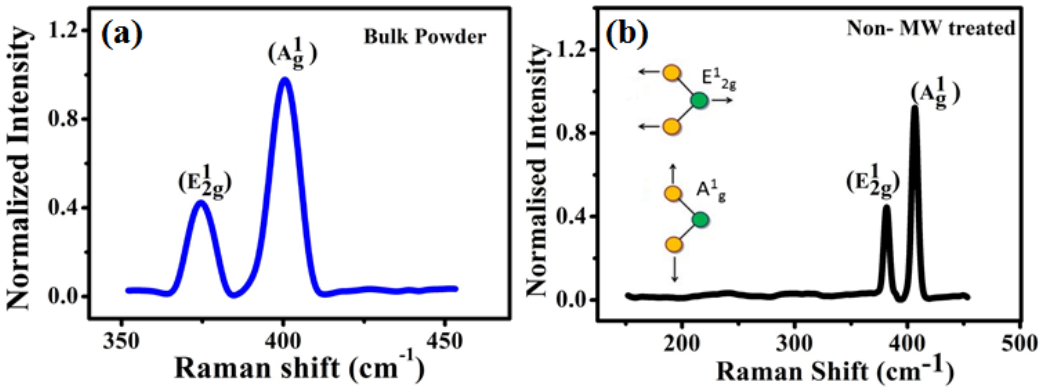

Figure.4.10. Raman spectra recorded for (a) as purchased MoS_2 powder, (b) Non MW treated sample. A schematic representation of the in- plane (E^1_{2g}) and out- of- plane (A^1_g) modes of vibration is given as inset to (b). Green and orange balls represent Mo and S atoms respectively.

Figure.4.10 represents the room-temperature Raman studies of bulk MoS_2 powder [Figure.4.10 (a)] and exfoliated non- MW treated MoS_2 sample [Figure .4.10 (b)]. For the bulk MoS_2 powder, Raman measurement was carried out from 350 to 450 cm^{-1}, whereas, for the non MW treated sample the Raman spectrum was obtained from 100 to 450 cm^{-1} in order to look for any extra feature in the spectrum which could be induced in the sample during the exfoliation process. From the bulk MoS_2 powder, characteristic Raman shifts are observed at 374.6 cm^{-1} (E^1_{2g}) and 400.89 cm^{-1} (A^1_g), whereas, for the exfoliated non- MW treated sample we observe the characteristic peaks at E^1_{2g} (382.17 cm^{-1}) and A^1_g (406.54 cm^{-1}). Both of these two bands in the Raman spectrum correspond to the optical phonon modes. The weak vdWs interlayer interactions would affect the intralayer bonding and the lattice vibrations of Mo and S atoms in the bulk stacked MoS_2 layers. The two Raman active modes of MoS_2 are schematically shown in Figures.4.10 (b) and (c). The in-plane (E^1_{2g}) mode corresponds to the two S atoms vibrating in the same direction and Mo atoms in the opposite direction (Figure. 4.10.(b)) whereas, in the out-of-plane (A^1_g) mode, the two S atoms vibrate in the opposite way out of the plane and Mo is stationary [Figure.4.10. (b) :inset] (H. Li et al., 2012), (C. Lee et al., 2010). A clear blue shift in the Raman peaks from bulk and exfoliated MoS_2 indicate the formation of nanostructures in the exfoliated sample (Nguyen et al., 2016), (Le et al., 2014), (H. Li et al., 2012). Theoretical calculations suggest that the frequency of both the characteristic modes should increase as one goes from 3D to 2D regime (Ataca, Topsakal, Aktürk, & Ciraci, 2011). We also observe a similar trend where both the Raman active modes appear at an increased frequency (blue shift) in the spectrum for the exfoliated sample compared to the bulk. The blue shift in Raman peaks are also reported for MoS_2 nanosheets and nanostructures (Nguyen et al., 2016), (Le et al., 2014), (H. Li et al., 2012).

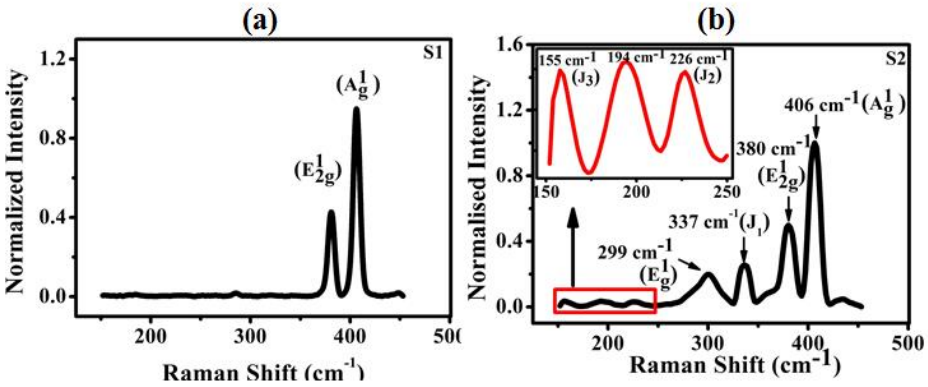

Figure.4.11. Raman measurements carried out on exfoliated MW treated samples; S1 (a) and S2 (b).

The Raman spectra acquired on exfoliated MW treated samples S1 and S2 are shown in Figure.4.11. The Raman spectrum [Figure.4.11(a)] of S1 shows similar peak features as of non-MW sample, however, with a small shift in the E^1_{2g} peak. The two characteristic shifts due to E^1_{2g} and A^1_g from the samples S1 and S2 are observed at 380 and 406 cm^{-1} respectively. We do not see evidence of any extra peak features from the sample S1. According to the symmetry considerations and a lattice-dynamical calculation, the strong 380 cm^{-1} Raman peak indicates a crystalline 2H MoS_2 (Jiménez Sandoval, Yang, Frindt, & Irwin, 1991). Theoretical calculations suggest that the frequency of both the characteristic modes should increase as one goes from 3D to 2D regime (Ataca et al., 2011). We also observe a similar trend where both the Raman active modes appear at an increased frequency (blue shift) in the spectrum for the exfoliated samples compared to the bulk. The blue shift in Raman peaks are also reported for MoS_2 nanosheets and nanostructures (Nguyen et al., 2016), (Le et al., 2014), (H. Li et al., 2012). It was observed that due to the absence of weak interlayer interaction as the dimension of the sample reduces from bulk to 2D monolayer MoS_2, the A^1_g mode softens whereas, the E^1_{2g} mode stiffens (C. Lee et al., 2010), (Molina-Sánchez & Wirtz, 2011). However, the Raman spectra acquired from the exfoliated samples, non MW treated [Figure.4.10(b)] as well as MW treated, S1 and S2 [Figure.4.11(a, b)] reveal that both the characteristic Raman modes have become stiff in our case. This phenomenon can be assigned to the presence of the

nanostructures in the exfoliated sample where the size has reduced in all three directions (Mukherjee, Maiti, Midya, Das, & Ray, 2015b). As a result, both in-plane and out-of-plane vibrations can become stiff (Mukherjee et al., 2015b). The difference between the E_{2g}^1 and the A_g^1 modes for the bulk and for the exfoliated samples S1 and S2 MoS_2 is found to be 26 cm^{-1}. This difference of 26 cm^{-1} between the two active Raman modes was reported earlier (Mukherjee et al., 2015b). On the contrary, the Raman spectra obtained from S2 [Figure.4.11(b)] shows five additional peaks other than E_{2g}^1 and A_g^1 modes. These additional modes of vibrations is displayed by the metallic 1T phase MoS_2. Raman shifts seen at 337 (J_1), 299 (E_g^1), 226 (J_2) and at 155 (J_3) cm^{-1} validate the formation of the 1T phase in the MW treated sample S2 [Figure.4.11(b)]. Presence of the E_g^1 band centering at 299 cm^{-1} along with the strong E_{2g}^1 band can be associated with the octahedral coordination of Mo in 1T-MoS_2 (Wei et al., 2008). Additional high intense Raman peaks at 380 cm^{-1} and 406 cm^{-1} which correspond to the in plane E_{2g}^1 and out-of-plane A_g^1 modes respectively can be associated with the presence of both 1T and 2H phase in the sample. Reports suggest that the distorted 1T phase (1T′) does not exhibit the E_{2g}^1 Raman shift (Wiesel et al., 2009). A prominent E_{2g}^1 onset in the Raman spectrum [Figure.4.11 (b)] at 380 cm^{-1} suggests hardly any presence of 1T′ phase in the sample. Characteristic Raman shifts in the spectrum shown in Figure.4.10 (b) strongly support the occurrence of the 1T polymorph in the exfoliated MW irradiated sample.

Thus, a featureless optical absorption spectrum [Figure.4.7] and the Raman spectrum [Figure.4.11(b)] clearly indicate the presence of a mixed 1T-2H phase in our exfoliated sample S2, whereas, sample S1 is mostly comprised of semiconducting 2H phase of MoS_2.

4.4. Conclusions

We have proposed a simple method to synthesize MoS_2 nanostructures of spheres, rods/tubes and sheets by a simple modification of the traditional LPE

technique where MW treatment at 175 ℃ for 10 min (S1) and 30 min (S2) was used for the synthesis of MoS_2 nanostructures. SEM and TEM investigations reveal explicitly the morphology of the as synthesized MoS_2 samples where the presence of heterodimensional structures of spheres, rod/tube and sheets coexist. Manifestation of hollow nanotubes with direct evidence of formation of belt like-structures in the TEM studies clearly suggest a rolling and curling mechanism of the MoS_2 sheets to give rise to these hollow nanostructures. From the TEM investigations, we find the wall thickness of the hollow rod/tube like-structures which is around 15–20 nm. The nanostructures, thus, formed are of diameters in the range of 150–200 nm for S1 and 50-150 nm for S2 respectively as revealed by SEM and TEM studies. Our optical and vibrational spectroscopy measurements suggest that the 2H phase of MoS_2 has mainly retained in S1, whereas, evidence of 1T phase formation is seen in S2. By a simple variation in the MW treatment time from 10 to 30 min, we see a clear indication of formation of metallic 1T phase in the sample. These results are directly validated by the UV-Vis absorption results where S1 shows signature of 2H, however, S2 reveals a featureless absorption corresponding to metallic 1T phase. Raman spectroscopy studies again directly corroborate evidence of 2H in S1, whereas, 1T and 2H in S2. Photoluminescence measurements provide an indirect signature where we find similar emission features, however, with a much less emission intensity from S2 compared to S1 supporting the formation of MW induced metallic 1T in S2. This chapter has dealt with the MW assisted LPE synthesis process of heterodimensional MoS_2 nanostructures and their detailed morphology, optical and vibrational spectroscopy studies.

CHAPTER 5

STRUCURAL STABILITY OF MoS_2 NANOSTRUCTURES

This chapter discusses the structural stability of exfoliated MoS_2 sheets comprised of hybridized superlattice phase of 1T- 2H MoS_2 under high energy electron beam of 300 keV energy.

5.1. Introduction

One of the most important features of MoS_2 is its polymorphism with distinct electronic properties. The main polytypes of MoS_2 are the semiconducting 2H phase and metallic 1T phase, which differs structurally in the arrangement of S atoms (Y.-C. Lin et al., 2014), (Mattheiss, 1973), (Fernando Wypych & Schöllhorn, 1992a), (Bissessur & Kannewurfb, 1993). 2H has a trigonal prismatic structure and belongs to the point group of D*3h* with band gap between the filled d_{z^2} and empty $d_{x^2-y^2,xy}$ bands whereas, 1T has an octahedral structure and belongs to the point group of O_h with Fermi level lying in the middle of degenerate $d_{xy,}, d_{yz}, d_{xz}$ single band (Mattheiss, 1973). Coplanar heterojunctions composed of vdWs layered materials with different structural polymorphs have drawn immense interest recently due to low contact resistance and high carrier injection rate owing to low Schottky barrier height. Present research has largely focused on efficient exfoliation of these layered materials and their restacking to achieve better performances. The Ohmic nature of heterojunction between semiconducting and metallic phases of MoS_2 was reported by Kappera *et al.* (Kappera et al., 2014). Thus, it can be a convenient solution to the contact issues in 2D electronics (Geim & Grigorieva, 2013). Moreover, the coexistence of 2H and 1T polymorphs can be of intense use in spintronics and electronic transport studies (Eda, Fujita, et al., 2012), (Hu et al., 2015a), (Sivaraman, Arthur, Souza, & Rodrigo, 2016), (Cai et al., 2015). The dynamic phase transitions from one phase to the other can find applications in the manufacture of non-volatile memory devices (A. Singh, Shirodkar, & Waghmare, 2015).

Due to external influence, deformations of many forms can occur in these 2D structures (H.-P. Komsa et al., 2012) as discussed already in the previous chapter. For example, the semiconducting 2H phase of MoS_2 is reported to be highly unstable to the electron beam (Reshmi et al., 2017b). An atomistic study of these materials involve probing by means of electron beam during investigations carried out by TEM, SEM etc. Hence, a clear understanding of the interaction of

the synthesized mixed phase with the electron beam is highly required to investigate the structural stability.

We have developed a MW assisted route to induce high concentration of metallic 1T phase in the original 2H matrix of exfoliated MoS_2 layers and thus facilitating the formation of a 1T-2H coplanar superlattice phase in a single nanostructure/flake. Thus, a MS homojunction of MoS_2 can easily be formed by simply increasing the MW irradiation time from 10 to 30 min. The coexistence of these phases has been experimentally verified using optical and vibrational characterisations discussed in the previous chapter. In this chapter we study the stability of the MW treated exfoliated MoS_2 samples, S1 and S2 during HRTEM measurements under high energy electron beam up to 300 keV. For S1 which is mainly comprised of 2H MoS_2, we observe an almost immediate interaction of electron beam with the nanostructures which fragment into small nanocrystallites within few seconds of starting the measurements. However, high structural stability is displayed by sample S2 which is constituted of MoS_2 1T-2H hybridized superlattice phase during HRTEM measurements under an electron beam of energy 300 keV. This structural stability could be either associated to the change in electronic configuration due to induction of the restacked hybridized phase with 1T- and 2H- regions or to the formation of the surface ripplocations (Eda, Fujita, et al., 2012), (Katsnelson & Geim, 2008). Surface ripplocations can act as an additional source of scattering centers to the electron beam and also it is possible that a pulse train of propagating ripplocations can sweep out the defects via interaction from specific areas of MoS_2 sheets (Katsnelson & Geim, 2008).

5.2. 2H to 1T phase transformation in MoS_2: Brief Overview

Extensive theoretical (W. Zhao & Ding, 2017) and experimental (Eda, Fujita, et al., 2012), (Chou et al., 2015) investigations have been carried out to study the nucleation of 1T phase in the 2H lattice of MoS_2. The mechanism of nucleation of 1T MoS_2 in the 2H phase, formation of coherent planar hetero-

structures of MoS_2 with 2H-1T interfaces and the kinetics of the interface propagation are studied by various authors (W. Zhao & Ding, 2017), (Hu et al., 2015b), (J. Ma et al., 2018), (Fei, Meng, Nie, & Luan, 2017). They confirmed that the boundary where metal atoms are coordinated in a zig-zag fashion are energetically stable and suggests the equilibrium 1T phase to be of hexagonal or triangular symmetry. Later in 2016, the phase conversion from 2H to 1T in bilayer MoS_2 was studied theoretically via lithiation (Pandey, Bothra, & Pati, 2016). Recent study has demonstrated the phase transition from 2H to 1T for MoS_2 and $MoSe_2$ using chemical vapors of butylamine and triethylamine which can be a suggested method for constructing passive chemical sensors (Friedman et al., 2017). A weak bombardment using Ar plasma could also be used for controlled phase transfer from 2H to 1T in monolayer MoS_2 (J. Zhu et al., 2017). Recently it was shown that even a mechanical strain can induce the phase transition in MoS_2 layers (Cheng, Sun, & Hu, 2016). The strain induced 2H to 1T transition in MoS_2 and its memristive behavior [21] has been addressed lately.

Reports on structural phase transformation of MoS_2 from 2H to 1T suggest that the transformation is not generally complete. Rather, we obtain layers with both phases co existing (Bertolazzi et al., 2011). Transformation of 2H to 1T MoS_2 by Li and K intercalation were reported earlier (Mattheiss, 1973), (Py & Haering, 1983) and later on electron crystallography and electron diffraction studies showed the presence of 1T phase of MoS_2 in the intercalated compounds (Heising & Kanatzidis, 1999), (F Wypych, Solenthaler, Prins, & Weber, 1999). During the alkali metal intercalation method, electron transfer from the alkali atoms of Li or K, causes a change in the d orbital configuration by electron donation to the MoS_2 layers, leading to an overall change in the exfoliated material which exhibits high yield of 1T MoS_2. The 1T metastable state persists until Li is completely removed subject to heating or aging (Eda, Fujita, et al., 2012), (Yang, Sandoval, Divigalpitiya, Irwin, & Frindt, 1991). The transformation from 2H to 1T is also found to be initiated by covalent functionalization (Voiry et al., 2014), (Qing Tang and De-en Jiang, 2015), (Mahler et al., 2014) or direct electron transfer (Y.-C. Lin et al., 2014), (Kang et al., 2014). Such a structural

phase transition from hexagonal, H to tetragonal, T can even occur by electron transfer from Au or Ag substrates (Loh & Chua, 2015). Re deposition was required to observe the phase transitions in MoS_2 which initiated as stripes near the Re dopant atoms and further extended to a large area. S vacancies produced also cluster together, producing local strain, which also causes the phase transition in MoS_2 (Y.-C. Lin et al., 2014). Recently, Xu *et al.*., has reported the synthesis of 70% 1T phase in the 2H matrix by a supercritical CO_2 based exfoliation technique (Qi et al., 2016). This technique has shown immense ability in synthesizing thinner MoS_2 sheets with more 1T component. In situ scanning transmission electron microscope (STEM) studies performed on single layer MoS_2 at high temperature showed that 2H and 1T polymorphs of MoS_2 can easily be converted from one to the other by a transversal displacement of one of the S planes via intralayer atomic plane gliding (Y.-C. Lin et al., 2014).

5.3. Stability of 1T-2H hybrid phase: Energetics

Naturally occurring MoS_2 is in the 2H semiconducting phase. Studies reveal that the distorted 1T (1T′) or the zigzag phase is energetically more stable than the 1T phase of MoS_2. The structural stability of T′ MoS_2 was first studied by Kan *et al.* (Kan et al., 2014) w.r.t. its formation energy which was shown to be higher than that of H-MoS_2 but lower than T-MoS_2 (Kan et al., 2014). The calculations performed based on energetics and kinetics of the phase transformation from 2H to 1T exhibit the formation energy of 1T and 1T′ MoS_2 as ∼0.84 and ∼0.55 eV per formula unit higher respectively than that of 2H (W. Zhao & Ding, 2017), (Kan et al., 2014) and the calculated barrier of phase transition from 2H to 1T is ∼1.6 eV per unit cell (W. Zhao & Ding, 2017). Scanning tunneling microscopy measurements (Qin, Yang, Frindt, & Irwin, 1992) and electron crystallography study (Heising & Kanatzidis, 1999) performed on restacked MoS_2 show that the distorted 1T′ MoS_2 is associated with Mo–Mo chains (Heising & Kanatzidis, 1999). According to density functional theory calculations the zigzag or the T′ MoS_2 is a charge density wave (CDW) state which is stable at low temperature (Kan et al., 2014). However, when it gains some energy from outside, CDW state becomes unstable and turns to octahedral

T-MoS_2 without the Mo–Mo chains (Kan et al., 2014). Theoretically, it has been shown that 2H to 1T phase transition is accompanied by the zigzag interface between 2H and 1T with a calculated barrier of zigzag boundary propagation of >4.0 eV (Raffone et al., 2016). As a result, expansion of 1T domain in the 2H lattice is a slow process.

Though enormous investigations have been carried out on atomic nucleation of the 1T phase in the 2H matrix, however, there is hardly any study so far related to the structural stability of the hybridized 1T-2H superlattice phase of MoS_2 according to our knowledge. By first principle theoretical calculations, it was observed that the thermodynamic stability of the hybrid 1T-2H phase is more, almost comparable to that of the semiconducting 2H phase (Jiang et al., 2015). Upon hybridization, the overall increase in the system energy compared to 2H phase was shown to be as small as 0.03 eV, whereas, the formation energy of the 1T phase is around 0.28 eV higher than that of 2H. Therefore, an increase in energy of 0.03 eV upon formation of the hybridized 1T-2H phase w.r.t. 2H is only about 10% of the energy difference between the 2H and the 1T (Jiang et al., 2015). As a result, stability of the 1T-2H hybridized phase is very close to that of 2H and much higher than that of pure 1T (Jiang et al., 2015). The metallic nature of the hybridized state was asserted from the fact that the total density of states of Mo *d* orbitals couple with that of the S_p orbitals and cross the Fermi level showing high conductivity (Jiang et al., 2015).

5.4. Experimental Section

Samples S1 and S2 were prepared as discussed in section 4.2.2. Exfoliated samples were then characterized by TEM (JEM2100 and FEI-Tecnai S-twin) with an electron beam energy of 200–300 keV.

5.5. Results and discussion

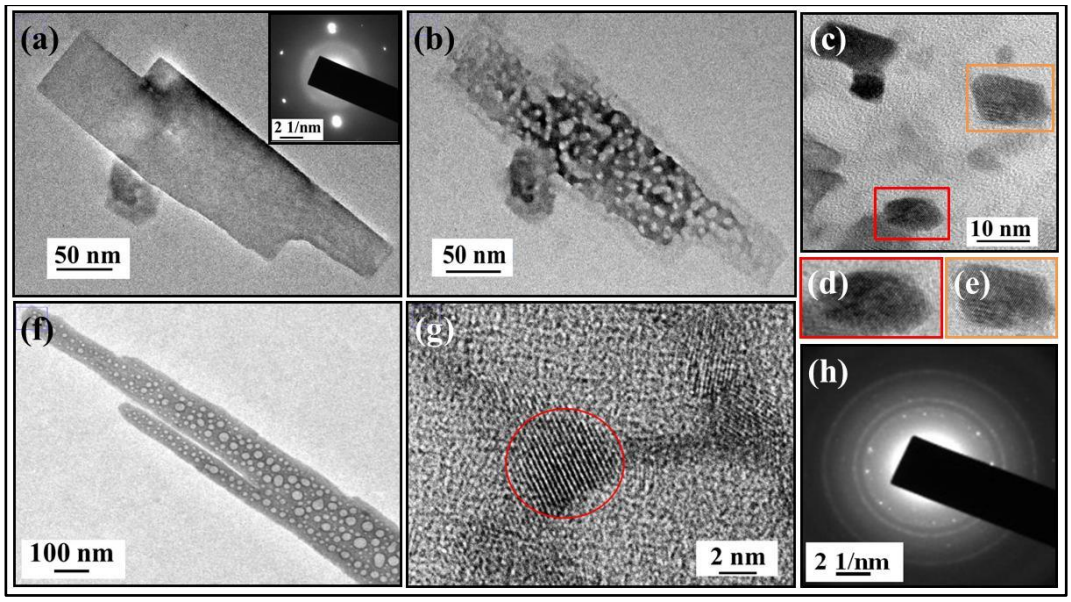

Figure 5.1. (a) and (b) Show the consecutive TEM images taken on a flake just after exposing and after 10 s of electron beam interaction. Beam energy in this case was 300 keV. Inset of (a) shows the hexagonal symmetry of the sample just after exposing to the electron beam. (c) Shows the formation of nanocrystallites upon beam interaction after 1 min (d), (e) TEM images of two nanocrystallites which are marked in (c). (f) Depicts the interaction of a 200 keV electron beam with S1 and the formation of porous structures just after an electron beam exposure for 10 s. (g) High resolution TEM image showing the formation of nanocrystallites from the nanorods almost after 1 min of electron beam exposure. (h) The SAED pattern taken after the beam interaction which shows the polycrystalline/amorphous nature of the sample.

Figure.5.1 shows the set of consecutive TEM studies carried on S1 nanosheets and nanorods in a span of 1 min. Illustration of the electron beam induced damage is mapped [Figure.5.1] for MoS_2 flake [Figure.5.1(a)] and nanorods [Figure.5.1(f)] which was evident almost immediately after starting the TEM measurements. We find that within approximately 10 s of electron beam exposure MoS_2 flakes and rod like- features start forming pores [Figures.5.1(b), (f)] along the surface and eventually decompose in to nanocrystallites [Figure. 5.1(c), (g)]. The corresponding Selected Area Electron diffraction (SAED)

patterns taken on the sample when it is just exposed to the electron beam [inset, Figure.5.1(a)] and after 1 min of electron beam exposure are shown in Figure.5.1(h). The diffraction pattern corresponding to the as prepared sample shows a clear 2H phase with hexagonal symmetry [inset, Figure.5.1(a)]. However, the hexagonal phase is lost upon electron beam interaction and the corresponding diffraction pattern exhibits concentric rings with spots which are related to either polycrystalline or amorphous phase in the sample.

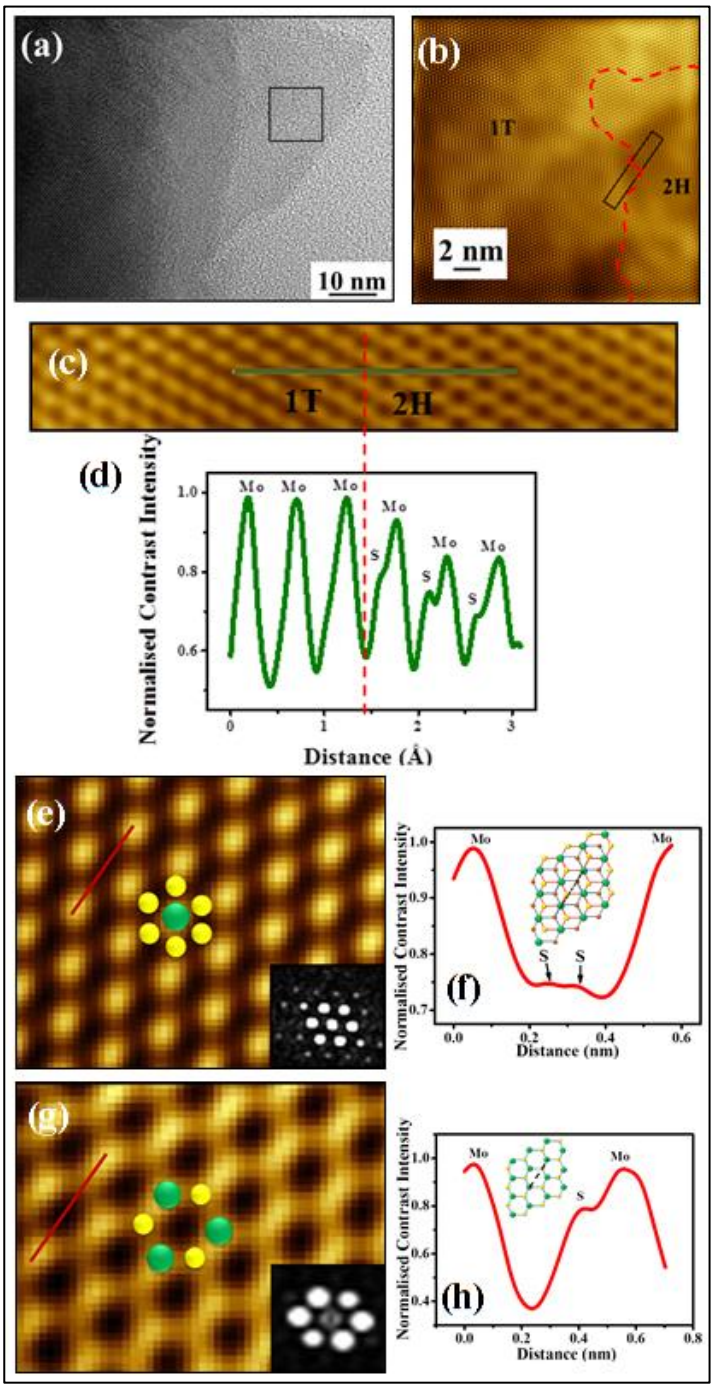

Figure 5.2. (a) MoS_2 flakes of different heights giving different contrast in the image. (b) HRTEM image taken from small square region marked in (a). The existence of both 1T and 2H phases are evident in the image and the phase boundaries are marked with red dotted line. (c) A region consisting both 1T- and 2H-domains which is taken from the marked rectangular area in (b)(shown as yellow dotted arrow). (d) The contrast profile taken along the green line as shown in (c). (e) HRTEM micrograph of 1T with corresponding FFT as inset. (f) The contrast profile taken along the red line as marked in (e) with schematic of the 1T as inset for better understanding. (g), (h) Similar HRTEM

image, FFT (inset) shown in (g) and contrast profile, schematic (inset) shown in (h) respectively from the 2H domain. In the profiles (f), (h), one can clearly see a significantly lower contrast of the S atoms from 1T compared to a stronger onsets of the S atoms from 2H corroborating the variation in the S atom stacking corresponding to the two domains. In all the schematics (e)–(h), green and yellow balls correspond to Mo and S atoms respectively. The color code shown in the HRTEM images was chosen by the post analysis software.

High resolution TEM (HRTEM) investigations carried out with an electron beam energy of 300 keV from S2 sample is shown in Figure.5.2. MoS_2 flakes constituted of different layers are visible in the TEM micrograph [Figure. 5.2(a)]. The flake terminations are having clear steps with different heights corresponding to different contrast in the image [Figure.5.2(a)]. An atomically resolved image of the surface taken from the marked area in Figure.5.2(a) is shown in Figure.5.2(b). HRTEM micrograph shown in Figure.5.2(b) clearly reveals formation of heterogeneous atomic arrangement in S2.

Occurence of a mixed 1T-2H phase with domains of octahedral 1T and trigonal prismatic 2H in the basal plane within the same MoS_2 sheet is evident Figure.5.2[(b), (c), (e), (g)]. A region containing 2H domain is marked with a red dashed line in Figure.5.2(b). In 2H-MoS_2, the coordination of S and Mo atoms forms a trigonal prismatic configuration with S atoms in the upper plane situating directly above the S atoms in the lower plane, whereas, in 1T-MoS_2, S atoms in one of the planes are displaced from their ideal position in the ⟨2100⟩ direction by $a/\sqrt{3}$ compared to S atoms in the adjacent planes and the Mo atoms occupy the octahedral holes of the S layers. Both 2H and 1T form hexagonally packed Mo lattice sandwiched between two hexagonal S lattices within an individual layer of MoS_2 and exhibit symmetrical Mo–Mo spacing. An enlarged atomically resolved image taken from the marked rectangular area in Figure.5.2(b) is shown in figure 5.2(c). Our HRTEM investigations reveal an atomically sharp interface between the 2H and the 1T domains [Figure.5.2(c)]. Evidence of an atomically sharp interface is further reflected in the contrast profile [Figure.5.2(d)] taken along the line shown in Figure.5.2(c) across the boundary, covering areas from both 1T and

2H phases. As the atomic coordination of the two polytypes (Eda, Fujita, et al., 2012) are different, a stronger onset from the S atoms in the 2H region (marked as arrows in the profile, Figure.5.2(d)) can be clearly seen, whereas, an abrupt decrease in the contrast of the S atoms corresponding to 1T domain is observed along the profile. Figure. 5.2(e), (g) very well exhibit the 1T and 2H structures and the contrast profiles [Figure.5.2(f), (h)] taken along the lines marked in Figure.5.2(e), (g) further corroborate the presence of heterogeneous atomic phases.

Schematics of the atomic arrangements corresponding to 2H and 1T are shown as insets in Figures.5.2(f), (h). The profiles taken along two Mo atoms are marked as black dotted lines in the schematics for a better understanding. A clear difference of the signal contrast in the profiles [Figures.5.2(f), (h)] is certainly evident from the S atoms corresponding to 2H- and 1T- phases of MoS_2 (Eda, Fujita, et al., 2012). Nearly identical Fourier transformed images [insets, Figures.5.2(e), (g)] of 2H and 1T and an equal Mo–Mo spacing of 3.05±0.05 Å for both the phases indicate an almost strain free, undisturbed orientation of Mo atoms with hexagonal arrangement across the two domains. According to our analysis of the HRTEM micrographs covering around a total of 3000 nm^2 area, we find 1T and 2H concentrations approximately 70% and 30% respectively. Here it should be noted that our HRTEM studies and post data analyses reveal similar behavior of 1T and 2H domains of MoS_2 which were earlier reported only by STEM investigations (Eda, Fujita, et al., 2012), (Chou et al., 2015). Though, in HRTEM studies, intensity is not proportional to the atomic contrast, however, we show here that even the contrast studies can provide good insight to understand some results. The profiles shown in Figures.5.2 [(d), (f), (h)] clearly exhibit different stacking of S atoms with distinct contrast variation corresponding to 1T and 2H which is similar as the intensity profiles discussed earlier by various authors (Eda, Fujita, et al., 2012), (Chou et al., 2015) in the context of STEM measurements. HRTEM image shown in Figure.5.2(b) also reveals formation of wrinkles/ripplocations on the MoS_2 sheets. Across the ripplocations perfect crystalline structure of the MoS_2 is evident without exhibiting any broken bonds

or dislocations (Kushima, Qian, Zhao, Zhang, & Li, 2015). From the contrast in the TEM micrograph [Figure.5.2(b)], the width of these ripplocations is estimated to be around 3±1 nm.

The presence of ripplocations are observed in many 2D system, either in the buried form, or on the surface (Kushima et al., 2015), (Gruber et al., 2016), (Fasolino, Los, & Katsnelson, 2007). The localized nature of these foldings, called ripplocations has been theoretically investigated using density functional approach. The studies suggest that the small ripplocations over long range can merge to form larger immobile folds which further alters the electronic nature of the sample (Sun et al., 2015).

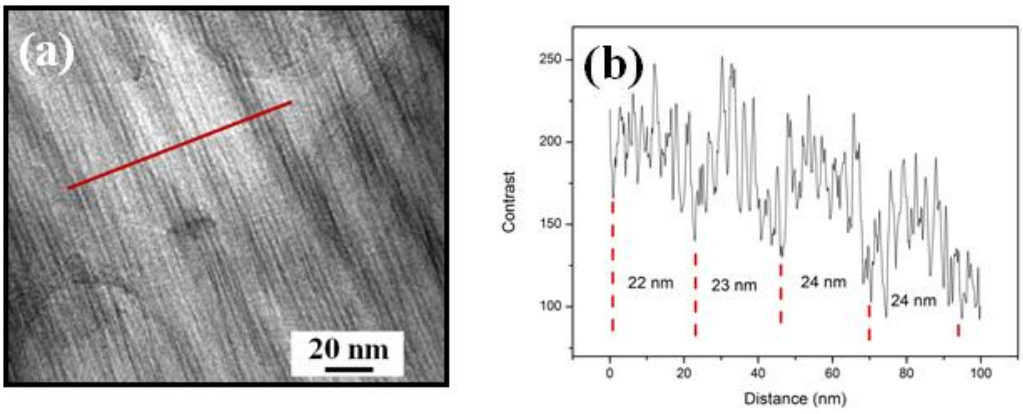

Figure 5.3. (a) Ripples with larger sizes. (b) line profile taken along the red line in (a). The superposition of smaller ripples on top of a larger ripple is evident from the line profile. The lateral dimension of ripples are around 20 nm.

Apart from small surface ripplocations/wrinkles as shown in Figure.5.2(b), even ripples with larger sizes were also observed on the exfoliated flakes in our sample S2 [Figure.5.3]. The average lateral periodicity or width of such bigger ripples were estimated to be of the order of 20-25 nm. We also observed smaller perturbations in the form of small ripples with lateral width approximately 3±1 nm within the surface of bigger ripples. The presence of these ripples or ripplocations on the exfoliated MoS_2 sheets could be due to either (i) strain induced by the formation of 1T-2H superlattice phase within the original 2H

matrix in the same MoS_2 sheets; or (ii) thermal effect assisted by MW irradiation or (iii) during the preparation of the TEM samples.

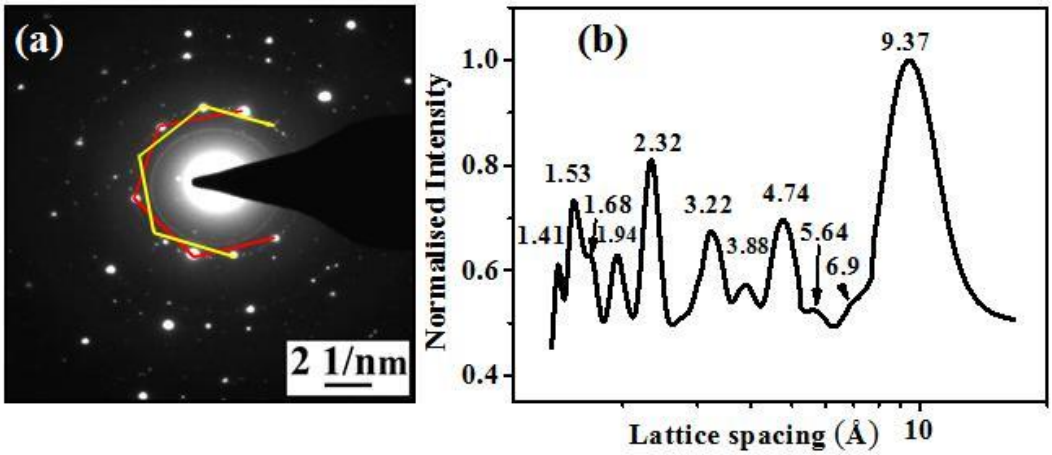

Figure 5.4. (a) Electron diffraction pattern obtained from S2 sample. The presence of 1T/2H heterostructure is clearly evident from the additional diffraction spots at 30° angle between the hexagonal spots of 2H phase. The rotated hexagonal planes are marked in (a). (b) The radial profile corresponding to the diffraction spots in (a) shows peaks from both 1T and 2H phases. An increased lattice pacing is observed in the (002) direction which could be due to interlayer expansion during restacking of layers.

The electron diffraction pattern (EDP) taken from a selected area on sample S2 is shown in Figure.5.4(a). Good crystalline nature of the exfoliated MoS_2 sheets can be observed in the selected area electron diffraction (SAED) pattern with clear and distinct spots depicting the 1T-2H symmetry [Figure.5.4(a)] of MoS_2. The EDP corresponding to 2H-polytype shows a hexagonal arrangement of diffraction spots [Figure.5.4(a)], whereas, that of 1T-polytype shows [Figure.5.4(a)] extra spots at 30° angular spacing in between the hexagonal spots of the 2H phase due to 30° off-set of the S atoms corresponding to upper and lower layers [46]. Here, it should be noted that absorption, PL and Raman studies carried out just after MW irradiation and before conducting the TEM measurements corroborate the fact that the induced 1T domains in the 2H matrix is not due to the electron beam irradiation during the TEM investigations but rather a MW assisted transition from 2H to 1T.

In Figure.5.4(b), we report radial intensity profile obtained by integrating the intensity of the diffraction pattern [Figure.5.4(a)] along the azimuthal direction (Rotunno et al., 2016). The intensity mapping of the diffraction pattern provides good insight into the characteristic crystalline planes corresponding to 1T and 2H polymorphs present in the exfoliated MW treated MoS_2. From the radial profile plotted in Figure.5.4(b), strong evidence of the occurrence of a mixed 1T-2H heterogeneous phase could be further validated. The peak feature at 1.41 Å is assigned to the (220) reflection coming from 1T and/or (200) reflection from 2H-MoS_2 (Fernando Wypych & Schöllhorn, 1992b) ,(Downs & Hall-Wallace, 2003). The onset at 1.53 Å is attributed to (004) reflection from 1T (Fernando Wypych & Schöllhorn, 1992b) and/or (112) reflection from 2H (Downs & Hall-Wallace, 2003). 1.94 Å onset could be due to 1T (003) reflections (Fernando Wypych & Schöllhorn, 1992b). The strong peak feature at 2.32 Å can be assigned either due to 1T (201) reflection (Fernando Wypych & Schöllhorn, 1992b) or 2H (103) reflection (Downs & Hall-Wallace, 2003). 3.22 Å onset can be associated with the reflections from 2H (004) (Downs & Hall-Wallace, 2003) and/or 1T (110) (Fernando Wypych & Schöllhorn, 1992b). The onset at 3.88 Å is due to 1T (101), whereas, the strong peak feature at 4.74 Å can be attributed to the (100) reflection from 1T (Fernando Wypych & Schöllhorn, 1992b). A small onset at 5.64 Å could be due to the (001) peak from the restacked nanosheets (Fernando Wypych & Schöllhorn, 1992b). This indicates an additional separation of ~5.64 Å between layers during restacking and also reveals the monolayer nature of the exfoliated MoS_2 nanosheets to some extent (Acerce et al., 2015), (Huang et al., 2016), (P Joensen, E D Crozier, 1987). We do not observe any prominent peak feature at 6.15 Å corresponding to the interlayer spacing of MoS_2. However, a small onset at 6.9 Å seen in the profile [Figure.5.4(b)] could be attributed to the non stacked MoS_2 in the sample which exhibits nearly a similar interlayer spacing of bulk MoS_2. The absence of the 2H (002) and (105) peaks could be strong evidence for the presence of monolayers (Per Joensen, Frindt, & Morrison, 1986) in the exfoliated sample. The strong peak at 9.6 Å is assigned to the restacking of the MoS_2 layers after the MW assisted exfoliation along the c-axis. Wang *et al.* (D. Wang et al., 2017) have also seen a large interlayer spacing of 9.3 Å compared to

the bulk interplanar spacing of 6.15 Å which the authors have attributed to the insertion of ions and molecules (Acerce et al., 2015), (D. Wang et al., 2017), (P. Joensen, Crozier, Alberding, & Frindt, 1987) during the exfoliation process. The broadness of the 9.6 Å peak indicates that the nanosheets are randomly arranged during restacking, with large spacings between the layers. Structural stacking of the materials can change when the transition from bulk to the 2D state occurs during the liquid phase exfoliation process (Shmeliov et al., 2014). The non bulk stacking sequences can be derived from its bulk counterparts by translational shifts of the layers (Shmeliov et al., 2014) and such non bulk stacking could be quite dominant suggesting high possibility of unusual stacking sequence in 2D nanostructures (Shmeliov et al., 2014). Random stacking and the presence of 1T phase in our case are also indicated by the near-absence of the (002) and (105) peaks in the diffraction pattern (Per Joensen et al., 1986). We hardly observe any evidence of electron beam induced structural damage during the TEM investigations for electron beam energy of 300 keV and for exposure time up to several minutes on the suspended MoS_2 sheets which contain highly crystalline 1T-2H hybridized superlattice phase. HRTEM image of a MoS_2 layer shown in Figure 5.2(b) was acquired almost after 2 min of electron beam exposure. Due to such structural stability of the 1T-2H phase under electron beam of 300 keV, atomically resolved TEM micrographs were possible to acquire to probe the 2D layers in the mesoscopic regime and to understand the coplanar interface containing 1T-, 2H-domains. Similar TEM investigations carried out on MoS_2 sheets and nanostructures (Reshmi et al., 2017a) constituted mainly of 2H MoS_2 (S1), however, show a completely different behavior where immediate interaction of electron beam is observed [Figure.5.1]. According to our knowledge, there is only one report for the 2H phase with no significant structural damage or amorphization of MoS_2 sheets at 200 kV electron beam acceleration (Brivio, Alexander, & Kis, 2011). However, the authors hardly provide any insight in to the matter. In a drastic contrast to their results (Brivio et al., 2011), we find almost an instant structural damage and amorphisation by 300 keV electron beam for the 2H phase of MoS_2, whereas, a hybridized 1T-2H superlattice phase exhibits good structural stability towards the similar electron beam energy.

Radiation related damage on the surface of 2D materials have been addressed till date by various authors (Enyashin et al., 2011), (A.Garcia, A M Raya, M M Mariscal,R Esparza, M.Herrera, S I Molina, G Scavello, P L Galindo, 2014), (H.-P. Komsa et al., 2012). A detailed discussion related to radiation related damage has been described in chapter 3. Komsa *et al.* (H.-P. Komsa et al., 2012) have shown that the displacement thresholds for S atoms in the top layer facing the electron beam is around 8.1 eV which is considerably higher than for the bottom chalcogen layer with a displacement threshold of 6.9 eV because the displaced atom is 'stopped' by the other layers (Jana & Rao, 2016). The corresponding electron beam energy varies accordingly from 90 to 80 keV (H.-P. Komsa et al., 2012). Thus formation of vacancy columns is possible even at 80 keV of electron beam energy (Jana & Rao, 2016). Displacement threshold for transition metals is higher; about 20 eV is required to displace Mo atom from its site in the MoS_2 lattice which corresponds to an electron beam energy of 560 keV (H.-P. Komsa et al., 2012). As a result, TEM investigations of the 2D materials of TMDs at low energy will mainly be dominant by the damage related to radiolysis (Zan et al., 2013), (W. Zhou, Zou, Najmaei, Liu, Shi, Kong, & Lou, 2013), (Sadan, Houben, Enyashin, Seifert, & Tenne, 2008) of the chalcogen atoms.

For our case, a high energy of the electrons of 200–300 keV in the TEM studies would cause both knock-on and radiolysis to happen simultaneously on the exfoliated MoS_2 sheets and nanostructures. MoS_2 sheets become perforated following to the electron beam subjection by losing S atoms (Zan et al., 2013), (W. Zhou, Zou, Najmaei, Liu, Shi, Kong, & Lou, 2013), (Sadan et al., 2008), (X. Liu, Xu, Wu, Zhang, Yu, Qiu, Hong, Jin, et al., 2013), which creates hole on the surface. This hole extends under the scanning electrons and the less coordinated atoms at the edge of the holes assist the process related to the ionization damage (Zan et al., 2013). The knock-on mechanism of the edge atoms will also go on parallally due to a significantly lower threshold energy compared to the bulk (Zan et al., 2013) and a 200–300 keV of electron energy in our case is way above. Thus, 2H phase of MoS_2 (Reshmi et al., 2017a) seemed to be extremely

vulnerable under electron beam of high energy (200–300 keV) and within a minute of the electron beam exposure MoS_2 sheets and nanostructures decompose and melt into nanocrystallites [Figures.5.1(c)–(e), (g)]. These nano crystallites are obviously Mo rich due to S depletion induced by electron beam interaction (Rotunno et al., 2016), (A.Garcia, A M Raya, M M Mariscal,R Esparza, M.Herrera, S I Molina, G Scavello, P L Galindo, 2014).

Formation of ripples in 2D materials plays significant role to provide structural stability of the 2D sheets (Eda, Fujita, et al., 2012). Occurence of the microscopic corrugations in the 2D sheets can act as an additional source of scattering during the interaction of the electron beam with 2D layers. Ripples which are orginally created by thermal fluctuations and then become static or quenched after removing the thermal energy from the system or due to placing of the 2D layers on a substrate, can result in sufficient scattering of the electron beam (Katsnelson & Geim, 2008). Recently, by a new ReaxFF reactive force-field study (Ostadhossein et al., 2017), it is proposed that induction of a repeated series of propagating ripplocations over a given region of a MoS2 layer could potentially act to sweep out sulfur vacancies from that region. The electronic structure of the coplanar 1T-2H hybridized phase and the formation of the non bulk stacked layers would present the characteristics which might also be associated for the structural stability of the 1T-2H superlattice phase under electron beam studies.

5.4. Conclusion

Electron beam stability of sample S1 and S2 were investigated using HRTEM. S1 consisting of mostly 2H phase showed an immediate disintegration into nanocrstallites in the presence of high energy electron beam. On the other hand, for the sample S2, TEM measurements clearly display the induction of 1T phase in the 2H lattice which was due to the electron beam irradiation during the exfoliation process. HRTEM studies exhibit the formation of a coplanar 1T-2H heterogeneous coplanar superlattice phase with a higher concentration of 1T than 2H. From the atomically resolved TEM micrographs we estimated the

concentrations of the 1T- and the 2H- phase which are approximately 70% and 30% respectively. Evidence of surface ripplocations/ripples in the TEM measurements suggests the membrane folding mechanism which could be either due to MW assisted thermal effect on thin MoS_2 layers or due to strain induced by the formation of 1T- 2H superlattice phase or might have generated during the sample preparation process for the TEM studies on the Cu microgrids. We observed a structural stability of highly crystalline 1T-2H hybridized phase under a 300 keV electron beam which could be attributed to the formation of surface ripplocations or to the associated characteristics in the electronic structures of the 1T-2H coplanar phase or to the restacking of the exfoliated 2D layers. The ripplocations can act as an additional source of scattering centers and also the interaction of ripplocations and S vacancies could be an intriguing possibility to get rid of undesirable defects from particular regions of MoS_2 sheets with a pulse train of propagating ripplocations.

CHAPTER 6

CONCLUSIONS AND FUTURE PERSPECTIVES

6.1. Conclusions

Due to increased technological demands, the incorporation of nanostructured materials into device structures has received prior importance. In such reduced dimensions, the materials show enhanced electrical, electronic, optical and mechanical properties. On the other hand, with shrinking size, the conventional MS or MIS interfaces fail to perform due to the interdiffusion process. In such a scenario, 2D materials play a major role in overcoming the drawbacks of the conventional MS, MIS junctions. 2D materials like TMDs, exist in different polymorphic structures which show metallic (1T) as well as semiconducting (2H) nature, according to the atomic arrangement. The nanostructures of these TMDs materials exhibit novel electronic as well as optical properties making them a good candidate for various electronic and optoelectronic applications. A controlled production of metallic phase in a semiconducting matrix of TMDs can overcome the shortcomings of the conventional MS junction by reducing the strain due to lattice mismatch. Hence, there can be a considerable reduction in the potential barrier thus improving the performance of the devices.

We first provide a birds-eye view about the work that has been carried out throughout the thesis. A general discussion about synthesis of nanostructures, importance of nano dimension and the MS, MIS systems in technological applications, and the dominance of 2D materials with superior properties in these fields etc. have been addressed first.

Then a general overview of the conventional MS and MIS systems followed by our results and discussions related to Cu-SiO_2/Si system are discussed. We studied the growth and interaction of Cu at 600^{o}C on a 270 nm thick SiO_2 layer on Si(111) substrate. Growth of triangular voids on the surface is observed which follow substrate crystal symmetry. Deposition of Cu exhibits formation of sparsely distributed triangular islands *via* void filling mechanism. We find evidence of formation of Cu oxides and Cu silicides along with an intermediate Cu-O-Si phase in the grown film. Our XPS studies reveal that the

new intermediate Cu-O-Si phase dominates the composition (as high as ~ 41%) of the sample. Evidence of formation of all these phases could be associated with the growth parameters, thickness of the SiO_2 barrier, amount of deposited Cu, diffusion of Cu in the SiO_2/Si system and migration of Si towards the surface. Preliminary electrical characterizations show an overall behavior of the film which is not metallic.

This is followed by a detailed review on the exfoliation techniques used for isolating the layers of 2D materials, especially, MoS_2. Synthesis of nanostructures of MoS_2 using top down approach, influence of MW energy in the formation of the nanostructures, interaction of electron beam with 2D materials and the associated structural phase transformations are the main topics which have been discussed briefly. Then we discuss our method to synthesize MoS_2 nanostructures of spheres, rods/tubes and sheets by a simple modification of the traditional LPE where MW treatment at 175 °C was used after the exfoliation. We show that 1T domains can be induced in the original 2H lattice of MoS_2 by changing the MW exposure time from 10 (S1) to 30 (S2) min. Exfoliated and MW treated MoS_2 nano structures have been characterised using SEM, TEM, UV-Vis absorption spectroscopy, Raman spectroscopy and by PL studies. Our investigations reveal that the sample S1 is mainly constituted of 2H phase, whereas, in S2 1T phase dominates over 2H. Both the MW irradiated samples, S1 and S2 are comprised of MoS_2 nanostructures which exhibit good emission. However, the normalized PL spectra reveal a much higher emission from the 10 min MW assisted sample than that of 30 min. We attribute this difference in the emission to the semiconducting 2H and metallic 1T phase which comprises the samples respectively.

Finally, we discuss the structural stability of exfoliated MoS_2 sheets under high energy electron beam. HRTEM studies clearly demonstrate the formation of a coplanar 1T-2H heterogeneous superlattice phase in S2 with a higher concentration of 1T than 2H. From the atomically resolved TEM micrographs we estimated the concentrations of the 1T- and the 2H- phase which are approximately 70% and 30% respectively. We also find evidence of surface

ripplocations/ripples in the TEM micrographs which suggests the membrane folding mechanism either due to MW assisted thermal effect on thin MoS_2 layers or due to strain induced by the formation of 1T-2H superlattice phase or might have generated during the sample preparation process for the TEM studies on the Cu microgrids. The structural stability observed by highly crystalline 1T-2H hybridized phase under a 300 keV electron beam could be attributed to the formation of surface ripplocations or to the associated characteristics in the electronic structures of the 1T-2H coplanar phase or to the restacking of the exfoliated 2D layers. The ripplocations can act as an additional source of scattering centers and also the interaction of ripplocations and the S vacancies could be an intriguing possibility to get rid of undesirable defects from particular regions of MoS_2 sheets with a pulse train of propagating ripplocations. On the other hand, we observed that sample S1 consisting of mostly 2H phase showed an immediate disintegration into nanocrstallites in the presence of high energy electron beam. This study corresponding to structural stability of 1T-2H hybridized sharp MS junction with less strain can have important technological applications.

6.2. Future perspectives

Through our experimental studies, we have observed a high structural stability for the mixed 1T-2H phase of MoS_2. This hybrid phase is shown to withstand an electron beam of extremely high energy of 300 keV. A theoretical validation of this result can provide further insights into the kinetics and energetics of formation of such a coplanar phase and the role of MW irradiation. Previous reports have shown that the ripples present on the surface of 2D materials can act as additional scattering center for the beam, thereby providing the stability. However, a theoretical insight related to the formation of the hybridized phase and the ripples in the MW treated samples will aid to understand quantitatively the roles of these on providing the stability to the mixed phase of MoS_2.

BIBLIOGRAPHY

1. A.Garcia, A M Raya, M M Mariscal,R Esparza, M.Herrera, S I Molina, G Scavello, P L Galindo, M. J.-Y. and A. ponce. (2014). Analysis of electron

beam damage of exfoliated MoS2 sheets by quantitative HAADF-STEM imaging. *Ultramicroscopy*, *146*, 33–38. https://doi.org/10.1038/jid.2014.371

2. Aboelfotoh, M. O., Krusinelbaum, L., & Aboelfotoh, M. (1991). Electrical transport in thin films of copper silicide. *Journal of Applied Physics*, *70*(6), 3382–3384. https://doi.org/10.1063/1.349280

3. Acerce, M., Voiry, D., & Chhowalla, M. (2015). Metallic 1T phase MoS2 nanosheets as supercapacitor electrode materials. *Nature Nanotechnology*, *10*(4), 313–318. https://doi.org/10.1038/nnano.2015.40

4. Albiter, M. a, Huirache-Acuña, R., Paraguay-Delgado, F., Rico, J. L., & Alonso-Nuñez, G. (2006). Synthesis of MoS 2 nanorods and their catalytic test in the HDS of dibenzothiophene. *Nanotechnology*, *17*(14), 3473–3481. https://doi.org/10.1088/0957-4484/17/14/020

5. Algara-Siller, G., Kurasch, S., Sedighi, M., Lehtinen, O., & Kaiser, U. (2013). The pristine atomic structure of MoS2 monolayer protected from electron radiation damage by graphene. *Applied Physics Letters*, *103*(20). https://doi.org/10.1063/1.4830036

6. Arellano, U., Shen, J. M., Wang, J. A., Timko, M. T., Chen, L. F., Vázquez Rodríguez, J. T., … Llanos, M. E. (2015). Dibenzothiophene oxidation in a model diesel fuel using CuO/GC catalysts and H2O2in the presence of acetic acid under acidic condition. *Fuel*, *149*, 15–25. https://doi.org/10.1016/j.fuel.2014.11.001

7. Ataca, C., Topsakal, M., Aktürk, E., & Ciraci, S. (2011). A comparative study of lattice dynamics of three- and two-dimensional MoS2. *Journal of Physical Chemistry C*. https://doi.org/10.1021/jp205116x

8. Backes, C., Smith, R. J., McEvoy, N., Berner, N. C., McCloskey, D., Nerl, H. C., … Coleman, J. N. (2014). Edge and confinement effects allow in situ measurement of size and thickness of liquid-exfoliated nanosheets. *Nature Communications*. https://doi.org/10.1038/ncomms5576

9. Balendhran, S., Ou, J. Z., Bhaskaran, M., Sriram, S., Ippolito, S., Vasic, Z., … Kalantar-zadeh, K. (2012). Atomically thin layers of MoS 2 via a two step thermal evaporation–exfoliation method. *Nanoscale*, *4*(2), 461–466. https://doi.org/10.1039/C1NR10803D

10. Banhart, F., Kotakoski, J., & Krasheninnikov, A. V. (n.d.). Structural Defects in Graphene, *5*(1).

11. Bastide, S., Duphil, D., Borra, J. P., & Lévy-Clément, C. (2006). WS2 closed nanoboxes synthesized by spray pyrolysis. *Advanced Materials*. https://doi.org/10.1002/adma.200501735

12. Benito, N., & Palacio, C. (2014). Mixed Ti-O-Si oxide films formation by oxidation of titanium-silicon interfaces. *Applied Surface Science*, *301*, 436–441. https://doi.org/10.1016/j.apsusc.2014.02.094

13. Benito, Noelia, & Flores, M. (2017). Evidence of Mixed Oxide Formation on the Cu / SiO 2 Interface. *The Journal of Physical Chemistry C*, *121*(34), 18771–18778. https://doi.org/10.1021/acs.jpcc.7b06563

14. Benouattas, N., & Mosser, A. (2000). Behaviour of copper atoms in annealed Cu/ SiO x / Si systems. *Applied Surface Science*, *153*, 79–84.

15. Benouattas, N., Mosser, A., & Bouabellou, A. (2006). Surface morphology and reaction at Cu / Si interface — Effect of native silicon suboxide, *252*, 7572–7577. https://doi.org/10.1016/j.apsusc.2005.09.010

16. Bergin, S. D., Nicolosi, V., Streich, P. V., Giordani, S., Sun, Z., Windle, A. H., … Coleman, J. N. (2008). Towards solutions of single-walled carbon nanotubes in common solvents. *Advanced Materials*. https://doi.org/10.1002/adma.200702451

17. Bernal, M. M., & Milano, D. (2014). Two-dimensional nanomaterials via liquid-phase exfoliation: synthesis, properties and applications. In *Carbon Nanotechnology* (pp. 159–185).

18. Bertolazzi, S., Jacopo, B., & Andras, K. (2011). Stretching and Breaking of

Ultrathin MoS2. *ACS Nano*, *5*(12), 9703–9709. Retrieved from http://pubs.acs.org/doi/pdf/10.1021/nn203879f

19. Bhar, S. K., Mukherjee, N., Maji, S. K., Adhikary, B., & Mondal, A. (2010). Synthesis of nanocrystalline iron oxide ultrathin films by thermal decomposition of iron nitropruside: Structural and optical properties. *Materials Research Bulletin*. https://doi.org/10.1016/j.materresbull.2010.08.006

20. Bissessur, R., & Kannewurfb, C. R. (1993). Encapsulation of Polymers into MoS2 and Metal to Insulator Transition in Metastable. *J. Chem. Soc., Chem. Commun.*, (20), 1582–1585.

21. Bo, C., Yan-hui, J., Gong-Ping, L., & Xi-Meng, C. (2010). Atomic diffusion in annealed Cu / SiO 2 / Si (100) system prepared by magnetron sputtering. *Chinese Physics B*, *19*(2), 1–4.

22. Bregadiolli, B. A., Fernandes, S. L., & De Oliveira Graeff, C. F. (2017). Easy and fast preparation of TiO2 -based nanostructures using microwave assisted hydrothermal synthesis. *Materials Research*. https://doi.org/10.1590/1980-5373-MR-2016-0684

23. Brivio, J., Alexander, D. T. L., & Kis, A. (2011). Ripples and layers in ultrathin MoS 2 membranes. *Nano Letters*, *11*(12), 5148–5153. https://doi.org/10.1021/nl2022288

24. Cai, L., He, J., Liu, Q., Yao, T., Chen, L., Yan, W., … Wei, S. (2015). Vacancy-Induced Ferromagnetism of MoS 2 Nanosheets. *Journal of the American Chemical Society*, *137*(7), 2622–2627. https://doi.org/10.1021/ja5120908

25. Caldwell, M. A., Haynor, B., Aloni, S., Ogletree, D. F., Wong, H. S. P., Urban, J. J., & Milliron, D. J. (2010). Spectroscopic evidence for exceptional thermal contribution to electron beam-induced fragmentation. *Journal of Physical Chemistry C*. https://doi.org/10.1021/jp1078086

26. Castellanos-Gomez, A., Barkelid, M., Goossens, A. M., Calado, V. E., Van Der Zant, H. S. J., & Steele, G. A. (2012). Laser-thinning of MoS 2: On demand generation of a single-layer semiconductor. *Nano Letters*. https://doi.org/10.1021/nl301164v

27. Cetin, H., & Ayyildiz, E. (2005). Temperature dependence of electrical parameters of the Au/n-InP Schottky barrier diodes. *Semiconductor Science and Technology*, *20*(6), 625–631. https://doi.org/10.1088/0268-1242/20/6/025

28. Chand, S., & Kumar, J. (1997). Effects of barrier height distribution on the behavior of a Schottky diode. *Journal of Applied Physics*, *82*(10), 5005–5010. https://doi.org/10.1063/1.366370

29. Chen, R. X., Zhu, S. L., Mao, J., Cui, Z. D., Yang, X. J., Liang, Y. Q., & Li, Z. Y. (2015). Synthesis of CuO / Co 3 O 4 Coaxial Heterostructures for Efficient and Recycling Photodegradation. *International Journal of Photoenergy*, *2015*, 1–11.

30. Cheng, P., Sun, K., & Hu, Y. H. (2016). Mechanically-induced reverse phase transformation of MoS2 from stable 2H to metastable 1T and its memristive behavior. *RSC Advances*. https://doi.org/10.1039/c6ra12735e

31. Chhowalla, M., Shin, H. S., Eda, G., Li, L. J., Loh, K. P., & Zhang, H. (2013). The chemistry of two-dimensional layered transition metal dichalcogenide nanosheets. *Nature Chemistry*. https://doi.org/10.1038/nchem.1589

32. Chico, L., Jaskólski, W., López-Sancho, M. P., & Muñoz, M. C. (2005). Quantum confinement in carbon-nanotube systems. *International Journal of Nanotechnology*, *2*(1–2), 103–113.

33. Chou, S. S., Sai, N., Lu, P., Coker, E. N., Liu, S., Artyushkova, K., … Brinker, C. J. (2015). Understanding catalysis in a multiphasic two-dimensional transition metal dichalcogenide. *Nature Communications*, *6*, 1–8. https://doi.org/10.1038/ncomms9311

34. Chuvilin, A., Meyer, J. C., Algara-Siller, G., & Kaiser, U. (2009). From graphene constrictions to single carbon chains. *New Journal of Physics*. https://doi.org/10.1088/1367-2630/11/8/083019

35. Ci, L., Song, L., Jin, C., Jariwala, D., Wu, D., Li, Y., … Ajayan, P. M. (2010). Atomic layers of hybridized boron nitride and graphene domains. *Nature Materials*, *9*(5), 430–435. https://doi.org/10.1038/nmat2711

36. Ciesielski, A., & Samorì, P. (2014). Graphene via sonication assisted liquid-phase exfoliation. *Chem. Soc. Rev.*, *43*(1), 381–398. https://doi.org/10.1039/C3CS60217F

37. Coehoorn, R., Haas, C., Dijkstra, J., Flipse, C. J. F., de Groot, R. A., & Wold, A. (1987). Electronic structure of MoSe2, MoS2, and WSe2. I. Band-structure calculations and photoelectron spectroscopy. *Physical Review B*, *35*(12), 6195–6202. https://doi.org/10.1103/PhysRevB.35.6195

38. Coleman, J. N., Lotya, M., O'Neill, A., Bergin, S. D., King, P. J., Khan, U., … Nicolosi, V. (2011). Two-Dimensional Nanosheets Produced by Liquid Exfoliation of Layered Materials. *Science*, *331*(6017), 568–571. https://doi.org/10.1126/science.1194975

39. Coleman, Jonathan N. (2009). Liquid-phase exfoliation of nanotubes and graphene. *Advanced Functional Materials*. https://doi.org/10.1002/adfm.200901640

40. Collins, M. J. (2010). Future trends in microwave synthesis. *Future Medicinal Chemistry*. https://doi.org/10.4155/fmc.09.133

41. Cowley, R. A. (1965). Raman scattering from crystals of the diamond structure. *J. Phys. France*, *26*(11), 659–667.

42. Cros, A., Aboelfotoh, M. O., & Tu, K. N. (1990). Formation, oxidation, electronic, and electrical properties of copper silicides. *Journal of Applied Physics*, *67*, 3328–3336. https://doi.org/10.1063/1.345369

43. Cunningham, G., Lotya, M., Cucinotta, C. S., Sanvito, S., Bergin, S. D.,

Menzel, R., … Coleman, J. N. (2012). Solvent exfoliation of transition metal dichalcogenides: Dispersibility of exfoliated nanosheets varies only weakly between compounds. *ACS Nano*. https://doi.org/10.1021/nn300503e

44. Dallinger, D., & Kappe, C. O. (2007). Microwave-assisted synthesis in water as solvent. *Chemical Reviews*. https://doi.org/10.1021/cr0509410

45. Das, S., Chen, H. Y., Penumatcha, A. V., & Appenzeller, J. (2013). High performance multilayer MoS2 transistors with scandium contacts. *Nano Letters*, *13*(1), 100–105. https://doi.org/10.1021/nl303583v

46. Dhas, N. A., & Suslick, K. S. (2005). Sonochemical preparation of hollow nanospheres and hollow nanocrystals. *Journal of the American Chemical Society*. https://doi.org/10.1021/ja049494g

47. Diamandescu, L., Vasiliu, F., Tarabasanu-Mihaila, D., Feder, M., Vlaicu, A. M., Teodorescu, C. M., … Vasile, E. (2008). Structural and photocatalytic properties of iron- and europium-doped TiO 2 nanoparticles obtained under hydrothermal conditions. *Materials Chemistry and Physics*. https://doi.org/10.1016/j.matchemphys.2008.05.023

48. Dickinson, R. G., & Pauling, L. (1923). THE CRYSTAL STRUCTURE OF MOLYBDENITE. *Journal of the American Chemical Society*, *45*(6), 1466–1471. https://doi.org/10.1021/ja01659a020

49. Dodoo-Arhin, D., Howe, R. C. T., Hu, G., Zhang, Y., Hiralal, P., Bello, A., … Hasan, T. (2016). Inkjet-printed graphene electrodes for dye-sensitized solar cells. *Carbon*, *105*, 33–41. https://doi.org/10.1016/j.carbon.2016.04.012

50. Dolbak, A. E., Zhachuk, R. A., & Olshanetsky, B. Z. (2003). Mechanism of Cu transport along clean Si surfaces . *Central European Journal of Physics*, *3*, 463–473. https://doi.org/10.2478/BF02475857

51. Dolling, G., & Cowley, A. (1966). The thermodynamic and optical germanium, silicon, diamond an arsenide. *Proc. Phys. Soc*, *88*, 463. Retrieved from http://iopscience.iop.org/0370-1328/88/2/318/pdf

52. Dominko, R., Arčon, D., Mrzel, A., Zorko, A., Cevc, P., Venturini, P., … Mihailovic, D. (2002). Dichalcogenide nanotube electrodes for Li-ion batteries. *Advanced Materials*, *14*(21), 1531–1534. https://doi.org/10.1002/1521-4095(20021104)14:21<1531::AID-ADMA1531>3.0.CO;2-P

53. Downs, R. T., & Hall-Wallace, M. (2003). The American Mineralogist crystal structure database. *American Mineralogist*, *88*(1), 247–250.

54. Du, X., Takeguchi, M., Tanaka, M., & Furuya, K. (2003). Formation of crystalline Si nanodots in SiO2 films by electron irradiation. *Applied Physics Letters*, *82*(7), 1108–1110. https://doi.org/10.1063/1.1555691

55. E.'Sobol, J. F. M. W. F. S. P., & Bomben, K. D. (1992). Handbook of X-ray Photoelectron Spectroscopy. *Perkin-Elmer Corporation , Physical Electronics Division*.

56. Eda, G., Fujita, T., Yamaguchi, H., Voiry, D., Chen, M., & Chhowalla, M. (2012). Coherent atomic and electronic heterostructures of single-layer MoS 2. *ACS Nano*, *6*(8), 7311–7317. https://doi.org/10.1021/nn302422x

57. Eda, G., Yamaguchi, H., Voiry, D., Fujita, T., Chen, M., & Chhowalla, M. (2011). Photoluminescence from chemically exfoliated MoS 2. *Nano Letters*. https://doi.org/10.1021/nl201874w

58. Eda, G., Yamaguchi, H., Voiry, D., Fujita, T., Chen, M., & Chhowalla, M. (2012). Photoluminescence from Chemically Exfoliated MoS 2. *Nano Letters*, *12*(1), 526–526. https://doi.org/10.1021/nl2044887

59. Egerton, R. F. (2013). Control of radiation damage in the TEM. *Ultramicroscopy*. https://doi.org/10.1016/j.ultramic.2012.07.006

60. Egerton, R. F., Li, P., & Malac, M. (2004). Radiation damage in the TEM and SEM. In *Micron*. https://doi.org/10.1016/j.micron.2004.02.003

61. Egerton, R. F., McLeod, R., Wang, F., & Malac, M. (2010). Basic questions related to electron-induced sputtering in the TEM. *Ultramicroscopy*.

https://doi.org/10.1016/j.ultramic.2009.11.003

62. Ektessabi, A. M. (1993). Temperature dependence of atomic mixing at the copper-silicon interface. *Thin Solid Films*, *236*, 135–139.

63. Enyashin, a N., Yadgarov, L., Houben, L., Popov, I., Weidenbach, M., Tenne, R., … Seifert, G. (2011). New Route for Stabilization of 1T-WS2 and MoS2 Phases. *Journal of Physical Chemistry C*, *115*(50), 24586–24591. https://doi.org/Doi 10.1021/Jp2076325

64. Fang, X., Bando, Y., Gautam, U. K., Ye, C., & Golberg, D. (2008). Inorganic semiconductor nanostructures and their field-emission applications. *Journal of Materials Chemistry*. https://doi.org/10.1039/b712874f

65. Fasolino, A., Los, J. H., & Katsnelson, M. I. (2007). Intrinsic ripples in graphene. *Nature Materials*, *6*(11), 858–861. https://doi.org/10.1038/nmat2011

66. Fei, J., Meng, L., Nie, T., & Luan, Y. (2017). Electronic properties of 1T-MoS 2 nanoribbon and its homojunction nanoribbon. *Physica Status Solidi (B)*, *254*(6), 1600728. https://doi.org/10.1002/pssb.201600728

67. Feng, X., Hu, M., Zhou, J., Gong, S., Zhao, T., Zhong, R., & Liu, S. (2018). Preliminary experimental study of graphene-based terahertz radiation excited by an electron beam. In *2018 IEEE International Vacuum Electronics Conference, IVEC 2018*. https://doi.org/10.1109/IVEC.2018.8391577

68. Fernando, C. A. N., & Wetthasinghe, S. K. (2000). Investigation of photoelectrochemical characteristics of n-type Cu2O films. *Solar Energy Materials and Solar Cells*, *63*, 299–308.

69. Forsberg, V., Zhang, R., Bäckström, J., Dahlström, C., Andres, B., Norgren, M., … Olin, H. (2016). Exfoliated MoS2 in Water without Additives. *PloS One*, *11*(4), e0154522. https://doi.org/10.1371/journal.pone.0154522

70. Frey, G. L., Elani, S., Homyonfer, M., Feldman, Y., & Tenne, R. (1998). Optical-absorption spectra of inorganic fullerenelike MS2 (M= Mo, W).

Physical Review B, *57*(11), 6666–6671. https://doi.org/10.1103/PhysRevB.57.6666

71. Friedman, A. L., Aubrey, T. H., Perkins, F. K., Jernigan, G. G., James, C., & Campbell, P. M. (2017). Evidence for Chemical Vapor Induced 2H to 1T Phase Transition in MoX2 (X = Se , S) Transition Metal Dichalcogenide Films. *Scientific Reports*, *7*, 1–9. https://doi.org/10.1038/s41598-017-04224-4

72. Gabriel, C., Gabriel, S., Grant, E. H., Halstead, B. S. J., & Michael P Mingos, D. (1998). Dielectric parameters relevant to microwave dielectric heating. *Chemical Society Reviews*. https://doi.org/10.1039/a827213z

73. Gao, B., & Zhang, X. (2014). Synthesis of MoS2 Inorganic Fullerene-like Nanoparticles by a Chemical Vapour Deposition Method. *The South African Journal of Chemistry*, *67*(1), 6–11.

74. Geaney, H., Dickinson, C., Dwyer, C. O., Mullane, E., Singh, A., & Ryan, K. M. (2012). Growth of Crystalline Copper Silicide Nanowires in High Yield within a High Boiling Point Solvent System. *Chemistry of Materials*, *24*, 4319–4325.

75. Geim, A. K., & Grigorieva, I. V. (2013). Van der Waals heterostructures. *Nature*, *499*(7459), 419–425. https://doi.org/10.1038/nature12385

76. Geim, A. K., & Novoselov, K. S. (2007). The rise of graphene. *Physical Review Letters*, *77*(18), 3865–3868. https://doi.org/10.1103/PhysRevLett.77.3865

77. Ghorbani-Asl, M., Zibouche, N., Wahiduzzaman, M., Oliveira, A. F., Kuc, A., & Heine, T. (2013). Electromechanics in MoS2 and WS2: nanotubes vs. monolayers, 1–19. https://doi.org/10.1038/srep02961

78. Gonzalez-Martinez, I. G., Bachmatiuk, A., Bezugly, V., Kunstmann, J., Gemming, T., Liu, Z., … Rümmeli, M. H. (2016). Electron-beam induced synthesis of nanostructures: A review. *Nanoscale*.

https://doi.org/10.1039/c6nr01941b

79. Grimaldi, M. G., Wieluński, L., Nicolet, M.-A., & Tu, K. N. (1981). Germanide formation by thermal treatment of platinum films deposited on single-crystal Ge〈100〉 substrates. *Thin Solid Films*, *81*(3), 207–211. https://doi.org/10.1016/0040-6090(81)90483-1

80. Gruber, J., Lang, A. C., Griggs, J., Taheri, M. L., Tucker, G. J., & Barsoum, M. W. (2016). Evidence for Bulk Ripplocations in Layered Solids. *Scientific Reports*, *6*(February), 1–8. https://doi.org/10.1038/srep33451

81. Guardia, L., Paredes, J. I., Rozada, R., Villar-Rodil, S., Martínez-Alonso, A., & Tascón, J. M. D. (2014). Production of aqueous dispersions of inorganic graphene analogues by exfoliation and stabilization with non-ionic surfactants. *RSC Advances*. https://doi.org/10.1039/c4ra00212a

82. Guo, Y., Sun, D., Ouyang, B., Raja, A., Song, J., Heinz, T. F., & Brus, L. E. (2015). Probing the Dynamics of the Metallic-to-Semiconducting Structural Phase Transformation in MoS $_2$ Crystals. *Nano Letters*, *15*(8), 5081–5088. https://doi.org/10.1021/acs.nanolett.5b01196

83. H Dallaporta, M Liehr, J. E. L. (1990). Silicon dioxide defects induced by metal impurities. *Physical Review B*, *41*(8), 5075.

84. Halim, U., Zheng, C. R., Chen, Y., Lin, Z., Jiang, S., Cheng, R., … Duan, X. (2013). A rational design of cosolvent exfoliation of layered materials by directly probing liquid–solid interaction. *Nature Communications*, *4*(1), 2213. https://doi.org/10.1038/ncomms3213

85. Han, K., & Tao, M. (2009). Electrochemically deposited p-n homojunction cuprous oxide solar cells. *Solar Energy Materials and Solar Cells*, *93*(1), 153–157. https://doi.org/10.1016/j.solmat.2008.09.023

86. Han, M., Jiang, K., Zhang, J., Yu, W., Li, Y., Hu, Z., & Chu, J. (2012). Structural, electronic band transition and optoelectronic properties of delafossite CuGa1−xCrxO2 ($0 \leq x \leq 1$) solid solution films grown by the

sol–gel method. *Journal of Materials Chemistry*, *22*(35), 18463. https://doi.org/10.1039/c2jm33027j

87. Han, S., Luo, X., Cao, Y., Yuan, C., Yang, Y., Li, Q., … Ye, S. (2015). Morphology evolution of MoS2 nanorods grown by chemical vapor deposition. *Journal of Crystal Growth*, *430*(November), 1–6. https://doi.org/10.1016/j.jcrysgro.2015.08.005

88. Hansen, L. P., Ramasse, Q. M., Kisielowski, C., Brorson, M., Johnson, E., Topsøe, H., & Helveg, S. (2011). Atomic-Scale Edge Structures on Industrial-Style MoS2 Nanocatalysts. *Angewandte Chemie International Edition*, *50*(43), 10153–10156. https://doi.org/10.1002/anie.201103745

89. Hashimoto, A., Suenaga, K., Gloter, A., Urita, K., & Iijima, S. (2004). Direct evidence for atomic defects in graphene layers. *Nature*. https://doi.org/10.1038/nature02817

90. Heising, J., & Kanatzidis, M. G. (1999). Structure of Restacked MoS 2 and WS 2 Elucidated by Electron Crystallography. *J. Am. Chem. Soc.*, *121*(12), 638–643. https://doi.org/10.1021/ja983043c

91. Hobbs, R. G., Petkov, N., & Holmes, J. D. (2012). Semiconductor nanowire fabrication by bottom-up and top-down paradigms. *Chemistry of Materials*, *24*(11), 1975–1991. https://doi.org/10.1021/cm300570n

92. Hu, Z., Zhang, S., Zhang, Y. N., Wang, D., Zeng, H., & Liu, L. M. (2015b). Modulating the phase transition between metallic and semiconducting single-layer MoS2 and WS2 through size effects. *Physical Chemistry Chemical Physics*. https://doi.org/10.1039/c4cp04775c

93. Huang, H., Cui, Y., Li, Q., Dun, C., Zhou, W., Huang, W., … Carroll, D. L. (2016). Metallic 1T phase MoS2 nanosheets for high-performance thermoelectric energy harvesting. *Nano Energy*, *26*, 172–179. https://doi.org/10.1016/j.nanoen.2016.05.022

94. Ikeda, T., Kamo, T., & Danno, M. (1995). New synthesis method of

fullerenes using microwave-induced naphthalene-nitrogen plasma at atmospheric pressure. *Applied Physics Letters*, *67*(7), 900–902. https://doi.org/10.1063/1.114688

95. In-Chul Kim, Dongjin Byun, Sangwha Lee, J. K. L. (2006). Electrochemical characteristics of silicon-metals coated graphites for anode materials of lithium secondary batteries. *Electrochimica Acta*, *52*, 1532–1537. https://doi.org/10.1007/s10832-006-0386-z

96. Istratov, A. A., Flink, C., Hieslmair, H., Weber, E. R., & Heiser, T. (1998). Intrinsic Diffusion Coefficient of Interstitial Copper in Silicon. *Physical Review Letters*, *81*(6), 1243–1246.

97. J.R. Shi , S.P. Lau, Z. Sun, X. Shi, B.K. Tay, H. S. T. (2001). Structural and electrical properties of copper thin films prepared by filtered cathodic vacuum arc technique. *Surface and Coatings Technology*, *138*, 250–255. https://doi.org/10.1016/j.jcrysgro.2004.04.098

98. Jana, M. K., & Rao, C. N. R. (2016). Two-dimensional inorganic analogues of graphene: transition metal dichalcogenides. *Philosophical Transactions of the Royal Society A: Mathematical, Physical and Engineering Sciences*, *374*(2076), 20150318. https://doi.org/10.1098/rsta.2015.0318

99. Jawaid, A., Nepal, D., Park, K., Jespersen, M., Qualley, A., Mirau, P., … Vaia, R. A. (2016). Mechanism for Liquid Phase Exfoliation of MoS2. *Chemistry of Materials*, *28*(1), 337–348. https://doi.org/10.1021/acs.chemmater.5b04224

100. Jiang, L., Zhang, S., Kulinich, S. A., Song, X., Zhu, J., Wang, X., & Zeng, H. (2015). Optimizing hybridization of 1T and 2H phases in MoS2 monolayers to improve capacitances of supercapacitors. *Materials Research Letters*, *3*(4), 177–183. https://doi.org/10.1080/21663831.2015.1057654

101. Jiménez Sandoval, S., Yang, D., Frindt, R. F., & Irwin, J. C. (1991). Raman study and lattice dynamics of single molecular layers ofMoS2. *Physical Review B*, *44*(8), 3955–3962. https://doi.org/10.1103/PhysRevB.44.3955

102. Jin, Z., Li, X., Mullen, J. T., & Kim, K. W. (2014). Intrinsic transport properties of electrons and holes in monolayer transition-metal dichalcogenides. *Physical Review B*, *90*(4), 045422. https://doi.org/10.1103/PhysRevB.90.045422

103. Joensen, P., Crozier, E. D., Alberding, N. A., & Frindt, R. F. (1987). A study of single-layer and restacked MoS2 by X-ray diffraction and X-ray absorption spectroscopy. *Journal of Physics C: Solid State Physics*. https://doi.org/10.1088/0022-3719/20/26/009

104. Joensen, Per, Frindt, R. F., & Morrison, S. R. (1986). Single-layer MoS2. *Materials Research Bulletin*. https://doi.org/10.1016/0025-5408(86)90011-5

105. Kan, M., Wang, J. Y., Li, X. W., Zhang, S. H., Li, Y. W., Kawazoe, Y., … Jena, P. (2014). Structures and Phase Transition of a MoS 2 Monolayer. *The Journal of Physical Chemistry C*, *118*(3), 1515–1522. https://doi.org/10.1021/jp4076355

106. Kang, Y., Najmaei, S., Liu, Z., Bao, Y., Wang, Y., Zhu, X., … Fang, Z. (2014). Plasmonic Hot Electron Induced Structural Phase Transition in a MoS 2 Monolayer. *Advanced Materials*, *26*(37), 6467–6471. https://doi.org/10.1002/adma.201401802

107. Kappera, R., Voiry, D., Yalcin, S. E., Jen, W., Acerce, M., Torrel, S., … Chhowalla, M. (2014). Metallic 1T phase source/drain electrodes for field effect transistors from chemical vapor deposited MoS2. *APL Materials*, *2*(9), 092516. https://doi.org/10.1063/1.4896077

108. Katsnelson, M. ., & Geim, A. . (2008). Electron scattering on microscopic corrugations in graphene. *Philosophical Transactions of the Royal Society A: Mathematical, Physical and Engineering Sciences*, *366*(1863), 195–204. https://doi.org/10.1098/rsta.2007.2157

109. Kester, E., Gillot, B., Perriat, P., Dufour, P., Villette, C., Tailhades, P., & Rousset, A. (1996). Thermal Behavior and Cation Distribution of Submicron Copper Ferrite Spinels CuxFe3−xO4(0 ≤x≤ 0.5) Studied by DTG, FTIR, and

XPS. *Journal of Solid State Chemistry*, *126*(1), 7–14. https://doi.org/10.1006/jssc.1996.0302

110. Kharissova, O. V. (2004). Vertically aligned carbon nanotubes fabricated by microwaves. *Reviews on Advanced Materials Science*.

111. Kibsgaard, J., Lauritsen, J. V., Lægsgaard, E., Clausen, B. S., Topsøe, H., & Besenbacher, F. (2006). Cluster−Support Interactions and Morphology of MoS 2 Nanoclusters in a Graphite-Supported Hydrotreating Model Catalyst. *Journal of the American Chemical Society*, *128*(42), 13950–13958. https://doi.org/10.1021/ja0651106

112. Kim, J., Kwon, S., Cho, D. H., Kang, B., Kwon, H., Kim, Y., … Lee, C. (2015). Direct exfoliation and dispersion of two-dimensional materials in pure water via temperature control. *Nature Communications*. https://doi.org/10.1038/ncomms9294

113. KO, E., HWANG, J., KIM, J. H., LEE, J. H., LEE, S. H., TRAN, V.-K., … SEONG, G. H. (2016). Electrochemical Fabrication of Nanostructures on Porous Silicon for Biochemical Sensing Platforms. *Analytical Sciences*, *32*(6), 681–686. https://doi.org/10.2116/analsci.32.681

114. Koffyberg, F. P., & Benko, F. A. (1982). A photoelectrochemical determination of the position of the conduction and valence band edges of p-type CuO. *Journal of Applied Physics*, *53*, 1173–1177. https://doi.org/10.1063/1.330567

115. Kolobov, A. V., & Tominaga, J. (2016). *Two-Dimensional Transition-Metal Dichalcogenides*. (R. Hull, C. Jagadish, Y. Kawazoe, R. M. Osgood, J. Parisi, T.-Y. Seong, … Z. M. Wang, Eds.) (Vol. 239). Cham: Springer International Publishing. https://doi.org/10.1007/978-3-319-31450-1

116. Komarneni, S., Roy, R., & Li, Q. H. (1992). Microwave-hydrothermal synthesis of ceramic powders. *Materials Research Bulletin*. https://doi.org/10.1016/0025-5408(92)90004-J

117. Komsa, H.-P., Kotakoski, J., Kurasch, S., Lehtinen, O., Kaiser, U., & Krasheninnikov, A. V. (2012). Two-Dimensional Transition Metal Dichalcogenides under Electron Irradiation: Defect Production and Doping. *Physical Review Letters*, *109*(3), 035503. https://doi.org/10.1103/PhysRevLett.109.035503

118. Kotakoski, J., Krasheninnikov, A. V., Kaiser, U., & Meyer, J. C. (2011). From point defects in graphene to two-dimensional amorphous carbon. *Physical Review Letters*. https://doi.org/10.1103/PhysRevLett.106.105505

119. Kouroupis-Agalou, K., Liscio, A., Treossi, E., Ortolani, L., Morandi, V., Pugno, N. M., & Palermo, V. (2014). Fragmentation and exfoliation of 2-dimensional materials: A statistical approach. *Nanoscale*. https://doi.org/10.1039/c3nr06919b

120. Krivanek, O. L., Chisholm, M. F., Nicolosi, V., Pennycook, T. J., Corbin, G. J., Dellby, N., … Pennycook, S. J. (2010). Atom-by-atom structural and chemical analysis by annular dark-field electron microscopy. *Nature*. https://doi.org/10.1038/nature08879

121. Kuc, A., Zibouche, N., & Heine, T. (2011). Influence of quantum confinement on the electronic structure of the transition metal sulfide TS2. *Physical Review B*, *83*(24), 245213. https://doi.org/10.1103/PhysRevB.83.245213

122. Kuemmeth, F., Ilani, S., Ralph, D. C., & McEuen, P. L. (2008). Coupling of spin and orbital motion of electrons in carbon nanotubes. *Nature*, *452*(7186), 448–452. https://doi.org/10.1038/nature06822

123. Kumar, R., Singh, R. K., Savu, R., Dubey, P. K., Kumar, P., & Moshkalev, S. A. (2016). Microwave-assisted synthesis of void-induced graphene-wrapped nickel oxide hybrids for supercapacitor applications. *RSC Advances*. https://doi.org/10.1039/c6ra00426a

124. Kumar, R., Singh, R. K., Singh, D. P., Savu, R., & Moshkalev, S. A. (2016). Microwave heating time dependent synthesis of various dimensional

graphene oxide supported hierarchical ZnO nanostructures and its photoluminescence studies. *Materials and Design*. https://doi.org/10.1016/j.matdes.2016.09.018

125. Kumar, R., Singh, R. K., Vaz, A. R., & Moshkalev, S. A. (2015). Microwave-assisted synthesis and deposition of a thin ZnO layer on microwave-exfoliated graphene: optical and electrochemical evaluations. *RSC Advances*. https://doi.org/10.1039/c5ra09936f

126. Kumara, A., & Ahluwalia, P. K. (2012). Electronic structure of transition metal dichalcogenides monolayers 1H-MX2 (M = Mo, W; X = S, Se, Te) from ab-initio theory: New direct band gap semiconductors. *European Physical Journal B*, *85*(6), 18–22. https://doi.org/10.1140/epjb/e2012-30070-x

127. Kunimitsu Uchinokura, T. S. and E. M. (1972). RAMAN SCATTERING BY SILICON. *Solid State Communications*, *11*, 47–49.

128. Kushima, A., Qian, X., Zhao, P., Zhang, S., & Li, J. (2015). Ripplocations in van der Waals layers. *Nano Letters*, *15*(2), 1302–1308. https://doi.org/10.1021/nl5045082

129. Lauritsen, J. V., Kibsgaard, J., Helveg, S., Topsøe, H., Clausen, B. S., Lægsgaard, E., & Besenbacher, F. (2007). Size-dependent structure of MoS2 nanocrystals. *Nature Nanotechnology*, *2*(1), 53–58. https://doi.org/10.1038/nnano.2006.171

130. Le, Q. Van, Nguyen, T. P., Jang, H. W., & Kim, S. Y. (2014). The use of UV/ozone-treated MoS 2 nanosheets for extended air stability in organic photovoltaic cells. *Phys. Chem. Chem. Phys.*, *16*(26), 13123–13128. https://doi.org/10.1039/C4CP01598C

131. Lee, C., Yan, H., Brus, L. E., Heinz, T. F., Hone, J., & Ryu, S. (2010). Anomalous Lattice Vibrations of Single- and Few-Layer MoS 2. *ACS Nano*, *4*(5), 2695–2700. https://doi.org/10.1021/nn1003937

132. Lee, Y. H., Zhang, X. Q., Zhang, W., Chang, M. T., Lin, C. Te, Chang, K. Di, … Lin, T. W. (2012). Synthesis of large-area MoS 2 atomic layers with chemical vapor deposition. *Advanced Materials*. https://doi.org/10.1002/adma.201104798

133. Lehtinen, O., Komsa, H. P., Pulkin, A., Whitwick, M. B., Chen, M. W., Lehnert, T., … Krasheninnikov, A. V. (2015). Atomic scale microstructure and properties of se-deficient two-dimensional MoSe2. *ACS Nano*. https://doi.org/10.1021/acsnano.5b00410

134. Li, H., Zhang, Q., Yap, C. C. R., Tay, B. K., Edwin, T. H. T., Olivier, A., & Baillargeat, D. (2012). From Bulk to Monolayer MoS2: Evolution of Raman Scattering. *Advanced Functional Materials*, *22*(7), 1385–1390. https://doi.org/10.1002/adfm.201102111

135. Li, Q., Walter, E. C., van der Veer, W. E., Murray, B. J., Newberg, J. T., Bohannan, E. W., … Penner, R. M. (2005). Molybdenum Disulfide Nanowires and Nanoribbons by Electrochemical/Chemical Synthesis. *The Journal of Physical Chemistry B*, *109*(8), 3169–3182. https://doi.org/10.1021/jp045032d

136. Li, S., Cai, H., Gan, C. L., Guo, J., Dong, Z., & Ma, J. (2010). Controlled Synthesis of Copper-Silicide Nanostructures. *Crystal Growth and Design*, *10*, 2983–2989. https://doi.org/10.1021/cg1000232

137. Li, T., & Galli, G. (2007). Electronic Properties of MoS 2 Nanoparticles. *The Journal of Physical Chemistry C*, *111*(44), 16192–16196. https://doi.org/10.1021/jp075424v

138. Li, W., Zhang, G., Guo, M., & Zhang, Y.-W. (2014). Strain-tunable electronic and transport properties of MoS2 nanotubes. *Nano Research*, *7*(4), 518–527. https://doi.org/10.1007/s12274-014-0418-y

139. Li, X., Mullen, J. T., Jin, Z., Borysenko, K. M., Buongiorno Nardelli, M., & Kim, K. W. (2013). Intrinsic electrical transport properties of monolayer silicene and MoS2 from first principles. *Physical Review B*, *87*(11), 115418.

https://doi.org/10.1103/PhysRevB.87.115418

140. Lin, J., Cretu, O., Zhou, W., Suenaga, K., Prasai, D., Bolotin, K. I., … Pantelides, S. T. (2014). Flexible metallic nanowires with self-adaptive contacts to semiconducting transition-metal dichalcogenide monolayers. *Nature Nanotechnology*, *9*(6), 436–442. https://doi.org/10.1038/nnano.2014.81

141. Lin, J., Pantelides, S. T., & Zhou, W. (2015). Vacancy-induced formation and growth of inversion domains in transition-metal dichalcogenide monolayer. *ACS Nano*. https://doi.org/10.1021/acsnano.5b00554

142. Lin, J., Zhang, Y., Zhou, W., & Pantelides, S. T. (2016). Structural Flexibility and Alloying in Ultrathin Transition-Metal Chalcogenide Nanowires. *ACS Nano*, *10*(2), 2782–2790. https://doi.org/10.1021/acsnano.5b07888

143. Lin, Y.-C., Dumcenco, D. O., Huang, Y.-S., & Suenaga, K. (2014). Atomic mechanism of the semiconducting-to-metallic phase transition in single-layered MoS2. *Nature Nanotechnology*, *9*(5), 391–396. https://doi.org/10.1038/nnano.2014.64

144. Lin, Y. C., Zhang, W., Huang, J. K., Liu, K. K., Lee, Y. H., Liang, C. Te, … Li, L. J. (2012). Wafer-scale MoS2 thin layers prepared by MoO3 sulfurization. *Nanoscale*. https://doi.org/10.1039/c2nr31833d

145. Lin, Z., Carvalho, B. R., Kahn, E., Xu, D., Zhu, Y., Liu, J., … Peng, W. (2016). Microwave-assisted 1T to 2H phase reversion of MoS 2 in solution : a fast route to processable dispersions of 2H-MoS 2 nanosheets and nanocomposites. *Nanotechnology*, *27*(38), 1–7. https://doi.org/10.1088/0957-4484/27/38/385604

146. Liu, G., Ma, H., Teixeira, I., Sun, Z., Xia, Q., Hong, X., & Tsang, S. C. E. (2016a). Hydrazine-Assisted Liquid Exfoliation of MoS_2 for Catalytic Hydrodeoxygenation of 4-Methylphenol. *Chemistry - A European Journal*, *22*(9), 2910–2914. https://doi.org/10.1002/chem.201504009

147. Liu, H., Neal, A. T., & Ye, P. D. (2012). Channel Length Scaling of MoS 2 MOSFETs. *ACS Nano*, *6*(10), 8563–8569. https://doi.org/10.1021/nn303513c

148. Liu, X., Xu, T., Wu, X., Zhang, Z., Yu, J., Qiu, H., … Guo, W. (2013). Top-down fabrication of sub-nanometre semiconducting nanoribbons derived from molybdenum disulfide sheets. *Nature Communications*. https://doi.org/10.1038/ncomms2803

149. Liu, Y. C., Wang, V., Xia, M. G., & Zhang, S. L. (2017). First-principles study on structural, thermal, mechanical and dynamic stability of T'-MoS 2. *Journal of Physics: Condensed Matter*, *29*(9), 095702. https://doi.org/10.1088/1361-648X/aa5213

150. Liu, Z., Suenaga, K., Wang, Z., Shi, Z., Okunishi, E., & Iijima, S. (2011). Identification of active atomic defects in a monolayered tungsten disulphide nanoribbon. *Nature Communications*. https://doi.org/10.1038/ncomms1224

151. Loh, T. A. J., & Chua, D. H. C. (2015). Origin of Hybrid 1T- and 2H-WS 2 Ultrathin Layers by Pulsed Laser Deposition. *The Journal of Physical Chemistry C*, *119*(49), 27496–27504. https://doi.org/10.1021/acs.jpcc.5b09277

152. Lv, R., Robinson, J. A., Schaak, R. E., Sun, D., Sun, Y., Mallouk, T. E., & Terrones, M. (2015). Transition metal dichalcogenides and beyond: Synthesis, properties, and applications of single- and few-layer nanosheets. *Accounts of Chemical Research*. https://doi.org/10.1021/ar5002846

153. M. Seibt, M. Griess, A.A. Istratov, H. Hedemann, A. Sattler, and W. S. (1998). Formation and properties of copper silicide precipitates in silicon. *Physica Status Solidi (A)*, *166*, 171.

154. Ma, H., Shen, Z., & Ben, S. (2018). Understanding the exfoliation and dispersion of MoS2 nanosheets in pure water. *Journal of Colloid and Interface Science*. https://doi.org/10.1016/j.jcis.2017.11.013

155. Ma, J., Zhang, Q., Yang, J., Feng, S., Lei, M., & Quhe, R. (2018). Computational study of phase engineered transition metal dichalcogenides heterostructures. *Computational Materials Science*, *142*, 129–134. https://doi.org/10.1016/j.commatsci.2017.10.014

156. Mahler, B., Hoepfner, V., Liao, K., Ozin, G. A., Mahler, B., Hoepfner, V., … Ozin, G. (2014). Colloidal Synthesis of 1T-WS 2 and 2H-WS2 Nanosheets : Applications for Photocatalytic Hydrogen Evolution . *Journal of the American Chemical Society*, *136*(40), 14121–14127.

157. Mak, K. F., Lee, C., Hone, J., Shan, J., & Heinz, T. F. (2010). Atomically thin MoS2: A new direct-gap semiconductor. *Physical Review Letters*, *105*(13), 2–5. https://doi.org/10.1103/PhysRevLett.105.136805

158. Manzeli, S., Ovchinnikov, D., Pasquier, D., Yazyev, O. V, & Kis, A. (n.d.). 2D transition metal dichalcogenides. https://doi.org/10.1038/natrevmats.2017.33

159. Margulis, L., Salitra, G., Tenne, R., & Talianker, M. (1993). Nested fullerene-like structures. *Nature*, *365*(6442), 113–114. https://doi.org/10.1038/365113b0

160. Mattheiss, L. F. (1973). Band structures of transition-metal-dichalcogenide layer compounds. *Physical Review B*, *8*(8), 3719–3740. https://doi.org/10.1103/PhysRevB.8.3719

161. Mattheiss, L. F. (1991). Structural effects on the calculated semiconductor gap of CrSi2. *Physical Review B*, *43*(2), 2–5.

162. May, P., Khan, U., Hughes, J. M., & Coleman, J. N. (2012). Role of solubility parameters in understanding the steric stabilization of exfoliated two-dimensional nanosheets by adsorbed polymers. *Journal of Physical Chemistry C*. https://doi.org/10.1021/jp302365w

163. McBrayer, J. D. (1986). Diffusion of Metals in Silicon Dioxide. *Journal of The Electrochemical Society*, *133*(6), 1242.

https://doi.org/10.1149/1.2108827

164. Meyer, J. C., Eder, F., Kurasch, S., Skakalova, V., Kotakoski, J., Park, H. J., … Kaiser, U. (2012). Accurate measurement of electron beam induced displacement cross sections for single-layer graphene. *Physical Review Letters*. https://doi.org/10.1103/PhysRevLett.108.196102

165. Meyer, J. C., Kisielowski, C., Erni, R., Rossell, M. D., Crommie, M. F., & Zettl, A. (2008). Direct imaging of lattice atoms and topological defects in graphene membranes. *Nano Letters*. https://doi.org/10.1021/nl801386m

166. Molina-Sánchez, A., & Wirtz, L. (2011). Phonons in single-layer and few-layer MoS <math display="inline"> <msub> <mrow/> <mn>2</mn> </msub> </math> and WS <math display="inline"> <msub> <mrow/> <mn>2</mn> </msub> </math>. *Physical Review B*, *84*(15), 155413. https://doi.org/10.1103/PhysRevB.84.155413

167. Monch, W. (1990). On the physics of metal-semiconductor interfaces. *Reports on Progress in Physics*, *53*(3), 221–278. https://doi.org/10.1088/0034-4885/53/3/001

168. Morales, J., Barranco, A., Caballero, A., Holgado, J. P., & Gonza, A. R. (2002). Interface Effects for Cu , CuO , and Cu 2 O Deposited on SiO 2 and ZrO 2 . XPS Determination of the Valence State of Copper in Cu / SiO 2 and Cu / ZrO 2 Catalysts. *Journal of Physical Chemistry B*, *106*, 6921–6929.

169. Mueller, T., & Malic, E. (2018). Exciton physics and device application of two-dimensional transition metal dichalcogenide semiconductors. *Npj 2D Materials and Applications*, *2*(1), 29. https://doi.org/10.1038/s41699-018-0074-2

170. Mukherjee, S., Maiti, R., Midya, A., Das, S., & Ray, S. K. (2015a). Tunable Direct Bandgap Optical Transitions in MoS 2 Nanocrystals for Photonic Devices. *ACS Photonics*, *2*(6), 760–768. https://doi.org/10.1021/acsphotonics.5b00111

171. Nagaraju, G., Tharamani, C. N., Chandrappa, G. T., & Livage, J. (2007). Hydrothermal synthesis of amorphous MoS2 nanofiber bundles via acidification of ammonium heptamolybdate tetrahydrate. *Nanoscale Research Letters*, *2*(9), 461–468. https://doi.org/10.1007/s11671-007-9087-z

172. Nguyen, T. P., Sohn, W., Oh, J. H., Jang, H. W., & Kim, S. Y. (2016). Size-Dependent Properties of Two-Dimensional MoS 2 and WS 2. *The Journal of Physical Chemistry C*, *120*(18), 10078–10085. https://doi.org/10.1021/acs.jpcc.6b01838

173. Nishiyama, A., Ter Horst, G., Zagwijn, P. M., Van Den Hoven, G. N., Frenken, J. W. M., Garten, F., … Vrijmoeth, J. (1996). Growth mode and interface structure of Ag on the HF-treated Si(111):H surface. *Surface Science*, *350*(1–3), 229–238. https://doi.org/10.1016/0039-6028(95)01073-4

174. Nüchter, M., Ondruschka, B., Bonrath, W., & Gum, A. (2004). Microwave assisted synthesis – a critical technology overview. *Green Chemistry*. https://doi.org/10.1039/b310502d

175. O'Neill, A., Khan, U., & Coleman, J. N. (2012). Preparation of high concentration dispersions of exfoliated MoS 2 with increased flake size. *Chemistry of Materials*. https://doi.org/10.1021/cm301515z

176. Ostadhossein, A., Rahnamoun, A., Wang, Y., Zhao, P., Zhang, S., Crespi, V. H., & Van Duin, A. C. T. (2017). ReaxFF Reactive Force-Field Study of Molybdenum Disulfide (MoS2). *Journal of Physical Chemistry Letters*, *8*(3), 631–640. https://doi.org/10.1021/acs.jpclett.6b02902

177. P Joensen, E D Crozier, N. A. and R. F. F. (1987). A study of single-layer and restacked MoS , by x-ray diffraction and x-ray absorption spectroscopy. *J. Phys. C: Solid State Phys.*, *20*(26), 4043–4053.

178. Pachauri, V., Kern, K., & Balasubramanian, K. (2013). Chemically exfoliated large-area two-dimensional flakes of molybdenum disulfide for device applications. *APL Materials*. https://doi.org/10.1063/1.4820423

179. Pandey, M., Bothra, P., & Pati, S. K. (2016). Phase Transition of MoS2 Bilayer Structures. *Journal of Physical Chemistry C*, *120*(7), 3776–3780. https://doi.org/10.1021/acs.jpcc.5b10904

180. Park, J.-H., Han, D.-S., Kang, Y.-J., Shin, S.-R., & Park, J.-W. (2014). Self-forming Al oxide barrier for nanoscale Cu interconnects created by hybrid atomic layer deposition of Cu–Al alloy. *Journal of Vacuum Science & Technology A: Vacuum, Surfaces, and Films*, *32*(1), 01A131. https://doi.org/10.1116/1.4845595

181. Pearton, S. J., Heo, W. H., Ivill, M., Norton, D. P., & Steiner, T. (2004). Dilute magnetic semiconducting oxides. *Semiconductor Science and Technology*, *19*(10). https://doi.org/10.1088/0268-1242/19/10/R01

182. Pua, F., Chia, C., Zakari, S., & Liew, T. (2010). Preparation of transition metal sulfide nanoparticles via hydrothermal route. *Sains Malaysiana*, *39*(2), 243–248. Retrieved from http://eprints.um.edu.my/5337/

183. Py, M. A., & Haering, R. R. (1983). Structural destabilization induced by lithium intercalation in MoS 2 and related compounds. *Canadian Journal of Physics*, *61*(1), 76–84. https://doi.org/10.1139/p83-013

184. Pyrz, W. D., Park, S., Vogt, T., & Buttrey, D. J. (2007). Electron beam-induced fragmentation and dispersion of Bi-Ni nanoparticles. *Journal of Physical Chemistry C*. https://doi.org/10.1021/jp071414i

185. Qi, Y., Xu, Q., Wang, Y., Yan, B., Ren, Y., & Chen, Z. (2016). CO 2 - Induced Phase Engineering: Protocol for Enhanced Photoelectrocatalytic Performance of 2D MoS 2 Nanosheets. *ACS Nano*, *10*(2), 2903–2909. https://doi.org/10.1021/acsnano.6b00001

186. Qin, X. R., Yang, D., Frindt, R. F., & Irwin, J. C. (1992). Scanning tunneling microscopy of single-layer MoS2 in water and butanol. *Ultramicroscopy*, *42–44*, 630–636. https://doi.org/10.1016/0304-3991(92)90334-G

187. Qing Tang and De-en Jiang. (2015). Stabilization and Band-Gap Tuning of

1T- MoS2 Monolayer by Covalent Functionalization. *Chemistry of Materials*, *27*(10), 3743–3748. https://doi.org/10.1021/acs.chemmater.5b00986

188. Quinn, M. D. J., Ho, N. H., & Notley, S. M. (2013). Aqueous dispersions of exfoliated molybdenum disulfide for use in visible-light photocatalysis. *ACS Applied Materials and Interfaces*. https://doi.org/10.1021/am404161k

189. Radisavljevic, B., Radenovic, A., Brivio, J., Giacometti, V., & Kis, A. (2011). Single-layer MoS2 transistors. *Nature Nanotechnology*, *6*(3), 147–150. https://doi.org/10.1038/nnano.2010.279

190. Raffone, F., Ataca, C., Grossman, J. C., & Cicero, G. (2016). MoS 2 Enhanced T-Phase Stabilization and Tunability Through Alloying. *The Journal of Physical Chemistry Letters*, *7*(13), 2304–2309. https://doi.org/10.1021/acs.jpclett.6b00794

191. Rai, A., Movva, H., Roy, A., Taneja, D., Chowdhury, S., & Banerjee, S. (2018). Progress in Contact, Doping and Mobility Engineering of MoS2: An Atomically Thin 2D Semiconductor. *Crystals*, *8*(8), 316. https://doi.org/10.3390/cryst8080316

192. Ramírez-Ortiz, J., Ogura, T., Medina-Valtierra, J., Acosta-Ortiz, S. E., Bosch, P., Antonio De Los Reyes, J., & Lara, V. H. (2001). A catalytic application of Cu2O and CuO films deposited over fiberglass. *Applied Surface Science*, *174*, 177–184. https://doi.org/10.1016/S0169-4332(00)00822-9

193. Remskar, M., Mrzel, A., Skraba, Z., Jesih, A., Ceh, M., Demsar, J., … Mihailovic, D. (2001). Self-Assembly of Subnanometer-Diameter Single-Wall MoS2 Nanotubes. *Science*, *292*(5516), 479–481. https://doi.org/10.1126/science.1059011

194. Remskar, M., Skraba, Z., Cléton, F., Sanjinés, R., & Lévy, F. (1996). MoS 2 as microtubes. *Applied Physics Letters*, *69*(3), 351–353. https://doi.org/10.1063/1.118057

195. Reshmi, S., Akshaya, M. V., Satpati, B., Basu, P. K., & Bhattacharjee, K. (2018a). Structural stability of coplanar 1T-2H superlattice MoS 2 under high energy electron beam. *Nanotechnology*, *29*(20), 205604. https://doi.org/10.1088/1361-6528/aab3c3

196. Reshmi, S., Akshaya, M. V., Satpati, B., Roy, A., Kumar Basu, P., & Bhattacharjee, K. (2017a). Tailored MoS 2 nanorods: a simple microwave assisted synthesis. *Materials Research Express*, *4*(11), 115012. https://doi.org/10.1088/2053-1591/aa949c

197. Robertson, A. W., & Warner, J. H. (2013). Atomic resolution imaging of graphene by transmission electron microscopy. *Nanoscale*, *5*(10), 4079. https://doi.org/10.1039/c3nr00934c

198. Rotunno, E., Fabbri, F., Cinquanta, E., Kaplan, D., Longo, M., Lazzarini, L., … Salviati, G. (2016). Structural, optical and compositional stability of MoS2 multi-layer flakes under high dose electron beam irradiation. *2D Materials*, *3*(2), 7. https://doi.org/10.1088/2053-1583/3/2/025024

199. Roy, A., Sundaravel, B., Batabyal, R., & Dev, B. N. (2012). Fractal pattern formation in thermal grooving at grain boundaries in Ag films on Si(111) surfaces. *Thin Solid Films*, *520*(15), 5086–5090. https://doi.org/10.1016/j.tsf.2012.03.011

200. Roy, Anupam, Bhattacharjee, K., Ghatak, J., & Dev, B. N. (2012). Growth of epitaxially oriented Ag nanoislands on air-oxidized Si(1 1 1)-(7 × 7) surfaces: Influence of short-range order on the substrate. *Applied Surface Science*, *258*(7), 2255–2265. https://doi.org/10.1016/j.apsusc.2011.09.060

201. Roy, Anupam, Guchhait, S., Sonde, S., Dey, R., Pramanik, T., Rai, A., … Banerjee, S. K. (2013). Two-dimensional weak anti-localization in Bi2Te3thin film grown on Si(111)-(7 × 7) surface by molecular beam epitaxy. *Applied Physics Letters*, *102*, 163118. https://doi.org/10.1063/1.4803018

202. Sadan, M. B., Houben, L., Enyashin, A. N., Seifert, G., & Tenne, R. (2008).

Atom by atom: HRTEM insights into inorganic nanotubes and fullerene-like structures. *Proceedings of the National Academy of Sciences*, *105*(41), 15643–15648. https://doi.org/10.1073/pnas.0805407105

203. Saigal, N., & Ghosh, S. (2016). Evidence for two distinct defect related luminescence features in monolayer MoS2. *Applied Physics Letters*, *109*(12). https://doi.org/10.1063/1.4963133

204. Santillo, G., Deorsola, F. A., Bensaid, S., Russo, N., & Fino, D. (2012). MoS 2 nanoparticle precipitation in turbulent micromixers. *Chemical Engineering Journal*, *207–208*, 322–328. https://doi.org/10.1016/j.cej.2012.06.127

205. Sarkar, D. K., Bera, S., Narasimhan, S. V, Chowdhury, S., Gupta, A., & Nair, K. G. M. (1998). GIXRD and XPS Investigation of Silicidation in Ion Beam Mixed Cu/Si(1 1 1) System. *Solid State Communications*, *107*(8), 413–416.

206. Sarma, J. V. N., Pande, S., Lepine, B., Turban, P., Gangopadhyay, S., Ababou-Girard, S., & Choudhary, S. (2018). Oxidation mechanism of thin Cu films: A gateway towards the formation of single oxide phase. *AIP Advances*, *8*(5), 055114. https://doi.org/10.1063/1.5028407

207. Savchenkov, A., Shukrinov, P., Mutombo, P., Slezák, J., & Cháb, V. (2002). Initial stages of Cu/Si interface formation. *Surface Science*, *507–510*, 889–894. https://doi.org/10.1016/S0039-6028(02)01407-3

208. Scafetta, M. D., Cordi, A. M., Rondinelli, J. M., & May, S. J. (2014). Band structure and optical transitions in LaFeO 3 : theory and experiment. *Journal of Physics: Condensed Matter*, *26*(50), 505502. https://doi.org/10.1088/0953-8984/26/50/505502

209. Scheuschner, N., Ochedowski, O., Kaulitz, A.-M., Gillen, R., Schleberger, M., & Maultzsch, J. (2014). Photoluminescence of freestanding single- and few-layer MoS 2. *Physical Review B*, *89*(12), 125406. https://doi.org/10.1103/PhysRevB.89.125406

210. Schlesinger, M. E. (1990). Thermodynamics of solid transition-metal silicides. *Chemical Reviews*, *90*(4), 607–628. https://doi.org/10.1021/cr00102a003

211. Sekar, K., Kuri, G., Satyam, P. V., Sundaravel, B., Mahapatra, D. P., & Dev, B. N. (1995). Shape transition in the epitaxial growth of gold silicide in Au thin films on Si(111). *Physical Review B*, *51*(20), 14330–14336. https://doi.org/10.1103/PhysRevB.51.14330

212. Sekar, K., Satyam, P. V., Kuri, G., Mahapatra, D. P., & Dev, B. N. (1993). An RBS study of interdiffusion across a brominated Si(111)/Cu interface with and without a barrier layer. *Nuclear Inst. and Methods in Physics Research, B*, *73*(1), 63–70. https://doi.org/10.1016/0168-583X(93)96054-G

213. Shin, D., Wang, S. X., Marshall, A. F., Kimura, W., Dong, C., Augustsson, A., & Guo, J. (2005). Growth and characterization of copper nanoclusters embedded in SiC matrix. *Thin Solid Films*, *473*, 267–271. https://doi.org/10.1016/j.tsf.2004.07.079

214. Shmeliov, A., Shannon, M., Wang, P., Kim, J. S., Okunishi, E., Nellist, P. D., … Nicolosi, V. (2014). Unusual stacking variations in liquid-phase exfoliated transition metal dichalcogenides. *ACS Nano*, *8*(4), 3690–3699. https://doi.org/10.1021/nn5003387

215. Singh, A. K., Kumar, P., Late, D. J., Kumar, A., Patel, S., & Singh, J. (2018). 2D layered transition metal dichalcogenides (MoS2): Synthesis, applications and theoretical aspects. *Applied Materials Today*. https://doi.org/10.1016/j.apmt.2018.09.003

216. Singh, A., Shirodkar, S. N., & Waghmare, U. V. (2015). 1H and 1T polymorphs, structural transitions and anomalous properties of (Mo , W)(S , Se) 2 monolayers : first-principles analysis. *2D Materials*, *2*(3), 35013. https://doi.org/10.1088/2053-1583/2/3/035013

217. Sivaraman, G., Arthur, F., Souza, L. De, & Rodrigo, G. (2016). Electronic Transport along Hybrid MoS 2 Monolayers. *Journal of Physical Chem*,

120(411), 23389–23396. https://doi.org/10.1021/acs.jpcc.6b07917

218. Skowron, S. T., Lebedeva, I. V., Popov, A. M., & Bichoutskaia, E. (2015). Energetics of atomic scale structure changes in graphene. *Chemical Society Reviews*, *44*(10), 3143–3176. https://doi.org/10.1039/C4CS00499J

219. Smith, R. J., King, P. J., Lotya, M., Wirtz, C., Khan, U., De, S., … Coleman, J. N. (2011). Large-scale exfoliation of inorganic layered compounds in aqueous surfactant solutions. *Advanced Materials*. https://doi.org/10.1002/adma.201102584

220. Splendiani, A., Sun, L., Zhang, Y., Li, T., Kim, J., Chim, C. Y., … Wang, F. (2010a). Emerging photoluminescence in monolayer MoS 2. *Nano Letters*, *10*(4), 1271–1275. https://doi.org/10.1021/nl903868w

221. Stephenson, T., Li, Z., Olsen, B., & Mitlin, D. (2014). Lithium ion battery applications of molybdenum disulfide (MoS 2) nanocomposites. *Energy Environ. Sci.*, *7*(1), 209–231. https://doi.org/10.1039/C3EE42591F

222. Stewart, J. A., & Spearot, D. E. (2013). Atomistic simulations of nanoindentation on the basal plane of crystalline molybdenum disulfide (MoS 2). *Modelling and Simulation in Materials Science and Engineering*, *21*(4), 045003. https://doi.org/10.1088/0965-0393/21/4/045003

223. Suenaga, K., Wakabayashi, H., Koshino, M., Sato, Y., Urita, K., & Iijima, S. (2007). Imaging active topological defects in carbon nanotubes. *Nature Nanotechnology*. https://doi.org/10.1038/nnano.2007.141

224. Sumitomo, K., Kobayashi, T., Shoji, F., Oura, K., & Katayama, I. (1991). Hydrogen-mediated epitaxy of Ag on Si(111) as studied by low-energy ion scattering. *Physical Review Letters*, *66*(9), 1193–1196. https://doi.org/10.1103/PhysRevLett.66.1193

225. Sun, L., Banhart, F., & Warner, J. (2015). Two-dimensional materials under electron irradiation. *MRS Bulletin*, *40*(1), 29–37. https://doi.org/10.1557/mrs.2014.303

226. Sundaravel, B., Das, A. K., Ghose, S. K., Rout, B., & Dev, B. N. (1999). Improvement of Ag(1 1 1) epitaxy on Si(1 1 1) by MeV Si+ irradiation and ion microbeam analysis of thermally induced morphology. *Nuclear Instruments and Methods in Physics Research, Section B: Beam Interactions with Materials and Atoms*, *156*(1), 130–134. https://doi.org/10.1016/S0168-583X(99)00281-5

227. Sundaravel, B., Das, A. K., Ghose, S. K., Sekar, K., & Dev, B. N. (1999). Epitaxial growth of silver on Br-passivated Si(111) substrates under high vacuum. *Applied Surface Science*, *137*(1–3), 11–19. https://doi.org/10.1016/S0169-4332(98)00484-X

228. Sundaravel, B., Sekar, K., Kuri, G., Satyam, P. V., Dev, B. N., Bera, S., … Caccavale, F. (1999). XPS and SIMS analysis of gold suicide grown on a bromine passivated Si(111) substrate. *Applied Surface Science*, *137*(1–3), 103–112. https://doi.org/10.1016/S0169-4332(98)00378-X

229. Suslick, K. S. (1995). Applications of Ultrasound to Materials Chemistry. *MRS Bulletin*. https://doi.org/10.1557/S088376940004464X

230. Tenne, R., Margulis, L., Genut, M., & Hodes, G. (1992). Polyhedral and cylindrical structures of tungsten disulphide. *Nature*, *360*(6403), 444–446. https://doi.org/10.1038/360444a0

231. Thermadam, S. P., Bhagat, S. K., Alford, T. L., Sakaguchi, Y., Kozicki, M. N., & Mitkova, M. (2010). Influence of Cu diffusion conditions on the switching of Cu-SiO2-based resistive memory devices. *Thin Solid Films*, *518*(12), 3293–3298. https://doi.org/10.1016/j.tsf.2009.09.021

232. Tian, Ye, He, Y., & Zhu, Y. (2004). Low temperature synthesis and characterization of molybdenum disulfide nanotubes and nanorods. *Materials Chemistry and Physics*, *87*(1), 87–90. https://doi.org/10.1016/j.matchemphys.2004.05.010

233. Tian, Yumei, Zhao, J., Fu, W., Liu, Y., Zhu, Y., & Wang, Z. (2005). A facile route to synthesis of MoS2 nanorods. *Materials Letters*, *59*(27), 3452–3455.

https://doi.org/10.1016/j.matlet.2005.06.012

234. Tian, Yumei, Zhao, X., Shen, L., Meng, F., Tang, L., Deng, Y., & Wang, Z. (2006). Synthesis of amorphous MoS2 nanospheres by hydrothermal reaction. *Materials Letters*. https://doi.org/10.1016/j.matlet.2005.09.029

235. Toh, R. J., Sofer, Z., Luxa, J., Sedmidubský, D., & Pumera, M. (2017). 3R phase of MoS 2 and WS 2 outperforms the corresponding 2H phase for hydrogen evolution. *Chemical Communications*, *53*(21), 3054–3057. https://doi.org/10.1039/C6CC09952A

236. Tongay, S., Suh, J., Ataca, C., Fan, W., Luce, A., Kang, J. S., … Wu, J. (2013). Defects activated photoluminescence in two-dimensional semiconductors: interplay between bound, charged and free excitons. *Scientific Reports*, *3*(1), 2657. https://doi.org/10.1038/srep02657

237. Towle, L. C., Oberbeck, V., Brown, B. E., & Stajdohar, R. E. (1966). Molybdenum diselenide: Rhombohedral high pressure-high temperature polymorph. *Science*. https://doi.org/10.1126/science.154.3751.895

238. Tung, R. T. (1992). Electron transport at metal-semiconductor interfaces: General theory. *Physical Review B*, *45*(23), 13509–13523. https://doi.org/10.1103/PhysRevB.45.13509

239. S., Jariwala, D., Sangwan, V. K., Lauhon, L. J., Marks, T. J., & Hersam, M. C. (2014). Emerging Device Applications for Semiconducting Two-Dimensional Transition Metal Dichalcogenides. *ACS Nano*, *8*(2), 1102–1120. https://doi.org/10.1021/nn500064s

240. Valladares, L. D. L. S., Salinas, D. H., Dominguez, A. B., Najarro, D. A., Khondaker, S. I., Mitrelias, T., … Majima, Y. (2012). Crystallization and electrical resistivity of Cu2O and CuO obtained by thermal oxidation of Cu thin films on SiO2 / Si substrates. *Thin Solid Films*, *520*(20), 6368–6374. https://doi.org/10.1016/j.tsf.2012.06.043

241. Vattikuti, S. V. P., Byon, C., Reddy, C. V., Shim, J., & Venkatesh, B. (2015).

Co-precipitation synthesis and characterization of faceted MoS2 nanorods with controllable morphologies. *Applied Physics A: Materials Science and Processing*, *119*(3), 813–823. https://doi.org/10.1007/s00339-015-9163-7

242. Vermaak, J. S., Snyman, L. W., & Auret, F. D. (1977). On the growth of Au on clean and contaminated GaAs(001) surfaces. *Journal of Crystal Growth*, *42*, 132–135. https://doi.org/10.1016/0022-0248(77)90185-3

243. Visic, B., Dominko, R., Gunde, M. K., Hauptman, N., Skapin, S. D., & Remskar, M. (2011). Optical properties of exfoliated MoS2 coaxial nanotubes - analogues of graphene. *Nanoscale Research Letters*, *6*(1), 593. https://doi.org/10.1186/1556-276X-6-593

244. Vivas-Castro, J., Rueda-Morales, G., Ortega-Cervantez, G., Moreno-Ruiz, L., Ortega-Aviles, M., & Ortiz-Lopez, J. (2011). Synthesis of Carbon Nanostructures by Microwave Irradiation. In *Carbon Nanotubes - Synthesis, Characterization, Applications*. https://doi.org/10.5772/17722

245. Voiry, D., Goswami, A., Kappera, R., Carvalho, C. De, Kaplan, D., Fujita, T., … Chhowalla, M. (2014). Covalent functionalisation of mololayered transition metal dichalcogenides by phase engineering. *Nature Chemistry*, *7*(1), 45–49. https://doi.org/10.1038/nchem.2108

246. Wang, D., Zhang, X., Bao, S., Zhang, Z., Fei, H., & Wu, Z. (2017). Phase engineering of a multiphasic 1T/2H MoS 2 catalyst for highly efficient hydrogen evolution. *Journal of Materials Chemistry A*, *5*(6), 2681–2688. https://doi.org/10.1039/C6TA09409K

247. Wang, Q. H., Kalantar-Zadeh, K., Kis, A., Coleman, J. N., & Strano, M. S. (2012). Electronics and optoelectronics of two-dimensional transition metal dichalcogenides. *Nature Nanotechnology*. https://doi.org/10.1038/nnano.2012.193

248. Wang, X., Feng, H., Wu, Y., & Jiao, L. (2013). Controlled synthesis of highly crystalline MoS2 flakes by chemical vapor deposition. *Journal of the American Chemical Society*. https://doi.org/10.1021/ja4013485

249. Wang, Yichao, Ou, J. Z., Balendhran, S., Chrimes, A. F., Mortazavi, M., Yao, D. D., … Kalantar-Zadeh, K. (2013). Electrochemical control of photoluminescence in two-dimensional MoS 2 nanoflakes. *ACS Nano*. https://doi.org/10.1021/nn4041987

250. Wang, Yongfan, Qu, F., Liu, J., Wang, Y., Zhou, J., & Ruan, S. (2015). Enhanced H2S sensing characteristics of CuO-NiO core-shell microspheres sensors. *Sensors and Actuators, B: Chemical*, *209*, 515–523. https://doi.org/10.1016/j.snb.2014.12.010

251. Warner, J. H., Rümmeli, M. H., Ge, L., Gemming, T., Montanari, B., Harrison, N. M., … Briggs, G. A. D. (2009). Structural transformations in graphene studied with high spatial and temporal resolution. *Nature Nanotechnology*, *4*(8), 500–504. https://doi.org/10.1038/nnano.2009.194

252. Wei, R., Yang, H., Du, K., Fu, W., Tian, Y., Yu, Q., … Zou, G. (2008). A facile method to prepare MoS2 with nanoflower-like morphology. *Materials Chemistry and Physics*, *108*(2–3), 188–191. https://doi.org/10.1016/j.matchemphys.2007.10.007

253. Werner, J. H., & Güttler, H. H. (1991). Barrier inhomogeneities at Schottky contacts. *Journal of Applied Physics*, *69*(3), 1522–1533. https://doi.org/10.1063/1.347243

254. Wiesel, I., Arbel, H., Albu-Yaron, A., Popovitz-Biro, R., Gordon, J. M., Feuermann, D., & Tenne, R. (2009). Synthesis of WS2 and MoS2 fullerene-like nanoparticles from solid precursors. *Nano Research*, *2*(5), 416–424. https://doi.org/10.1007/s12274-009-9034-7

255. Wilson, J. A., & Yoffe, A. D. (1969). The transition metal dichalcogenides discussion and interpretation of the observed optical, electrical and structural properties. *Advances in Physics*, *18*(73), 193–335. https://doi.org/10.1080/00018736900101307

256. Winchester, A., Ghosh, S., Feng, S., Elias, A. L., Mallouk, T., Terrones, M., & Talapatra, S. (2014). Electrochemical characterization of liquid phase

exfoliated two-dimensional layers of molybdenum disulfide. *ACS Applied Materials and Interfaces*. https://doi.org/10.1021/am4051316

257. Wright, G. B., & Mooradian, A. (1967). Raman scattering from donor and acceptor impurities in silicon. *Physical Review Letters, 18*(15), 608–610. https://doi.org/10.1103/PhysRevLett.18.608

258. Wypych, F, Solenthaler, C., Prins, R., & Weber, T. (1999). Electron Diffraction Study of Intercalation Compounds Derived from 1T-MoS2. *Journal of Solid State Chemistry*, *144*(2), 430–436. https://doi.org/10.1006/jssc.1999.8193

259. Wypych, Fernando, & Schöllhorn, R. (1992a). 1T-MoS 2 , a new metallic modification of molybdenum disulfide. *J. Chem. Soc., Chem. Commun.*, (19), 1386–1388. https://doi.org/10.1039/C39920001386

260. Xu, H., Zeiger, B. W., & Suslick, K. S. (2013). Sonochemical synthesis of nanomaterials. *Chemical Society Reviews*. https://doi.org/10.1039/c2cs35282f

261. Xu, M., Liang, T., Shi, M., & Chen, H. (2013). Graphene-like two-dimensional materials. *Chemical Reviews*. https://doi.org/10.1021/cr300263a

262. Yang, D., Sandoval, S. J., Divigalpitiya, W. M. R., Irwin, J. C., & Frindt, R. F. (1991). Structure of single-molecular-layer MoS2. *Physical Review B, 43*(14), 12053–12056. https://doi.org/10.1103/PhysRevB.43.12053

263. Ye, L., Wu, C., Guo, W., & Xie, Y. (2006). MoS 2 hierarchical hollow cubic cages assembled by bilayers: One-step synthesis and their electrochemical hydrogen storage properties. *Chemical Communications*. https://doi.org/10.1039/b610601c

264. Yuan, F., Wang, C., Li, G., Chang, S., Chu, L., Chen, L., & Tuan, H. (2013). Solution-phase synthesis of single-crystal Cu3Si nanowire arrays on diverse substrates with dual functions as high-performance field emitters and efficient anti-reflective layers. *Nanoscale, 5*(20), 9875–9881.

https://doi.org/10.1039/c3nr03045h

265. Yüksel, Ö. F. (2009). Temperature dependence of current–voltage characteristics of Al/p-Si (100) Schottky barrier diodes. *Physica B: Condensed Matter*, *404*(14–15), 1993–1997. https://doi.org/10.1016/j.physb.2009.03.026

266. Zabinski, J. S., Donley, M. S., Prasad, S. V., & McDevitt, N. T. (1994). Synthesis and characterization of tungsten disulphide films grown by pulsed-laser deposition. *Journal of Materials Science*. https://doi.org/10.1007/BF00356530

267. Zan, R., Bangert, U., Ramasse, Q., & Novoselov, K. S. (2011). Imaging of Bernal stacked and misoriented graphene and boron nitride: Experiment and simulation. *Journal of Microscopy*. https://doi.org/10.1111/j.1365-2818.2011.03520.x

268. Zan, R., Ramasse, Q. M., Jalil, R., Georgiou, T., Bangert, U., & Novoselov, K. S. (2013). Control of Radiation Damage in MoS by Graphene Encapsulation. *ACS Nano*, *7*(11), 10167–10174. https://doi.org/10.1021/nn4044035

269. Zelenski, C. M., & Dorhout, P. K. (1998). Template Synthesis of Near-Monodisperse Microscale Nanofibers and Nanotubules of MoS 2. *Journal of the American Chemical Society*, *120*(4), 734–742. https://doi.org/10.1021/ja972170q

270. Zeng, Z., Sun, T., Zhu, J., Huang, X., Yin, Z., Lu, G., … Zhang, H. (2012). An effective method for the fabrication of few-layer-thick inorganic nanosheets. *Angewandte Chemie - International Edition*. https://doi.org/10.1002/anie.201204208

271. Zeng, Z., Yin, Z., Huang, X., Li, H., He, Q., Lu, G., … Zhang, H. (2011). Single-layer semiconducting nanosheets: High-yield preparation and device fabrication. *Angewandte Chemie - International Edition*. https://doi.org/10.1002/anie.201106004

272. Zhang, J., Liu, C., & Fan, J. (2013). Comparison of Cu thin films deposited on Si substrates with different surfaces and temperatures. *Applied Surface Science*, *276*, 417–423. https://doi.org/10.1016/j.apsusc.2013.03.109

273. Zhang, Zhou, Wang, L. M., Ong, H. G., Wang, X. J., Wang, J. L., & Wang, S. J. (2008). Self-assembled shape- and orientation- controlled synthesis of nanoscale Cu 3 Si triangles , squares , and wires. *Nano Letters*, *8*(10), 3205–3210.

274. Zhang, Zhuhua, Zou, X., Crespi, V. H., & Yakobson, B. I. (2013). Intrinsic Magnetism of Grain Boundaries in Two-Dimensional Metal Dichalcogenides. *ACS Nano*, *7*(12), 10475–10481. https://doi.org/10.1021/nn4052887

275. Zhao, W., & Ding, F. (2017). Energetics and Kinetics of Phase Transition Between 2H and 1T MoS2 Monolayer—a Theoretical Study. *Nanoscale*, *9*(6), 2301–2309. https://doi.org/10.1039/xxxxxx

276. Zhao, X., Kotakoski, J., Meyer, J. C., Sutter, E., Sutter, P., Krasheninnikov, A. V., … Zhou, W. (2017). Engineering and modifying two-dimensional materials by electron beams. *MRS Bulletin*, *42*(09), 667–676. https://doi.org/10.1557/mrs.2017.184

277. Zheng, J., Zhang, H., Dong, S., Liu, Y., Tai Nai, C., Suk Shin, H., … Ping Loh, K. (2014). High yield exfoliation of two-dimensional chalcogenides using sodium naphthalenide. *Nature Communications*. https://doi.org/10.1038/ncomms3995

278. Zheng, X., Zhu, L., Yan, A., Bai, C., & Xie, Y. (2004). Ultrasound-assisted cracking process to prepare MoS2 nanorods. *Ultrasonics Sonochemistry*, *11*(2), 83–88. https://doi.org/10.1016/S1350-4177(03)00137-8

279. Zheng, Z., Wu, H. H., Chen, H., Cheng, Y., Zhang, Q., Xie, Q., … Zeng, X. C. (2018). Fabrication and understanding of Cu3Si-Si@carbon@graphene nanocomposites as high-performance anodes for lithium-ion batteries. *Nanoscale*, *10*(47), 22203–22214. https://doi.org/10.1039/c8nr07207h

280. Zhou, F., Szczech, J., Pettes, M. T., Moore, A. L., Jin, S., & Shi, L. (2007). Determination of transport properties in chromium disilicide nanowires via combined thermoelectric and structural characterizations. *Nano Letters*, *7*(6), 1649–1654. https://doi.org/10.1021/nl0706143

281. Zhou, J. B., & Gustafsson, T. (1997). Growth of thin Cu films on MgO (001). *Surface Science*, *375*, 221–225.

282. Zhou, K.-G., Mao, N.-N., Wang, H.-X., Peng, Y., & Zhang, H.-L. (2011). A Mixed-Solvent Strategy for Efficient Exfoliation of Inorganic Graphene Analogues. *Angewandte Chemie International Edition*, *50*(46), 10839–10842. https://doi.org/10.1002/anie.201105364

283. Zhou, W., Zou, X., Najmaei, S., Liu, Z., Shi, Y., Kong, J., … Idrobo, J. C. (2013). Intrinsic structural defects in monolayer molybdenum disulfide. *Nano Letters*. https://doi.org/10.1021/nl4007479

284. Zhu, J., Wang, Z., Yu, H., Li, N., Zhang, J., Meng, J., … Zhang, G. (2017). Argon Plasma Induced Phase Transition in Monolayer MoS 2. *Journal of the American Chemical Society*, *139*(30), 10216–10219. https://doi.org/10.1021/jacs.7b05765

285. Zhu, S., Meng, Q., Wang, L., Zhang, J., Song, Y., Jin, H., … Yang, B. (2013). Highly photoluminescent carbon dots for multicolor patterning, sensors, and bioimaging. *Angewandte Chemie - International Edition*. https://doi.org/10.1002/anie.201300519

286. Zhu, Y.-J., & Chen, F. (2014). Microwave-Assisted Preparation of Inorganic Nanostructures in Liquid Phase. *Chemical Reviews*, *114*(12), 6462–6555. https://doi.org/10.1021/cr400366s

287. Zilberberg, K., & Riedl, T. (2016). Metal-nanostructures – a modern and powerful platform to create transparent electrodes for thin-film photovoltaics. *Journal of Materials Chemistry A*, *4*(38), 14481–14508. https://doi.org/10.1039/C6TA05286J

288. Zuo, Z. J., Li, J., Han, P. De, & Huang, W. (2014). XPS and DFT studies on the autoxidation process of Cu sheet at room temperature. *Journal of Physical Chemistry C*, *118*(35), 20332–20345. https://doi.org/10.1021/jp504977p

LIST OF PUBLICATIONS BASED ON THE THESIS

International Journals

1. **S Reshmi,** M V Akshaya, Biswarup Satpati, Anupam Roy, Palash Kumar Basu, K Bhattacharjee (2017). Tailored MoS_2 nanorods: A simple Microwave Assisted Synthesis. *Mater. Res. Express* **,** 4 (11), 0–16**.**

2. **S Reshmi,** M V Akshaya, Biswarup Satpati, Palash Kumar Basu, K Bhattacharjee (2018). Structural Stability of coplanar 1T- 2H superlattice MoS_2 under high energy electron beam. *Nanotechnology,* 29, 205604

3. **S Reshmi**, Manu Mohan, Anupam Roy, K. Bhattacharjee. Evidence of an intermediate semiconducting Cu-O-Si phase in Cu-SiO_2/Si(111) system: An elemental and electrical characterization. *Thin solid films (Under review)*

Peer Reviewed Conference Proceedings

1. S Reshmi , M V Akshaya, Biswarup Satpati, Palash Kumar Basu, K Bhattacharjee(2018). Electron Beam Interaction and its Effect on the Crystalline 2H Phase of MoS2. **AIP Conference Proceedings**, 1942, 050097.

2. Gauthami Viswan., S Reshmi , Sachidanand P S, Manu Mohan, K. Bhattacharjee. Electrical characterizations of tailored MoS2 nanostructures. **IOP Conference series (Accepted).**

3. Sachidanand P. S, M. M. Sreelal, S Reshmi , Gauthami Viswan, Manu Mohan, Surya Kumar Gautam, Rakesh Kumar Singh, K. Bhattacharjee, MoS2 Nanostructures as highly transparent material: Optical transmittance measurements. Elsevier Materials Today Proceedings (**Accepted, In press**).

CONFERENCES/SEMINARS

Talks

1. S. Reshmi, Manu Mohan, Anupam Roy, K. Bhattacharjee. *Segregation of Cu on Si Surfaces: Atomic Force Microscopy and X-ray Photoelectron Spectroscopy Studies*; 2nd International Conference on Nano Science &

Engineering Applications (**ICONSEA 2018**), Jawaharlal Nehru Technological University (JNTU), Hyderabad, October 4- 6, (2018)

Poster Presentations

1. S. Reshmi, Abhishek Rai, Sudipta Roy Barman, K. Bhattacharjee. *Room Temperature Growth of Sn on Au(111) surface: Charge transport and Electronic Properties using Scanning Probe Microscopy*; Fourth International Conference on Frontiers in Nanoscience and Technology, (COCHIN NANO-2016), Cochin university of Science and technology (CUSAT), February 20- 23 (2016).

2. S. Reshmi, Akshaya M.V, Palash Kumar Basu, K. Bhattacharjee. *Electron Beam Interaction and its Effect on the Crystalline 2H Phase of* MoS_2; 62^{nd} DAE - Solid State Physics Symposium, Babha Atomic Research Center, Bombay, December 26-30 (2017).

Workshops

1. GIAN course on " Nanotechnology: From Fundamentals to Practice"; IISER, Trivandrum, June 13- 17 (2016).